# ENVIRONMENTAL LIMITATIONS TO FOREST GROWTH AND PRODUCTIVITY IN NORTH AMERICA

Matthew P. Dannenberg

"A dissertation submitted to the faculty at the University of North Carolina at Chapel Hill in partial fulfillment of the requirements for the degree of Doctor of Philosophy in the Curriculum of Geography."

Chapel Hill
2017

Approved by:

Conghe Song

Erika Wise

Aaron Moody

Diego Riveros-Iregui

Tamlin Pavelsky

## ABSTRACT

Matthew P. Dannenberg: Environmental Limitations to Forest Growth and Productivity in North America
(Under the direction of Conghe Song and Erika Wise)

Terrestrial primary production—the carbohydrates produced by plants via photosynthesis—is the entry point of energy and carbon into ecosystems, forming the base of the food chain and a sink for anthropogenic $CO_2$. Primary production can be limited by unfavorable environmental conditions, including non-optimal temperatures, water deficits, or inadequate nutrient supply. At present, our ability to model how environmental factors reduce primary production remains limited. This leads to uncertainty both in the remotely sensed models used to monitor primary production and in climate models that depend on accurate representation of the land surface and biosphere.

Given the importance of vegetation to humanity and the Earth system, in this dissertation I use tree rings and remote sensing to examine the environmental drivers of forest growth and productivity in North America. In particular, this research examines how forests are influenced by climate, atmospheric circulation, and land surface characteristics like topography and soil quality. I first examine how the seasonality of temperature and precipitation affect growth of ponderosa pine in the U.S. Pacific Northwest. I then develop a new tree-ring "environmental stress" index, which I use to model the climatic, topographic, and edaphic drivers of forest growth across the conterminous U.S. Finally, I examine how variability of the Pacific storm track acts as a synoptic-scale driver of hydroclimate and vegetation activity in western North America.

In this research, I show that forest primary productivity is significantly influenced by moisture supply across multiple seasons, particularly in western North America. Westerly Pacific storm tracks are largely responsible for delivery of moisture to this region, and I show that northerly shifts of these storm tracks reduce both water supply and primary production in the northwestern U.S. Using a set of machine learning model experiments, I also demonstrate that models of forest growth that incorporate topographic and soil characteristics outperform those based solely on climate. Taken together, these findings provide a framework for improving the models used to reconstruct past climate from tree-ring data and to monitor primary production with remote sensing, while also providing insight into potential influences of a warming climate on the biosphere.

To Becky: my wife, partner and best friend.

## ACKNOWLEDGEMENTS

Many individuals have contributed to the research presented in this dissertation. First and foremost, I thank my graduate advisors, Conghe Song and Erika Wise, for their many years of support, mentorship, and guidance. This work would not have been possible without them. I also thank the members of my graduate committee—Aaron Moody, Tamlin Pavelsky, and Diego Riveros-Iregui—for their comments and feedback over the years, which were instrumental in improving this research. Thank you as well to the anonymous reviewers whose comments on my manuscripts have contributed to the improvement of this dissertation. I am also grateful for the support of other graduate students in the Song and Wise labs, particularly Chris Hakkenberg and Qi Zhang. Finally, this research was supported by a small army of undergraduate and graduate research assistants (Kelsey Ajo, Dusty Grossheim, Chris Jones, Jocelyn Keung, Holly Kuestner, Claire Nelson, Zachary Pope, Melissa Wrzesien, and Lillian Wu), each of whom contributed in various ways to the collection and processing of datasets that were used in this dissertation.

This work was funded in part by NSF Paleo Perspectives on Climate Change (P2C2) grants 1102757 and 1304422, as well as by a Dissertation Completion Fellowship and the Ed and Carol Smithwick Summer Research Fellowship (both from UNC-Chapel Hill) and a Dissertation Research Grant from the American Association of Geographers. Many of the datasets used in this research were freely provided by the International Tree-Ring Data Bank, the Global Inventory Modeling and Mapping Studies (GIMMS), the USDA Natural Resources Conservation Service, the AmeriFlux network of eddy covariance flux towers, the Climate Research Unit at the University of East Anglia, and the PRISM research group at Oregon State University. I thank all of the contributors to these datasets.

## TABLE OF CONTENTS

## LIST OF TABLES

## LIST OF FIGURES

## LIST OF ABBREVIATIONS

| | |
|---|---|
| AVHRR | Advance Very High Resolution Radiometer |
| BI | Blue intensity |
| CPS | Composite-plus-scale |
| CRB | Columbia River basin |
| DBH | Diameter at Breast Height |
| EPS | Expressed Population Signal |
| EVC | Extreme value capture |
| EW | Earlywood width |
| GPP | Gross Primary Production |
| ITRDB | International Tree-Ring Data Bank |
| LUE | Light-Use Efficiency |
| LW | Latewood width |
| $LW_{adj}$ | Adjusted latewood width |
| NDVI | Normalized difference vegetation index |
| PAR | Photosynthetically active radiation |
| PCA | Principle component analysis |
| $P_{cool}$ | Cool-season precipitation |
| $P_{warm}$ | Warm-season precipitation |
| RF | Random Forest |
| SPEI | Standardized Precipitation-Evapotranspiration Index |
| SWE | Snow water equivalent |
| TMAX | Mean monthly maximum temperature |
| TMIN | Mean monthly minimum temperature |
| TRW | Total ring width |

| | |
|---|---|
| TWI | Topographic Wetness Index |
| UAA | Upslope Accumulated Area |
| VPD | Vapor Pressure Deficit |
| WB | Water Balance |

# CHAPTER 1: INTRODUCTION

## Overview

Vegetation on Earth's land surface provides many of the key resources and services that humans and other animals rely upon. Terrestrial primary production—the carbohydrates produced by plants via photosynthesis—is the entry point of energy and carbon into ecosystems and the fundamental source of food for all land-dwelling organisms [*Chapin et al.*, 2011]. Recent estimates suggest that approximately 80% of available net primary production has already been appropriated for human use, with the remainder representing a key "planetary boundary" for future human activity [*Running*, 2012]. Uptake of $CO_2$ through plant productivity is also a major component of the global carbon cycle [*Pan et al.*, 2011]. Historically, primary production by terrestrial vegetation has acted as a large sink for $CO_2$, with approximately 25% of annual anthropogenic $CO_2$ emissions being removed from the atmosphere by plants [*Ciais et al.*, 2013].

The productivity of terrestrial vegetation can be limited or co-limited by multiple climate or environmental factors [*Nemani et al.*, 2003; *Garbulsky et al.*, 2010]. Precise knowledge of the environmental drivers of vegetation productivity is therefore needed both to monitor current vegetation activity over large areas and to project potential changes in ecosystem structure and function under a changing climate. At present, this knowledge is limited, particularly regarding how environmental limitations to plant growth vary spatially and temporally over large areas. The current generation of remotely sensed primary production models, for example, generally assume instantaneous responses of plant productivity to temperature and moisture [e.g., *Running et al.*, 2004], while largely ignoring

the effects of soils, topography, and lags between the climate system and plant activity. Estimating the effects of water stress on primary production is particularly challenging [*Zhang et al.*, 2015], and error in primary production estimates derived from remotely sensed data can partly be traced to uncertainties in the parameterization of these environmental limitations [*Cai et al.*, 2014]. Likewise, global climate models depend on accurate representation of environmental limitations to vegetation productivity. While projected changes in temperature, hydroclimate, and atmospheric circulation during the 21$^{st}$ century will likely have a strong impact on the primary production of the biosphere, there remains significant disagreement over whether the positive influences of climate change on vegetation (e.g., $CO_2$ fertilization and longer growing seasons) will outweigh its negative consequences (e.g., greater water stress and higher respiration rates) [*Settele et al.*, 2014; *Allen et al.*, 2015; *Smith et al.*, 2016; *Ballantyne et al.*, 2017].

Given the importance of vegetation for provisioning of ecosystem goods and services to humanity, as well as the current limitations in our understanding of how vegetation is limited by environmental conditions, my research is motivated by a fundamental question of contemporary biogeoscience: **how do vegetated ecosystems interact with and respond to variation in other Earth systems?** In this dissertation, I examine the environmental drivers of vegetation activity in North America and how sensitivity to those environmental drivers varies spatially and temporally. In particular, this work focuses on how vegetation activity in North America is influenced by three interacting components of the atmosphere and lithosphere (Figure 1.1):

(1) Local weather and climate conditions experienced by plants (e.g., temperature, precipitation, and vapor pressure deficit), with a particular focus on how the *seasonality* of climate affects ecosystem processes.

(2) Atmospheric circulation systems, particularly midlatitude storm tracks, which are largely responsible for water delivery to western North America.

(3) Land surface characteristics, specifically topography and soil structure and quality, that affect the ability of plants to obtain belowground resources like soil water and nutrients.

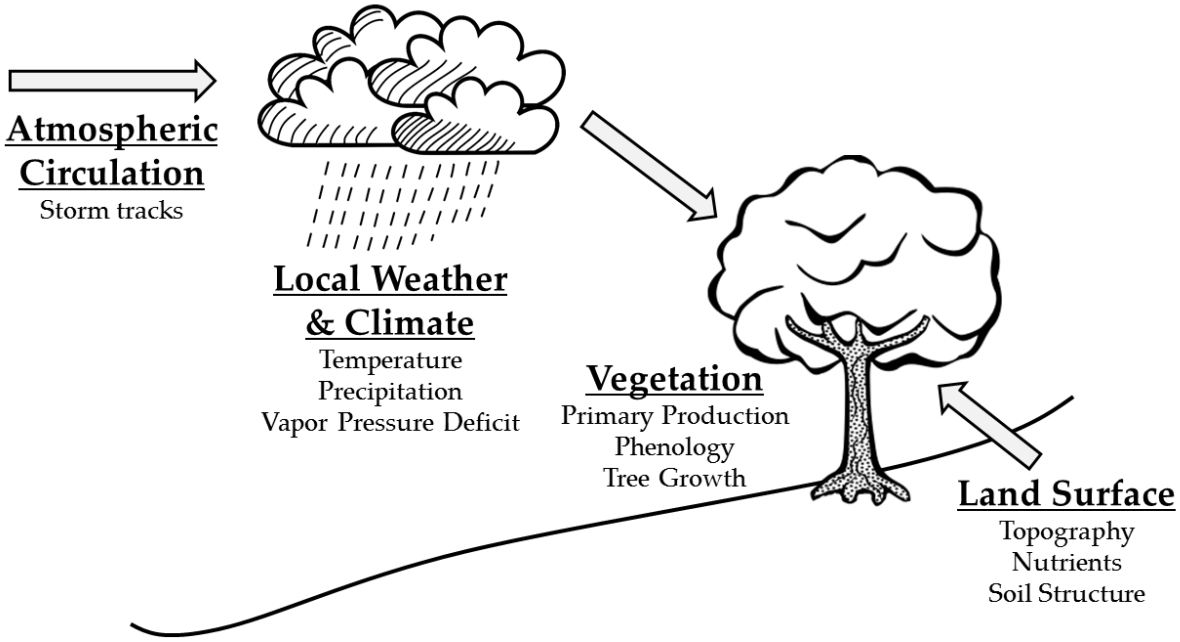


**Figure 1.1.** The Earth system perspective on the environmental limitations to vegetation activity that underlies this dissertation. The general Earth system of interest is represented in bold and underlined text, while the specific processes examined are represented in smaller text below each system.

In this Introduction, I first review the necessary background for the dissertation, focusing on two aspects of previous work that are relevant to all subsequent chapters: (1) the current state of knowledge regarding climatic and land surface limitations to vegetation activity, particularly at the level of individual plants, and (2) the two different, but complementary, measures of vegetation activity that I will use in the subsequent chapters to assess environmental limitations to plant growth at regional to continental scales. I then introduce the structure of the dissertation, including the main research questions, methods,

and findings of each individual chapter. I conclude with a summary of how this dissertation will contribute to current conversations in the fields of physical geography and biogeoscience.

## Background

*Environmental limitations to vegetation activity*

In order to assess the environmental drivers of vegetation activity over a large area, which is the fundamental goal of my dissertation, it is necessary to understand the physiological processes that connect individual plants with their environment. At the leaf level, the photosynthetic process starts with diffusion of $CO_2$ from the atmosphere into leaves through the stoma. However, when stomata are open, water is also lost from the leaf to the atmosphere. This loss of water from the leaf is replenished by water from the soil. To prevent excessive loss of water, plants regulate stomatal apertures based on the availability of soil moisture and the strength of the atmospheric sink for moisture. Low soil moisture, high vapor pressure deficit, and low leaf water potential therefore limit photosynthesis by restricting diffusion of $CO_2$ into stomata.

Moisture stress can also directly affect photosynthetic processes through metabolic damage or down-regulation (e.g., reduced ATP and RuBP synthesis or permanent photoinhibition) [*Flexas*, 2002; *Pallardy*, 2008] and through increased risk of xylem embolisms, cavitation, and hydraulic failure [*McDowell et al.*, 2011; *Williams et al.*, 2013]. Extreme duration and intensity of water stress can result in mortality due to carbon starvation (i.e., depletion of carbohydrate reserves due to greater reduction of photosynthesis than maintenance and growth respiration), disruption of xylem water transport, or increased susceptibility to biotic attack [*McDowell et al.*, 2011]. Water availability can also impact primary production indirectly through its control on nutrient cycling [*Chapin et al.*, 2011], by

reducing the capacity of plants to repair damage, and by exacerbating temperature-induced damage to the photosynthetic apparatus [*Allakhverdiev et al.*, 2008].

Temperature can affect vegetation activity both directly and indirectly. For example, temperature directly affects the rates of biochemical reactions in photosynthesis, with optimal temperatures that vary among different plant species and biomes [*Pallardy*, 2008]. At low temperatures, biochemical reactions occur at slower rates while high temperatures can lead to enzyme deactivation, protein denaturation, damage to photosystem II, generation of reactive oxygen species, and increased photorespiration [*Allakhverdiev et al.*, 2008; *Pallardy*, 2008]. Freezing temperatures also subject plants to increased risk of xylem embolisms and cavitation [*Pallardy*, 2008; *Chapin et al.*, 2011] and limit the ability of plant roots to obtain belowground resources [*Archibold*, 1995]. Temperature is a dominant control on the length of the vegetation growing season [*Richardson et al.*, 2013], though changes in the length of the growing season do not necessarily lead to proportional increases in primary production or net ecosystem exchange due to the effects of temperature on water availability and ecosystem respiration [*Angert et al.*, 2005; *Hu et al.*, 2010; *Brzostek et al.*, 2014; *Zhang et al.*, 2014; *Dannenberg et al.*, 2015]. In arid and semi-arid regions, high temperatures can exacerbate soil water limitation through increases in vapor pressure deficit and evaporative demand, which can lead to stomatal closure and thus lower rates of carbon assimilation [*McDowell et al.*, 2011; *Williams et al.*, 2013].

Finally, non-climatic environmental factors, such as soils and topography, can affect primary production through their control on the ability of plants to obtain necessary belowground resources. The nutrient content of soils can be an important limiting factor to the growth and productivity of terrestrial vegetation, particularly as a result of insufficient nitrogen or phosphorous, both of which are often in short supply in terrestrial ecosystems but which are necessary for formation of proteins, enzymes, and nucleic acids [*Pallardy*, 2008;

*Chapin et al.*, 2011]. Structural characteristics of soils, including soil depth and porosity, affect soil water storage and the ease with which plants can extract water from the soil [*Chapin et al.*, 2011; *Hornberger et al.*, 2014]. Likewise, topography affects the lateral redistribution of water within a watershed [*Beven and Kirkby*, 1979; *Hornberger et al.*, 2014], which is an important control on soil moisture [*Western et al.*, 1999] and therefore on ecosystem carbon and water fluxes [*Riveros-Iregui and McGlynn*, 2009; *Emanuel et al.*, 2010, 2011; *Riveros-Iregui et al.*, 2011]. Land surface characteristics like topography and soil structure and quality therefore represent important spatial constraints on the ability of plants to obtain belowground resources like water and nutrients.

*The canopy and the cambium: two perspectives on vegetation activity*

Variation in climate and land surface characteristics can affect vegetation processes both in the leaves of plant canopies and in the vascular cambium, which can be measured using remote sensing and tree rings, respectively. At the canopy level, solar radiation in the visible spectrum (i.e., photosynthetically active radiation (PAR)) provides the energy to drive photosynthesis. Healthy, productive plant canopies therefore tend to absorb most incoming PAR, while reflecting or transmitting most incoming near infrared radiation. The reflectance of the land surface in these spectral regions can be estimated through remote sensing, meaning that remotely sensed vegetation indices based on the difference between near infrared and visible reflectance (such as the normalized difference vegetation index) can be used to map and monitor canopy-level vegetation processes over large areas repeatedly through time. These vegetation indices form the basis for monitoring vegetation structure and function [*Song et al.*, 2015], including important processes in ecosystem carbon cycling like the fraction of PAR absorbed by plant canopies [e.g., *Myneni et al.*, 2002], gross and net

primary production [e.g., *Running et al.*, 2004], and land surface phenology [e.g., *Moody and Johnson*, 2001].

The carbohydrates produced through photosynthesis provide both the energy and the molecular structure needed for cell division and expansion in the vascular cambium of woody tissues [*Fritts*, 1976; *Pallardy*, 2008]. In regions where photosynthetic and cambial processes are limited by climate (either temperature or water availability), the widths of tree rings may vary annually as a function of climate. This variability provides the fundamental basis for using tree rings as proxies for past variation in temperature [e.g., *Mann et al.*, 1998, 2008; *Luterbacher et al.*, 2004], precipitation [e.g., *Neukom et al.*, 2010; *Yi et al.*, 2012], streamflow [e.g., *Wise*, 2010c; *Littell et al.*, 2016], and atmospheric circulation [e.g., *Wise and Dannenberg*, 2014]. The annual tree rings formed through cambial processes also represent the primary production that is allocated to woody growth, allowing long-term estimates of annual aboveground primary production based on measurements of tree-ring widths [e.g., *Graumlich et al.*, 1989; *Rathgeber et al.*, 2000]. Unlike remote sensing, tree-ring chronologies are located at discrete point locations and do not provide continuous spatial coverage of vegetation processes. However, they have demonstrated significant skill at representing productivity across entire landscapes [*Beck et al.*, 2013; *Bunn et al.*, 2013], including for grasslands near the tree-ring site [*Liang et al.*, 2009], suggesting that tree rings are likely useful indicators of ecosystem productivity across large regions and even for regions dominated by other plant functional types.

Together, remote sensing and tree-ring data provide complementary information on vegetation activity (Table 1.1). Remote sensing provides spatially continuous, but indirect, estimates of canopy structure and function at regular intervals over the past several decades. Tree rings, on the other hand, provide long-term, direct measurements of growth at discrete locations. Combining these two sources of vegetation information can therefore provide two

perspectives on the terrestrial carbon cycle across a range of spatial, temporal, and process scales [*Babst et al.*, 2014].

**Table 1.1.** Complementary characteristics of remote sensing and tree-ring estimates of vegetation activity.

| | Remote Sensing | Tree Rings |
|---|---|---|
| Spatial Scale | Continuous | Discrete |
| Frequency | Daily - Monthly | Annual |
| Length of Record | Decades | Centuries - Millennia |
| Process Measured | Canopy | Cambium |
| Type of Measurement | Indirect | Direct |

**Dissertation Structure and Contributions**

In this dissertation, I use both remote sensing and tree-ring data to examine the environmental factors that limit vegetation activity over large areas of North America, with the overarching goal of **identifying the spatial and temporal drivers of vegetation activity** in this region. Each chapter examines a different aspect of environmental limitations to plant growth (Figure 1.2), ranging from atmospheric circulation to the local climatic conditions experienced by plants to physical land surface characteristics. Below, I present a brief summary of each individual chapter as well as the key contributions of the dissertation as a whole.

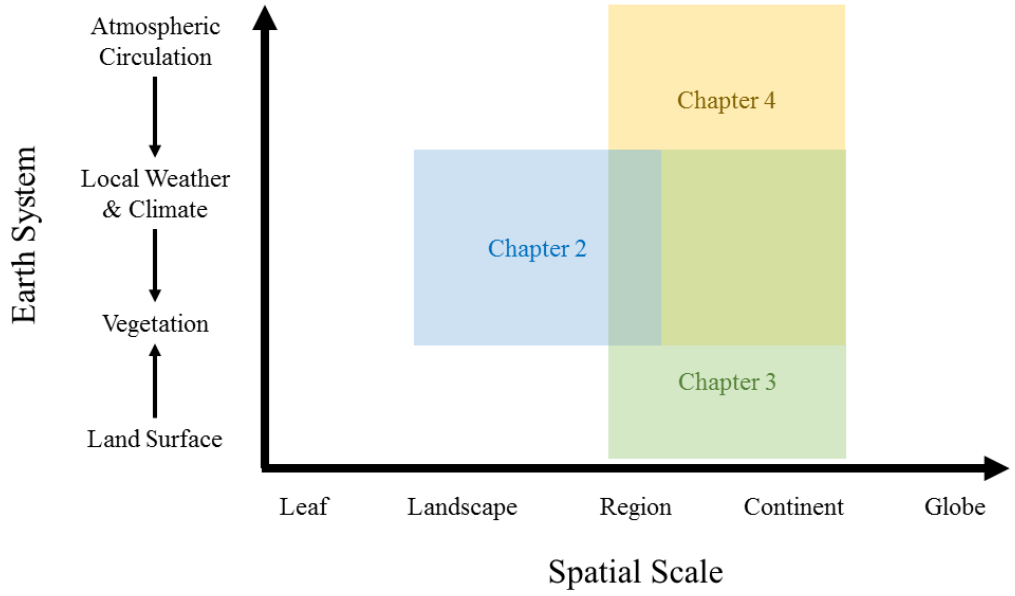


**Figure 1.1.** Spatial scales and Earth systems examined in each chapter.

*Summary of Chapter 2*

Research Questions: How does sub-annual growth of a prominent tree species in the western U.S. (*Pinus ponderosa* subsp. *ponderosa*) respond to seasonal climate variability? What are the implications of that response both for reconstruction of past climate and for understanding the consequences of future hydroclimatic change for these ecosystems?

Aims and Methods: In this chapter, I examine how the seasonality of precipitation and temperature affect tree growth, as measured by total ring width, earlywood width, adjusted latewood width, and blue intensity chronologies from a network of six *Pinus ponderosa* sites in and surrounding the upper Columbia River basin of the U.S. Pacific Northwest. I also evaluate the potential for combining multiple tree-ring metrics together in reconstructions of past cool- and warm-season precipitation.

Key Findings: Warm-season precipitation tends to be a limiting factor across all sites and tree-ring metrics. Earlywood and latewood widths differ primarily in their sensitivity to conditions in the year prior to growth, while total and earlywood widths from the lowest

elevation sites also show relatively strong dependence on cool-season moisture. Temperature is not strongly limiting at any of the sites nor for any tree-ring metric. Effective correlation analyses and composite-plus-scale tests suggest that combining multiple tree-ring metrics together may improve reconstructions of warm-season precipitation. For cool-season precipitation, total ring width alone explains more variance than any other individual metric or combination of metrics. The composite-plus-scale tests show that ponderosa pine tree rings in the upper Columbia River basin are asymmetric in their responses precipitation extremes: while growth indices strongly reflect low (but not high) precipitation extremes during the cool season, they reflect high (but not low) precipitation extremes during the warm season.

*Summary of Chapter 3*

Research Questions: What are the dominant sources of "environmental stress" in vegetated ecosystems of the conterminous United States? How responsive are these ecosystems to climate conditions prior to the growing season? What are the consequences of failing to account for topography and soil characteristics in models of environmental stress?

Aims and Methods: I develop a data-driven approach for estimation of environmental stress effects on forest growth (based on tree-ring widths) and assess the environmental drivers of both spatial and temporal variation of forest growth stress. I first test and evaluate the new environmental stress index at six ponderosa pine tree-ring sites in the U.S. Pacific Northwest and then apply the index to a large network of tree-ring widths across the conterminous United States. Finally, I use correlation analyses and a series of machine learning model experiments to examine the climatic, topographic, and edaphic drivers of growth in ecoregions of the U.S.

Key Findings: Comparison of the newly developed environmental stress index to annual gross primary production from nearby eddy covariance flux towers demonstrates that

the environmental stress index captures meaningful information on primary production at the continental scale. Tree growth in ecosystems of the western United States relies on water that is delivered prior to the growing season, a key finding given that many primary production models do not include physically-meaningful lags between the climate system and ecosystem carbon uptake. In addition, topographic and soil characteristics, which are not typically included in the current generation of remote sensing-based primary production models, are important drivers of spatial gradients in mean environmental stress in most of the eastern U.S.

*Summary of Chapter 4*

Research Questions: How have the hydroclimate and water resources of western North America responded to historical Pacific storm track variability? How have storm track-induced changes in water supply affected primary production, phenology, and fire regimes in this region?

Aims and Methods: I estimate cool-season Pacific storm track position and intensity for the period 1980-2014 using 300 hPa meridional wind velocity from the North American Regional Reanalysis. Using historical climate data, I examine the sensitivity of water resources (the climatic water balance, snowpack, and streamflow) to variation in the position and intensity of the storm track. To examine the sensitivity of ecological systems to storm track variability, I develop or obtain estimates of forest growth, land surface phenology, and wildfire area from a large network of tree-ring widths and remotely sensed data from AVHRR and Landsat.

Key Findings: Over the study period, cool-season storm tracks entered western North America between approximately 41°N to 53°N. I show that cool-season moisture availability and snow water equivalent both exhibit strong responses to this variability in storm track position, with positive correlations to storm track latitude in eastern Alaska and northwestern

Canada but negative correlations in the northwestern U.S. Likewise, tree-ring widths and remotely sensed estimates of peak greenness show that ecosystems of the western U.S. tend to be greener and more productive following winters with south-shifted storm tracks, while Canadian ecosystems tend to be greener in years when the cool-season storm track is shifted to the north. On average, larger areas of the northwestern U.S. are burned by moderate to high severity wildfires when storm tracks are displaced north, and the average burn area per fire also tends to be higher in years with north-shifted storm tracks. A persistent shift in the position of Pacific storm tracks during the 21st century would likely alter hydroclimatic and ecological regimes in western North America, particularly in the western U.S., where water supply and vegetation activity are closely linked to the position of the Pacific storm track.

*Overall contributions of the dissertation*

Taken together, the research performed in this dissertation makes two primary contributions within the fields of physical geography and Earth system science. First, by examining the sensitivity of North American forests to climate seasonality and land surface characteristics, this dissertation will lay a framework for improving both the tree-ring models used to reconstruct past climate and the remotely sensed models used to monitor primary production. Second, this research will contribute to understanding how future climate change will influence vegetation activity in North America, particularly in the dry regions of western North America where changes in temperature, drought, snowpack, evaporative demand, and precipitation seasonality have occurred in the recent past [*Barnett et al.*, 2008; *Pederson et al.*, 2011; *Kapnick and Hall*, 2012] and are expected to continue in the future [*Cayan et al.*, 2008; *Seager and Vecchi*, 2010; *Ashfaq et al.*, 2013; *Pierce and Cayan*, 2013; *Pierce et al.*, 2013; *Seager et al.*, 2013; *Cook et al.*, 2014, 2015; *Rupp et al.*, 2016].

# CHAPTER 2: SEASONAL CLIMATE SIGNALS FROM MULTIPLE TREE-RING METRICS: A CASE STUDY OF *PINUS PONDEROSA* IN THE UPPER COLUMBIA RIVER BASIN[1]

## Introduction

Temperature increases over the 21st century will alter hydroclimatic regimes in many regions, and these impacts will be highly seasonal [*Lute et al.*, 2015]. In the U.S. Pacific Northwest, climate models project relatively little change in total annual precipitation, but this precipitation may be redistributed from the warm season to the cool season, resulting in an enhanced seasonal precipitation cycle in which dry summers become drier and wet winters become wetter [*Mote and Salathé*, 2010]. Even with projected increases in winter precipitation, warmer temperatures could lead to reductions in snowpack and an increasingly rain-dominated climate. In the western U.S., for example, climate change has led to significant reductions in mountain snowpack which are nearly unprecedented in historical and paleoclimate records [*Barnett et al.*, 2005; *Mote et al.*, 2005; *Pederson et al.*, 2011; *Luce et al.*, 2013]. Declining snowpacks, combined with seasonality shifts, are a major challenge for water resource managers in these regions [*Hamlet and Lettenmaier*, 1999; *Leung et al.*, 2004; *Crawford et al.*, 2015], increasing the need to understand historical variation of precipitation and drought on sub-annual time scales. These changes in hydroclimate will also have significant consequences for the functioning of terrestrial ecosystems [*Settele et al.*, 2014], including likely changes in vegetation distribution, fire regimes, and carbon uptake

[1] This chapter previously appeared as an article in the *Journal of Geophysical Research: Biogeosciences*. The original citation is as follows:

Dannenberg, M. P., and E. K. Wise (2016), Seasonal climate signals from multiple tree-ring metrics: a case study of Pinus ponderosa in the upper Columbia River basin, *J. Geophys. Res. Biogeosciences, 121,* 1178-1189, doi:10.1002/2015JG003155.

and storage [*Boisvenue and Running*, 2010; *Rogers et al.*, 2011; *Notaro et al.*, 2012; *Jiang et al.*, 2013].

The annual growth rings of trees can be used both to understand the sensitivity of tree growth to climate variability and to make inferences about past climate variability and change, including past variation of hydroclimate on seasonal timescales. Tree rings are frequently used as indicators of past environmental variation due to the sensitivity of cambial processes to climate, the longevity of many tree species, the relative simplicity and cost effectiveness of data collection, and the precise annual crossdating of each ring [*Fritts*, 1976; *Jones et al.*, 2009; *St. George*, 2014]. Tree-ring widths and densities have been used to infer past temperatures [*Mann et al.*, 1998, 2008; *Jones et al.*, 2009], precipitation [*Touchan et al.*, 2005; *Neukom et al.*, 2010], atmospheric circulation [*Wise and Dannenberg*, 2014], streamflow [*Wise*, 2010c], snow cover [*Pederson et al.*, 2011], and drought [*Cook et al.*, 1999, 2004]. The climate signals and seasonality recorded in tree rings reflect the environmental factors that are most limiting to growth, which in turn depend upon both the local environmental conditions, such as climate regime and topography, and the physiology of the tree species, including leaf phenology and longevity [*Fritts*, 1976]. The climate sensitivity of tree rings therefore varies geographically. In the southwestern U.S., for example, tree growth is most responsive to winter precipitation, while sites at high northern latitudes are often most responsive to temperature [*St. George*, 2014; *St. George and Ault*, 2014].

In some circumstances, additional tree-ring metrics, such as sub-annual ring widths and densities, may further enhance and isolate seasonal climate signals that are not resolvable from total ring-width alone. Earlywood and latewood widths (EW and LW, respectively) may be sensitive to water availability in different seasons. In the U.S. Southwest, EW reflects cool-season precipitation [*Stahle et al.*, 2009; *Griffin et al.*, 2013; *Meko et al.*, 2013] while

LW reflects warm-season precipitation [*Meko and Baisan*, 2001; *Stahle et al.*, 2009; *Griffin et al.*, 2013]. Previous studies in western Canada and the U.S. Intermountain West have also examined seasonal climate signals in sub-annual ring widths, including at ponderosa pine and Douglas-fir sites in British Columbia, Canada [*Watson and Luckman*, 2002] and Douglas-fir sites in Idaho and Montana [*Crawford et al.*, 2015]. *Watson and Luckman* [2002] found that both EW and LW are positively correlated with summer precipitation, though EW is more sensitive than LW to precipitation in winter and in the year prior to growth. While there is substantial overlap in the seasonal precipitation signals embedded in EW and LW chronologies, *Crawford et al.* [2015] found that EW is most sensitive to spring precipitation (April–June) while LW is most sensitive to precipitation later in the growing season (June–August). Neither EW nor LW were strongly correlated with temperature in these studies [*Watson and Luckman*, 2002; *Crawford et al.*, 2015].

The maximum density of tree-ring latewood is often strongly and positively dependent on summer temperature [e.g., *Briffa et al.*, 2004; *Kirdyanov et al.*, 2008; *Wilson et al.*, 2014], but it is expensive and time-consuming to obtain. Since the amount of blue light reflected from tree-ring latewood is inversely related to the density of latewood cells, the intensity of blue light reflectance from tree-ring latewood (blue intensity, or BI) can provide a reliable proxy for maximum latewood density with a similar climate signal at a fraction of the cost [*McCarroll et al.*, 2002, 2011; *Rydval et al.*, 2014; *Wilson et al.*, 2014]. Combining multiple tree ring metrics with complementary seasonal climate signals may improve the reconstruction of past climate [*McCarroll et al.*, 2003, 2011].

In this chapter, I examine the sensitivity of *Pinus ponderosa* subsp. *ponderosa* (ponderosa pine) tree-ring chronologies to seasonal climate variability at a network of six sites in and surrounding the U.S.'s upper Columbia River basin (CRB) in Washington state. The objectives of this study are to determine the sensitivity of different ponderosa pine

metrics to seasonal climate variability within the upper CRB and to evaluate the potential for a multi-metric tree ring reconstruction of past precipitation in both the cool and warm seasons. This work provides additional tests of the climate signals embedded in a relatively new paleoclimate proxy, BI. Results from this study demonstrate the utility of sub-annual ring widths for capturing seasonal climate signals and the potential for combining multiple tree-ring metrics in reconstructions of past hydroclimate on a sub-annual temporal scale in the Pacific Northwest region of the U.S.

## Data and Methods

### *Study Area and Climate Data*

The upper CRB (HUC Subregion 1702) is a semi-arid region covering most of central and eastern Washington in the U.S. Pacific Northwest (Figure 2.1). Monthly mean maximum temperatures and monthly precipitation were obtained for the period 1913-2012 from the PRISM (Parameter-elevation Relationships on Independent Slopes Model) Climate Group [*Daly et al.*, 2008], and were averaged and downloaded for the upper CRB from WestMap (http://www.cefa.dri.edu/Westmap/). During the period 1981-2010, mean temperatures ranged from below freezing during winter months to approximately 20°C in July and August (Figure A1). Annual precipitation in the CRB ranged from approximately 350 mm to more than 700 mm (with a mean of approximately 500 mm), with most precipitation received during the winter months (Figure A1).

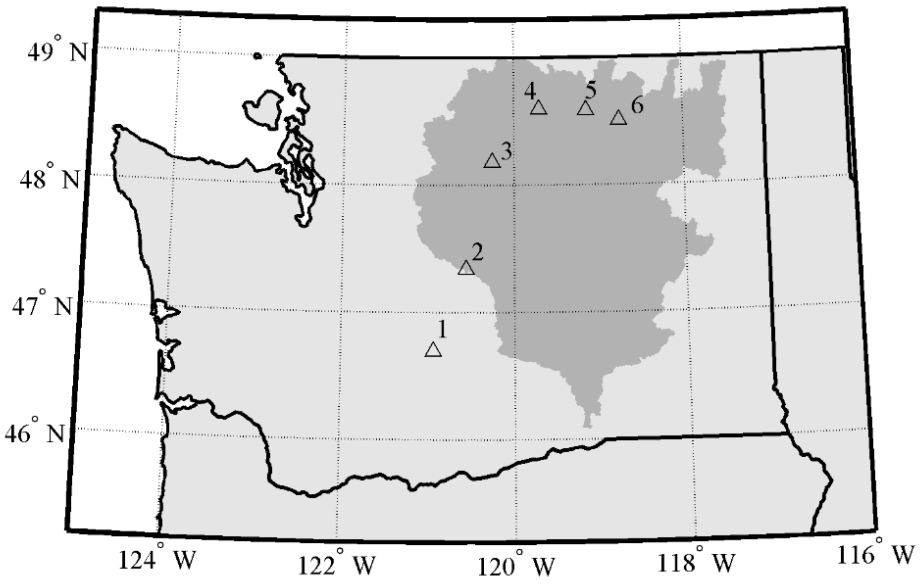


**Figure 2.1.** Six tree-ring sites in and surrounding the upper Columbia River Basin (HUC Subregion 1702; dark grey shading).

*Tree-Ring Data*

Increment cores were collected from six sites in and surrounding the upper CRB during summers 2011-2014 (Figure 2.1; Table A1). Site elevations ranged from approximately 825 meters to nearly 1400 meters above sea level. Trees with fire or lightening scars, which were widespread at several of the sites, were avoided when possible. Cores were collected, processed, and cross-dated following standard dendrochronological procedures [*Stokes and Smiley*, 1968]. Total ring width (TRW) was measured to 0.001 mm precision for at least one core per dated tree using a Velmex measuring system. Earlywood and latewood widths were measured following procedures outlined in *Griffin et al.* [2011]. Using the dplR package in the R statistical program [*Bunn*, 2008; *R Core Team*, 2014], all ring width series were detrended with a cubic smoothing spline with a wavelength two-thirds the length of the series and a frequency response of 0.5 [*Cook and Peters*, 1981; *Cook*, 1985], and site-level residual chronologies were formed using Tukey's biweight robust mean. Since LW is partially dependent on prior EW [*Stahle et al.*, 2009; *Griffin et al.*, 2011, 2013; *Crawford et*

*al.*, 2015], an adjusted LW index ($LW_{adj}$) was developed for each measured core prior to site-level averaging based on the residuals of a linear regression of the detrended LW width on the detrended EW width [*Griffin et al.*, 2011]. After quality control of ring width measurements using COFECHA [*Holmes*, 1983] and removing series with low correlations to the master chronologies, most ring-width chronologies achieved an expressed population signal (EPS) > 0.85 over the period 1913-2012 with the exception of $LW_{adj}$ chronologies at sites 1, 2, and 4, which each had EPS > 0.8 (Table A1).

A subset of cores from each site were scanned at 3200 DPI on a flatbed scanner, and BI chronologies were developed using the CooRecorder software [*Rydval et al.*, 2014]. Previous studies have suggested extracting resins from cores prior to scanning using soxhlet extraction or acetone baths [*Campbell et al.*, 2007, 2011; *Rydval et al.*, 2014; *Wilson et al.*, 2014], but I was not able to perform any resin extraction since these cores were subsequently used in isotope analyses. While the lack of resin extraction would likely pose a significant problem for a reconstruction due to large color differences between heartwood and sapwood, I focused solely on the climate signal in tree-ring metrics during the instrumental period (1913-2012). Most BI series consisted entirely of sapwood during the study period, but heartwood–sapwood boundaries were visually identified in the core scans and the heartwood BI was not considered in further analyses. Additional details of the blue intensity methodology are available in Appendix 3 (Text A1).

*Analyses*

I examined the sensitivity of different tree-ring metrics to seasonal climate variability using un-rotated principal component analysis (PCA), which I performed separately for each of the four tree-ring metrics over the period 1913-2012 using the six different site chronologies as variables to highlight the common signals among the sites. PCA was

performed using singular value decomposition on the covariance matrices of *P. ponderosa* metrics. Using the Seascorr program in the MATLAB programming environment [*Meko et al.*, 2011], I performed running correlations between the first two components of each tree-ring metric (a total of eight chronologies) and 1-, 3-, 6-, and 9-month composites of upper CRB-averaged precipitation (the primary variable) and maximum temperature (the secondary variable). Seasonal correlations between tree-ring metric PCs and the primary variable were calculated using the Pearson correlation coefficient. The relationship between tree-ring metrics and the secondary variable was assessed using partial correlation analysis (i.e., the correlation after the influence of the primary variable is removed), with significance of correlations estimated using Monte Carlo simulations [*Meko et al.*, 2011].

I assessed the potential for combining multiple tree-ring metrics in precipitation reconstructions using composites of the ponderosa pine BI and ring width PCs. Many approaches have been developed for compositing proxy time-series, but compositing generally involves either a weighted or unweighted averaging of standardized proxy records [*Jones et al.*, 2009]. Here, I standardized the first two PCs of each tree-ring metric to a common mean and variance so that all variables are on the same scale. I then formed a total of 21 composites using weighted averages of different metrics and PCs (Tables 2.1 and 2.2), where the weight was derived from the percentage of the variance explained in a linear relationship between a given component and the climate time-series of interest [*McCarroll et al.*, 2011]. I calculated "effective correlations" [*McCarroll et al.*, 2003, 2011] between these ponderosa pine composites and two precipitation composites: cool-season precipitation ($P_{cool}$, defined as the total precipitation from October through March) and warm-season precipitation ($P_{warm}$, defined as the total precipitation from May through August). A Lilliefors test of normality [*Lilliefors*, 1967] indicated that warm-season precipitation was not normally distributed, so all subsequent tests were performed using log-transformed $P_{warm}$.

In addition to the effective correlation analysis, I assessed the potential for a multi-metric tree ring reconstruction of cool- and warm-season precipitation in the upper CRB using a series of composite-plus-scale (CPS) tests. The CPS approach is a flexible tool for climate reconstruction [*Jones et al.*, 2009] that has been used with a variety of paleoclimate proxies, including tree-ring datasets [*Briffa et al.*, 2001; *Esper et al.*, 2002] and multiproxy datasets [*Crowley and Lowery*, 2000; *Mann and Jones*, 2003; *Moberg et al.*, 2005; *Neukom et al.*, 2011; *Emile-Geay et al.*, 2013]. In CPS methods, the mean and variance of composited proxy series are re-scaled to match the mean and variance of the target climate variable [*Jones et al.*, 2009]. I tested seven ponderosa pine composites for both $P_{cool}$ and $P_{warm}$, each containing both PCs of at least one metric (composites labeled "COMBO" in Tables 2.1 and 2.2). The mean and variance of each composite were re-scaled to match the mean and variance of $P_{cool}$ and $P_{warm}$ over the 1913-2012 study period. Additional details of the CPS methods used in this study are available in Appendix 3 (Text A2). While this variance-scaling approach does not suffer from the variance loss inherent in other reconstruction methods (e.g., inverse regression), the mean squared error in the model will, by definition, be inflated relative to a least squares solution [*McCarroll et al.*, 2015]. I therefore assessed the potential skill of seasonal precipitation reconstructions in the CRB using a variance-scaled adaptation of the coefficient of determination ($R^2_{vs}$), which can be interpreted in a manner similar to the commonly used reduction of error and coefficient of efficiency statistics, where $R^2_{vs} > 0$ indicates that the variance-scaled reconstruction is more skillful than a reconstruction based solely on the climatological mean [*McCarroll et al.*, 2015].

Since part of the justification for variance-scaled reconstructions is to better capture the full range of climate variability (including extreme events), I examined the sensitivity of ponderosa pine chronologies to extreme wet and extreme dry years during both the cool and warm seasons using the "extreme value capture" (EVC) statistic [*McCarroll et al.*, 2015]. I

defined extreme precipitation thresholds in each season based on the upper and lower 10$^{th}$ percentiles of the 100 year PRISM record and then calculated the proportion of these years that were correctly identified as extremely dry ($EVC_{low}$) or extremely wet ($EVC_{high}$) in the CPS predictions. Since I defined extreme events as the upper and lower 10$^{th}$ percentiles, there is a $\frac{1}{10}$ chance that the CPS-predicted precipitation will correctly identify an extreme year by chance alone. As in *McCarroll et al.* [2015], I used the binomial distribution to determine when the number of correctly identified extremes is significantly different than expected by chance.

**Table 2.1.** Effective correlations between $P_{cool}$ and tree-ring PCs, and the variance-scaled $R^2$ ($R^2_{vs}$) and extreme value capture statistics for both extreme low ($EVC_{low}$) and extreme high precipitation ($EVC_{high}$) events for COMBO composites. The model with the highest $R^2_{vs}$ is shown in bold and italics.

| | PC1 | PC2 | COMBO | $R^2_{vs}$ | $EVC_{low}$ | $EVC_{high}$ |
|---|---|---|---|---|---|---|
| TRW | 0.36 | 0.46 | 0.56 | ***0.12*** | 0.7*** | 0.2 |
| EW | 0.37 | 0.35 | 0.49 | <0 | 0.5** | 0.3 |
| $LW_{adj}$ | 0.16 | 0.19 | 0.24 | <0 | 0.1 | 0.3 |
| BI | 0.35 | -0.19 | 0.38 | <0 | 0.4* | 0.2 |
| EW + $LW_{adj}$ | 0.38 | 0.36 | 0.52 | 0.04 | 0.5** | 0.2 |
| EW + $LW_{adj}$ + BI | 0.39 | 0.36 | 0.51 | 0.02 | 0.5** | 0.1 |
| All Four | 0.39 | 0.42 | 0.56 | 0.11 | 0.5** | 0.1 |

* $p<0.05$
** $p<0.01$
*** $p<0.001$

**Table 2.2.** Effective correlations between $P_{warm}$ and tree-ring PCs, and the variance-scaled $R^2$ ($R^2_{vs}$) and extreme value capture statistics for both extreme low ($EVC_{low}$) and extreme high precipitation ($EVC_{high}$) events for COMBO composites. The model with the highest $R^2_{vs}$ is shown in bold and italics.

| | PC1 | PC2 | COMBO | $R^2_{vs}$ | $EVC_{low}$ | $EVC_{high}$ |
|---|---|---|---|---|---|---|
| TRW | 0.48 | -0.30 | 0.56 | 0.13 | 0.2 | 0.5** |
| EW | 0.42 | -0.28 | 0.51 | 0.03 | 0.2 | 0.4* |
| $LW_{adj}$ | 0.53 | -0.24 | 0.57 | 0.14 | 0.1 | 0.7*** |
| BI | 0.52 | 0.27 | 0.57 | 0.15 | 0 | 0.5** |
| EW + $LW_{adj}$ | 0.61 | 0.33 | 0.66 | ***0.32*** | 0 | 0.6*** |
| EW + $LW_{adj}$ + BI | 0.59 | 0.34 | 0.65 | 0.30 | 0 | 0.8*** |
| All Four | 0.59 | 0.34 | 0.66 | 0.31 | 0.1 | 0.6*** |

* $p<0.05$
** $p<0.01$
*** $p<0.001$

**Results**

The first component of the PCA emphasizes the growth patterns common to all sites (i.e., positive loadings on all sites) (Figure A2). The second component may reflect differences in elevation among sites (Figure A3), though further research would be needed to confirm this relationship given the limited sample size in this study ($n$ = 6). For TRW and EW, low elevation sites (sites 1 and 4) occupy one end of the PC2 spectrum while the highest elevation site (site 2) occupies the other. This suggests that while these sites have similar primary signals in TRW and EW (likely due to similar growth-limiting factors), they have different secondary signals that may indicate the presence of additional growth-limiting factors at some sites, perhaps related to site elevation. For TRW and EW, sites 1 and 4 also occupy one end of the PC2 spectrum with sites 5 and 6 representing the opposite extreme for $LW_{adj}$ and site 5 for BI (Figure A2). The first principal components represent substantially more variance than the remaining components (Figure A4). The first and second principal components explain 58.8-70.7% and 11.0-14.8% of the variance among sites, respectively (Table A3). Together, the first two components explain 73.6-81.7% of the variance among sites.

Pairwise correlations among the tree-ring metric PCs indicate that there is a wide range in the amount of variance that is shared by different measures of tree growth (Table 2.3). Since each individual tree ring is mostly composed of EW, this metric is closely related to TRW ($r^2$>0.8 for both PCs). As highlighted in previous research [e.g., *Griffin et al.*, 2011], unadjusted LW is closely coupled to prior EW and that dependence is also reflected in the EW and LW principal components in the U.S. Pacific Northwest ($r^2$=0.53 for PC1; $r^2$=0.39 for PC2). The core-level adjustment of LW substantially reduces this dependence on prior EW ($r^2$=0.03 for PC1; $r^2$=0.09 for PC2) so that $LW_{adj}$ and EW represent discrete climate signals, as in previous studies [*Stahle et al.*, 2009; *Griffin et al.*, 2011, 2013; *Crawford et al.*, 2015]. BI is closely related to all other tree-ring metrics ($r^2 \geq 0.22$), particularly with unadjusted LW ($r^2$=0.83 for PC1; $r^2$=0.42 for PC2), which demonstrates that the processes contributing to formation of latewood width and density are not independent of each other and that these metrics likely share a similar climate signal. The common signal shared by LW and BI is reduced following adjustment of LW for dependence on prior EW ($r^2$=0.53 for PC1; $r^2$=0.22 for PC2).

**Table 2.3.** Shared variance ($r^2$) among PC1 metrics (lower-left of matrix) and among PC2 metrics (upper-right of matrix).

| | TRW | EW | LW | $LW_{adj}$ | BI |
|---|---|---|---|---|---|
| TRW | - | 0.82 | 0.64 | 0.21 | 0.32 |
| EW | 0.96 | - | 0.39 | 0.09 | 0.24 |
| LW | 0.67 | 0.53 | - | 0.61 | 0.42 |
| $LW_{adj}$ | 0.09 | 0.03 | 0.58 | - | 0.22 |
| BI | 0.51 | 0.38 | 0.83 | 0.53 | - |

Correlations between PC1 of each metric and seasonal climate variables show that the dominant climate signal embedded in TRW and EW series in the upper CRB is spring and summer precipitation in the year of growth, late-summer and autumn precipitation during the

previous growing season, and some additional contribution from winter precipitation (Figure 2.2; full Seascorr results in Figure A5). For $LW_{adj}$, the upper CRB chronologies primarily reflect summer precipitation (May through August) in the year of growth, with very little contribution from prior growing season conditions. The BI signal is similar to the ring width signals and primarily reflects warm-season precipitation in both the year of growth and the prior growing season. After accounting for the influence of precipitation on growth, there are generally low and non-significant correlations between maximum temperature and tree-ring metrics at these sites (Figure A5).

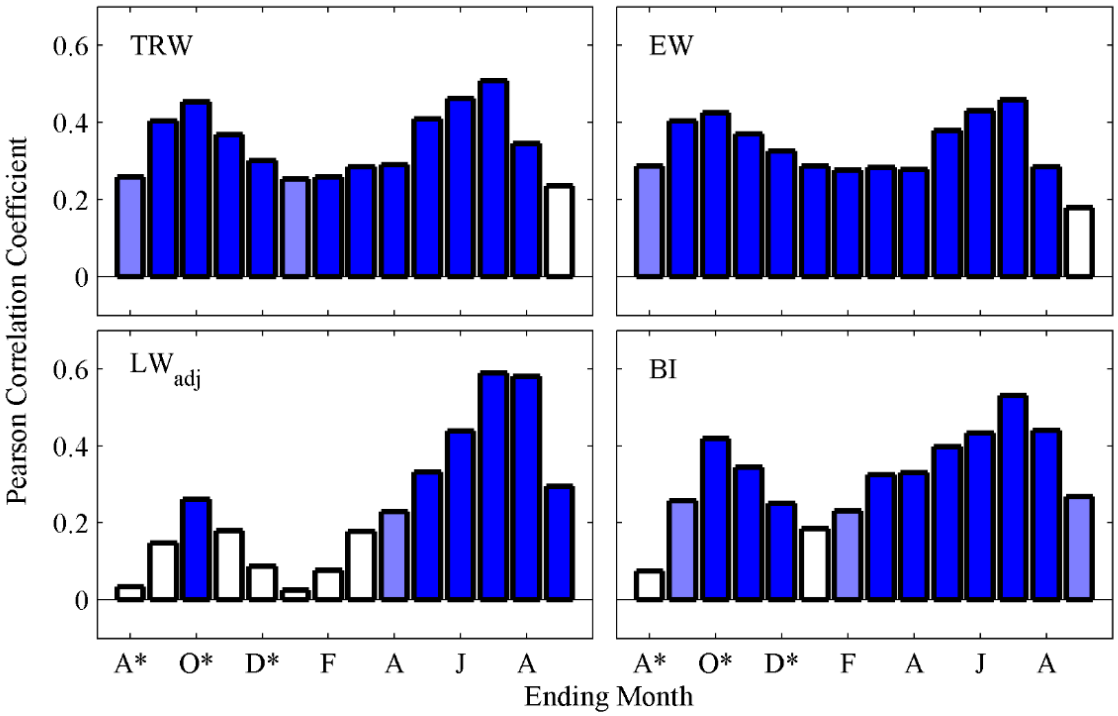


**Figure 2.2.** Pearson correlation coefficients between the first principal component of each tree-ring metric and 3-month precipitation composites (* = previous year). Dark blue shading indicates significance at a 99% level, and light blue shading indicates significance at a 95% level. Full Seascorr results (including correlations at different time-scales and with maximum temperature) are shown in Figure A5.

PC2 of each metric highlights differences in growth among the upper CRB sites, which generally reflect differing responses among the sites to winter precipitation (Figure 2.3; full Seascorr results in Figure A6). The second PC of TRW and EW are both positively

correlated with precipitation during the cool season and negatively correlated with warm-season precipitation. Seascorr results for TRW and EW chronologies at Sites 1 and 4 (not shown), which are both low elevation sites with positive loadings in PC2, differ substantially from the other sites. Whereas most sites correlate most strongly with warm-season precipitation with little dependence on cool-season precipitation, Sites 1 and 4 are most strongly correlated with precipitation from the previous autumn through early spring. The negative correlation between warm-season precipitation and PC2 of TRW and EW may reflect a lack of warm-season precipitation dependence at Sites 1 and 4, in combination with additional warm-season precipitation dependence at Site 2, which has negative loadings in PC2. In contrast, PC2 of $LW_{adj}$ contains very little cool-season precipitation signal and instead reflects warm-season precipitation in the year of growth, similar to PC1 of $LW_{adj}$. In general, PC2 of BI is not highly correlated to either cool-season or warm-season precipitation. As with PC1, there are very few significant correlations between PC2 and maximum temperature after accounting for the variance explained by precipitation (Figure A6). While I chose to use residual chronologies in this study, standard chronologies contain very similar seasonal precipitation signals for all four tree ring metrics (Figures A7-A8).

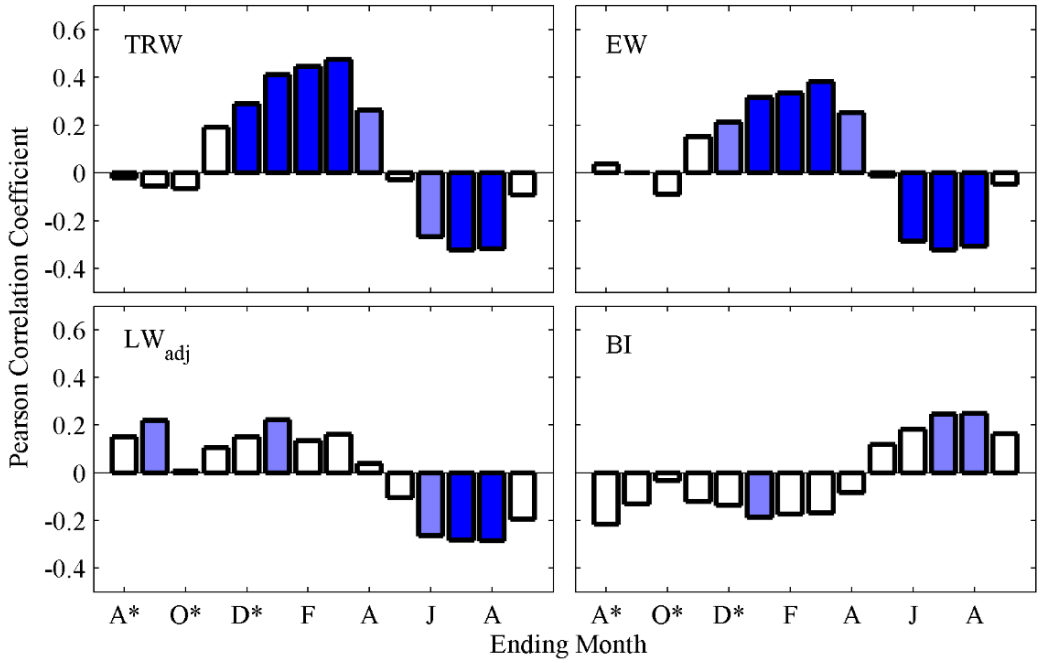


**Figure 2.3.** Pearson correlation coefficients between the second principal component of each tree-ring metric and 3-month precipitation composites (* = previous year). Dark blue shading indicates significance at a 99% level, and light blue shading indicates significance at a 95% level. Full Seascorr results (including correlations at different time-scales and with maximum temperature) are shown in Figure A6.

Effective correlation analyses between $P_{cool}$ and the 21 tree-ring metric composites indicate that the highest correlations ($r = 0.56$; Table 2.1) are achieved with a model that includes both PCs of TRW with no additional tree-ring metrics (Figure 2.4 a-b). In addition to being more parsimonious, the CPS model that includes only TRW is slightly more skillful ($R^2_{vs} = 0.12$) than the four metric composite ($R^2_{vs} = 0.11$) and successfully captures more of the extremely dry cool seasons ($EVC_{low} = 0.7$; $p < 0.001$) than the model that contains all four metrics ($EVC_{low} = 0.5$; $p < 0.01$). CPS models based on EW, $LW_{adj}$, or BI have no reconstructive skill ($R^2_{vs} < 0$) unless combined with at least one other metric. There is a distinct asymmetry in the sensitivity of the tree-ring composites to precipitation extremes: while most of the CPS models (except the one based solely on $LW_{adj}$) are able to capture a significant fraction of extremely dry cool seasons, none of the ponderosa pine composites are able to capture a significant proportion of extremely wet cool seasons.

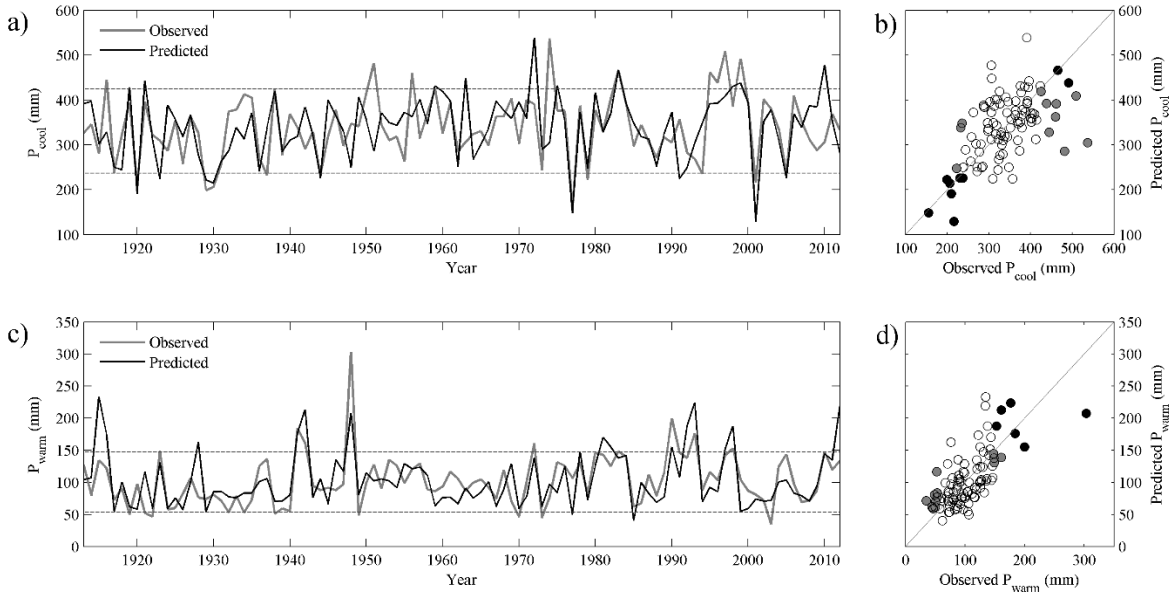


**Figure 2.4.** (a) Time plot of observed (grey) and predicted (black) October – March precipitation ($P_{cool}$) in the CRB based on a CPS model of TRW (both PC1 and PC2). Dashed horizontal lines show thresholds for identification of years with extreme precipitation. (b) Scatter plot of observed $P_{cool}$ and TRW-predicted $P_{cool}$. Filled circles indicate extreme years that were correctly identified (black) or not identified (gray) as extreme by the tree-ring CPS models. (c) Time plot of observed (grey) and predicted (black) May – August precipitation ($P_{warm}$) in the CRB based on a CPS model of EW and $LW_{adj}$ (both PC1 and PC2). Dashed horizontal lines show thresholds for identification of years with extreme precipitation. (d) Scatter plot of observed $P_{warm}$ and predicted $P_{warm}$. Filled circles indicate extreme years that were correctly identified (black) or not identified (gray) as extreme by the tree-ring CPS models.

Effective correlations between $P_{warm}$ and composites of ponderosa pine metrics (Table 2.2) indicate that warm-season precipitation is most strongly correlated with a composite containing both PCs of EW and $LW_{adj}$ ($r = 0.66$). While the individual metrics are each correlated with $P_{warm}$ with approximately equal strength ($0.51 \leq r \leq 0.57$), including TRW and BI along with EW and $LW_{adj}$ does not improve the overall correlation with $P_{warm}$. As suggested by the seasonal correlation analyses (Figures 2.2 and 2.3), the dominant signal in the network of CRB sites is related to warm-season precipitation, and the CPS skill for $P_{warm}$ therefore tends to be stronger than for $P_{cool}$. All COMBO composites exhibit at least some skill ($R^2_{vs} > 0$), though a CPS model composed of EW and $LW_{adj}$ (Figure 2.4 c-d) is

considerably more skillful than any individual metric. In contrast to the cool-season CPS tests, warm seasons that are extremely wet are successfully identified by most tree ring-based CPS models ($EVC_{high} \geq 0.4$; $p < 0.05$). Warm seasons that are extremely dry are poorly reflected in the CPS-predicted $P_{warm}$ ($EVC_{low} \leq 0.2$; $p > 0.05$). While the variance explained by the CPS model declines when BI is added to the EW + $LW_{adj}$ composite, the proportion of extremely wet warm seasons that are correctly identified by the CPS model increases from 60% to 80%.

**Discussion**

Results from this research demonstrate that different tree-ring metrics contain different seasonal precipitation signals in the upper CRB, particularly in their sensitivity to cool-season and prior growing season precipitation, though the dominant signals tend to reflect dependence on warm-season precipitation. In some cases, combining tree-ring metrics with complementary signals improves CPS model skill. Total ring width of *P. ponderosa* provides the strongest relationship to cool-season precipitation ($r^2 = 0.31$; $R^2_{vs} = 0.12$), and including additional tree-ring metrics does not improve the CPS model of $P_{cool}$. However, including multiple tree-ring metrics in a warm-season precipitation model offers substantial gains in model strength: while the best single tree-ring metric explains 32% of $P_{warm}$ variance, a model that includes both EW and $LW_{adj}$ explains 44% of $P_{warm}$ variance.

Like previous studies of sub-annual ring widths in western Canada and the U.S. Intermountain West [*Watson and Luckman*, 2002; *Crawford et al.*, 2015], there is very little evidence of temperature dependence in these tree-ring chronologies and substantial overlap in the EW and LW precipitation signals. While EW reflects precipitation in both the previous growing season and year of growth, LW reflects precipitation later in the year of growth. EW at these sites is also significantly correlated with cool-season precipitation, particularly at two

low elevation sites, which both have positive loadings in PC2 (Figures 2.3 and A2) and which are most strongly correlated with precipitation from autumn of the previous year through spring. The differences in precipitation signal between TRW/EW and $LW_{adj}$ may reflect the usage of stored photosynthate from the previous growing season for EW formation and the usage of photosynthate produced in the year of growth for LW formation [*Kagawa et al.*, 2006; *Offermann et al.*, 2011].

The signals embedded in these sub-annual ponderosa pine metrics differ from those found in other regions. In parts of the U.S. Southwest, for example, EW primarily reflects cool-season precipitation while LW tends to reflect warm-season precipitation delivered via the North American monsoon system [*Meko and Baisan*, 2001; *Stahle et al.*, 2009; *Griffin et al.*, 2013]. While previous studies have documented significant relationships between BI and warm-season temperature [*McCarroll et al.*, 2011; *Rydval et al.*, 2014; *Wilson et al.*, 2014], I found very little evidence of temperature dependence in the BI chronologies from the upper CRB (after accounting for the variance explained by precipitation).

The precipitation–tree growth relationships found in this study ($r^2 = 0.31$ for $P_{cool}$; $r^2 = 0.44$ for $P_{warm}$) compare favorably to those found in other studies of *P. ponderosa* in northwestern North America, where precipitation typically explains anywhere from 20-50% of total ring width variance depending on site and season of interest [*Graumlich*, 1987; *Kusnierczyk and Ettl*, 2002; *Knutson and Pyke*, 2008; *Knapp and Soulé*, 2011; *Soulé and Knapp*, 2011]. It is possible that model strength could be further improved through inclusion of tree-ring chronologies from other sites and species. Cool-season precipitation reconstructions in particular may benefit from inclusion of subalpine conifer species such as subalpine fir (*Abies lasiocarpa*) and mountain hemlock (*Tsuga mertensiana*) that are negatively correlated with winter precipitation and spring snowpack [*Peterson and Peterson*, 1994, 2001; *Peterson et al.*, 2002; *Lutz et al.*, 2012]. Like the *P. ponderosa* chronologies

developed in this study, Douglas-fir (*Pseudotsuga menziesii*) chronologies in northwestern North America are often strongly correlated with warm-season precipitation [*Watson and Luckman*, 2001; *Littell et al.*, 2008; *Lo et al.*, 2010; *Crawford et al.*, 2015], but with slight differences in seasonality [*Watson and Luckman*, 2002] which may complement the *P. ponderosa* warm-season precipitation signal and improve reconstruction of $P_{warm}$.

My results suggest that ponderosa pine metrics vary in their sensitivity to extreme precipitation in the U.S. Pacific Northwest. Among individual metrics, TRW successfully identifies 70% of extremely dry cool seasons, while $LW_{adj}$ only correctly identifies 10%. Likewise, CPS models based on $LW_{adj}$ are able to successfully identify 70% of extremely wet warm seasons, but none of the other three metrics correctly identify more than 50%. Tree ring-based predictions of warm-season precipitation are able to skillfully identify extremely wet years but not extremely dry years, while predictions of cool-season precipitation successfully capture extremely dry years but not extremely wet years. This suggests that inferences regarding extreme events from these models or comparison between extremes in the instrumental and paleoclimate records would be stronger for extremely wet years in the warm season but stronger for extremely dry years in the cool season. Asymmetries in the ability to capture extreme events may stem in part from asymmetries in the distributions of precipitation itself. For example, the distribution of warm-season precipitation (Figures 2.4 c-d) is highly skewed, with most years clustered near the lower end of the precipitation distribution. It may therefore be more difficult for tree-ring-based models to distinguish the driest years, which may be only slightly drier than other years that are not identified as extreme based on a 10% threshold. On the other hand, the wettest years are clearly separated from the bulk of the distribution and may therefore be easier to identify using tree-ring data since they are more distinct from the climatological norm. Quantifying the ability of reconstructions to capture extremes can improve interpretation of past climate through the

delineation of these strengths, weaknesses, and asymmetries in extreme value capture [*McCarroll et al.,* 2015].

**Summary and Conclusions**

Seasonal biases in tree-ring records remain a major challenge for the reconstruction and interpretation of past climates, particularly in the U.S. Pacific Northwest [*Steinman et al.*, 2012]. Previous studies have highlighted significant potential for improving seasonal climate reconstructions using combinations of multiple tree-ring metrics, including traditional TRW, sub-annual ring widths, and proxies for tree-ring latewood density. Using a network of TRW, EW, $LW_{adj}$, and BI chronologies from six *Pinus ponderosa* sites in and surrounding the upper CRB, I examined the sensitivities of these four ponderosa pine metrics to seasonal climate variability and evaluated the potential for sub-annual precipitation reconstruction using multiple metrics in the U.S. Pacific Northwest.

I found that all ring-width indices in this region are sensitive to warm-season precipitation, which is the season during which the least precipitation is received. In the upper CRB, TRW and EW are sensitive to warm-season precipitation in both the year of growth and in the previous growing season, while $LW_{adj}$ is not sensitive to conditions prior to the year of growth. Like previous studies in western Canada and the U.S. Intermountain West [*Watson and Luckman*, 2002; *Crawford et al.*, 2015], there is considerable seasonal overlap in the precipitation signals embedded in TRW, EW, and $LW_{adj}$, but peak correlations between warm-season precipitation and $LW_{adj}$ are stronger than other metrics and occur later in the growing season. Like *Watson and Luckman* [2002], I also identified positive and significant correlations between TRW and EW indices and cool-season precipitation at some sites. The BI signal in the upper CRB is similar to the ring-width metrics, with the first component containing a warm-season precipitation signal (in both the year of growth and in the prior

growing season). Unlike previous studies in Scandinavia [*McCarroll et al.*, 2011] and British Columbia [*Wilson et al.*, 2014], I did not find a strong relationship between BI and temperature in my semi-arid study region.

Effective correlation analyses and CPS tests suggest that use of multiple tree-ring metrics may improve seasonal precipitation reconstructions, though the magnitude of improvement may differ depending on the season of interest. In my study area, for example, TRW alone can explain more cool-season precipitation variance than all metrics combined. A composite index of EW and $LW_{adj}$ explains substantially more variance in warm-season precipitation than any single metric, thus highlighting the potential to capture seasonal climate signals embedded in sub-annual ring widths that are not resolvable by TRW alone. CPS tests suggest that reconstructions of $P_{cool}$ and $P_{warm}$ in the upper CRB are asymmetric in their ability to capture extreme events. While CPS-predicted $P_{cool}$ successfully identifies extremely dry years, there is very little skill in predicting extremely wet years. In contrast, the CPS model skillfully predicts extremely wet warm seasons, but not extremely dry ones. This asymmetry in the ability of CPS models to capture precipitation extremes suggests that future paleoclimate studies from other proxy records may benefit by using EVC as a validation metric to formally test the ability of variance-scaled reconstructions to correctly identify extreme events. Seasonal climate reconstruction and the capture of extremes in the tree-ring record may also benefit from future research to include stable isotope ratios of tree-ring cellulose as an additional metric and from the inclusion of chronologies from multiple species.

My results suggest that tree growth in the U.S. Pacific Northwest may be sensitive to the enhanced precipitation seasonality that is expected under a changing climate [*Mote and Salathé*, 2010; *Rogers et al.*, 2011]. Projected changes in the seasonality and phase of precipitation, in combination with higher summer temperatures and increases in vapor

pressure deficit, pose significant threats to vegetated ecosystems that rely on winter snowpack for soil moisture recharge [*Boisvenue and Running*, 2010; *Williams et al.*, 2013]. Substantial uncertainties in the responses and feedbacks of vegetation to the impacts of climate change limit our ability to project future changes in the distribution and functioning of terrestrial ecosystems. Empirical studies on the responses of tree growth to historical variation of temperature and water availability can constrain these models and improve our understanding of the potential responses of forest ecosystems to climate change [*Moorcroft*, 2006]. While tree growth at the six sites used in this study seems to be primarily limited by summer water availability, there is substantial variation among sites in their reliance on winter precipitation. Growth at Sites 1 and 4, for example, is significantly related to precipitation from the previous autumn through early spring. These results suggest that the impacts of shifting precipitation seasonality, as expected under a changing climate, on the forests of the U.S. Pacific Northwest will likely vary geographically due to differential reliance of forests on precipitation from different seasons. Where tree growth is primarily dependent on summer precipitation, as in most of my study sites, redistribution of precipitation from the warm to the cool season may result in long-term growth declines. The impacts of seasonal precipitation redistribution would likely be less severe for forests that partially rely on winter precipitation as an additional source of water availability, such as my Sites 1 and 4, though changes in the phase of precipitation may pose additional risks for these ecosystems that are not examined in this study. Continued research on the consequences of seasonal hydroclimate shifts for terrestrial ecosystems that combines inferences from tree-ring networks (or other sources of information on forest growth, such as remote sensing or eddy covariance flux towers) with 21$^{st}$ century climate projections [e.g., *Williams et al.*, 2013] will help delineate these differing responses.

# CHAPTER 3: ENVIRONMENTAL STRESSES TO PRIMARY PRODUCTION IN THE CONTERMINOUS UNITED STATES

## Introduction

Terrestrial primary production—the amount of carbon sequestered by plants via photosynthesis—is the fundamental source of food for all land-dwelling organisms and the primary entry point of energy and carbon into ecosystems. Recent estimates suggest around 80% of available primary production has already been appropriated for human use, with the remainder representing a key "planetary boundary" for future human activity [*Running*, 2012]. Terrestrial primary production is also a major component of the global carbon cycle, which has historically acted as a large sink for human emissions of $CO_2$ [*Pan et al.*, 2011; *Ciais et al.*, 2013].

Many environmental factors plays an important role in regulating the growth and productivity of terrestrial vegetation, including climate, soil quality, and ecological processes (e.g., disturbance, competition, and succession) [*Chapin et al.*, 2011]. Productivity of terrestrial vegetation can be limited or co-limited by multiple climate or environmental factors, with high spatial and temporal variability in the dominant environmental stressors [*Nemani et al.*, 2003; *Garbulsky et al.*, 2010]. Projected changes in temperature and hydroclimate over the 21$^{st}$ century will likely alter environmental stress regimes and thus impact the primary production of the biosphere [*Boisvenue and Running*, 2010; *Rogers et al.*, 2011; *Notaro et al.*, 2012; *Jiang et al.*, 2013], and many models suggest that the terrestrial biosphere will switch from a net sink to a net source of $CO_2$ in response to these changes [*Settele et al.*, 2014]. Understanding the environmental factors that control primary

production at a range of spatial and temporal scales is therefore crucial for modeling and monitoring primary production and for projecting responses of plant growth and productivity to future climate change.

The complexity of environmental limitations to plant growth—as well as their interactions with each other and their importance over different spatial and temporal scales—adds considerable uncertainty to models that attempt to monitor primary production based on satellite data. The dominant paradigm for modeling primary production with remote sensing is light-use efficiency (LUE) theory, which estimates plant production as a function of the amount of absorbed photosynthetically active radiation (PAR) by plant canopies and their efficiency at converting absorbed PAR to carbohydrates [*Monteith*, 1972, 1977, *Song et al.*, 2013, 2015]. Many of these models assume a constant optimal LUE that is reduced in response to "environmental stresses," which are typically based on relatively simple functions of easily measured meteorological variables, such as temperature and vapor pressure deficit.

While these environmental stress functions can capture stress-induced reductions in LUE in some regions, they may be poorly correlated (or even opposite in sign) in other ecosystems [*Garbulsky et al.*, 2010; *Zhang et al.*, 2015]. Differences in primary production estimates derived from remotely sensed data can partly be traced to differences in the parameterization of these environmental stress scalars [*Cai et al.*, 2014]. Estimating water stress is particularly challenging [*Zhang et al.*, 2015], especially in arid and semi-arid regions and during periods of extreme drought [*Leuning et al.*, 2005; *Gebremichael and Barros*, 2006; *Heinsch et al.*, 2006; *Pan et al.*, 2006; *Mu et al.*, 2007; *Nightingale et al.*, 2007; *Zhang et al.*, 2007a; *Hwang et al.*, 2008; *Kanniah et al.*, 2009]. Additionally, few LUE models incorporate stresses resulting from non-climatic factors, such as topographic position, insufficient nutrient supply, or other ecological factors (e.g., competition for belowground resources). Since nutrient supply is particularly important for the physiological processes that

drive light-use efficiency, inclusion of soil quality factors in LUE models could lead to substantial improvements in primary production estimates [*Nightingale et al.*, 2007], though soil data availability and quality would likely present a challenge for large-scale implementation.

Given the limitations of current environmental stress models, in this chapter I develop an alternative approach for quantifying environmental stress effects on forest primary production using tree-ring data and examine the drivers and seasonality of environmental stresses to forest primary production in the conterminous U.S. Widths of tree rings are a direct indicator of the net primary production that is allocated to woody growth [*Graumlich et al.*, 1989; *Rathgeber et al.*, 2000], and the sensitivity of stomatal, photosynthetic, and cambial processes to variation in each tree's local environment make tree-ring widths ideal indicators of long-term variation in forest productivity and environmental stress [*Fritts*, 1976]. Recent studies have demonstrated significant potential for using tree-ring metrics as indicators of ecosystem-scale productivity [*Beck et al.*, 2013; *Bunn et al.*, 2013], suggesting that carbon cycle models (including those based on remotely sensed data) may benefit from assimilation of tree rings [*Babst et al.*, 2014].

Here, I estimate annual environmental stress effects on plant growth based on tree-ring widths, species traits, and ecological theory developed for forest gap models. I define "environmental stress" as the proportion of the theoretical optimal diameter growth rate that is realized in a given year. I first test and evaluate the index at six tree-ring sites in the U.S. Pacific Northwest (described in Chapter 2) with detailed tree- and site-level data. I then apply the method to a large, continent-wide network of tree-ring widths in the conterminous U.S. and compare it to annual gross primary production from nearby flux tower sites. Finally, I use the tree-ring environmental stress index to assess the specific environmental factors that limit

forest growth in the conterminous U.S., including stresses induced by unfavorable climatic, topographic, and edaphic conditions.

## Data and Methods

### *A Tree-Ring Based Environmental Stress Index*

At its core, "environmental stress" is the reduction of plant growth below optimal levels in response to inadequate resource availability or unfavorable ambient conditions. Where measurements of annual tree growth are available, the effects of environmental stress can therefore be represented as the ratio between the actual, measured diameter growth in a given year and the theoretical optimal diameter growth rate in that same year. While actual tree growth is easily measured using standard dendrochronological procedures, optimal growth is a theoretical construct that cannot be directly measured but must be estimated using species-specific allometric equations such as those used in forest gap models [e.g., *Botkin et al.*, 1972; *Shugart*, 1984; *Urban et al.*, 1993; *Song and Woodcock*, 2003]. The approach used here is the inverse of typical gap model applications: while I am estimating the impacts of environmental stress using actual measurements of tree growth, forest gap models typically simulate growth and succession of forests based on modeled environmental stresses (e.g., light, nutrients, and water availability).

To estimate the optimal growth of a given tree in a given year, I follow the approach originally proposed for the JABOWA gap model [*Botkin et al.*, 1972]:

$$\Delta D_{opt} = \frac{GD[1-DH/D_{max}H_{max}]}{274+3b_2D-4b_3D^2}, \quad (1)$$

Where $\Delta D_{opt}$ is the optimal diameter growth (in cm) for a given tree in a given year, $G$ is a species-specific growth factor, $D$ is the diameter at breast height (DBH) at the start of the year, $H$ is the height of a given tree at the start of the year, $D_{max}$ is the maximum DBH of the tree species, $H_{max}$ is the maximum height of the tree species, and $b_2$ and $b_3$ are species-

specific allometric parameters. This formula assumes: 1) that annual volume increment is proportional to canopy leaf area (which is itself proportional to stem sapwood area), and 2) that there is an increasing maintenance cost with increasing tree size (i.e., as $D$ approaches $D_{max}$, volume increment approaches zero) [*Botkin et al.*, 1972; *Shugart*, 1984]. I estimated $D_{max}$, $H_{max}$, and maximum age based on the maximum observed DBH, height, and age for each species provided in *Hardin et al.* [2001], supplemented with information from the gap model literature [*Shugart*, 1984; *Urban et al.*, 1993]. I estimated the remaining parameters ($G$, $b_2$, and $b_3$) using equations provided in *Shugart* [1984]. A full list of species and parameters used in this model is provided in Table A4.

For application to tree-ring datasets, where *in situ* measurements of DBH are not typically available, $D$ must be estimated using an "inside-out" approach, in which stem diameter at the start of a given year is estimated by summing all diameter increments prior to that year ($D^*$). $D^*$ can then be substituted for $D$ in eqn. 1, resulting in an estimated optimal growth rate ($\Delta D^*_{opt}$). Estimating diameters in this manner will systematically underestimate annual stem diameters, which I address below. As in many gap models, I estimate $H$ as a species-specific quadratic function of $D^*$.

Following estimation of $\Delta D^*_{opt}$, the environmental stress index, $S^*$, for a given year is estimated for each tree as the ratio of measured diameter growth ($\Delta D$) to the estimated optimal diameter growth rate:

$$S^* = \frac{\Delta D}{\Delta D^*_{opt}}. \quad (2)$$

Annual site-level $S^*$ chronologies are then developed by averaging all core-level $S^*$ series at a given site using Tukey's biweight robust mean. Following accepted dendrochronological practice, I use an expressed population signal (EPS) threshold of 0.85 to exclude years with inadequate signal strength from any further analyses [*Wigley et al.*, 1984]. Theoretically, $S^*$ should be in the range [0,1], and it should capture and integrate the dominant sources of

environmental stress experienced by trees, including both interannual variation in stress resulting from climate variability as well as perennial sources of stress resulting from unfavorable site conditions (e.g., steep slopes or poor soil nutrient status).

For comparison, I also define a relative stress index ($S_r$) using methods standard to dendrochronology. Following typical detrending methods, I fit stiff smoothing splines (two-thirds the length of the series with a 50% frequency response) to the measured ring widths from each individual core, and divided this fitted curve into the measured ring width series to obtain a detrended ring width index [*Cook*, 1985]. As with $S^*$, I averaged the detrended ring width index series at each site using Tukey's biweight robust mean to obtain site-level $S_r$, retaining only the portions of the time-series that exceed an EPS of 0.85 [*Wigley et al.*, 1984]. Unlike $S^*$, this relative stress index has the same mean across all sites and only represents the interannual variation in stress experienced by trees. It therefore cannot capture spatial gradients in stress resulting from perennial reductions in growth due to unfavorable site conditions, but it also does not suffer from uncertainties introduced by the optimal growth model.

*Tree-Ring Data*

I tested the errors introduced to $\Delta D^*_{opt}$ and $S^*$ due to systematic underestimation of annual DBH using increment cores collected at six semi-arid ponderosa pine sites in the U.S. Pacific Northwest (Chapter 2; Figure A9), where DBH was measured for each tree at the time it was sampled. Cores were collected, processed, and cross-dated following standard dendrochronological procedures [*Stokes and Smiley*, 1968]. Ring widths were measured on a Velmex measuring system, and cross-dating was verified using the program COFECHA [*Grissino-Mayer*, 2001]. Ring width series were processed using the dplR package [*Bunn*, 2008] in the R statistical environment [*R Core Team*, 2014].

For continental-scale application of the tree-ring environmental stress index, I obtained tree-ring widths from the International Tree-Ring Data Bank (ITRDB) for all sites in the conterminous U.S. that at least partially overlap with the period 1980-present (Figure 3.1). Globally, the ITRDB contains ring width records for more than 3,200 sites, with particularly high sampling density within North America and western Europe [*St. George*, 2014]. In the conterminous U.S., there are more than 1,000 sites that overlap with the AVHRR remote sensing record (a total of more than 12,000 site-years of tree-ring widths) and approximately 300 that overlap with the MODIS record (2000-present). Of the ITRDB sites used in this study, the most prominent genera are *Pinus* (35% of the sites, mostly ponderosa pine), *Quercus* (23%, largely white oak and post oak), and *Pseudotsuga* (12%), though other genera are also present, including *Tsuga* (9%), *Abies* (4%), *Picea* (4%), *Juniperus* (4%), *Taxodium* (3%), *Larix* (1%), and *Liriodendron* (1%).

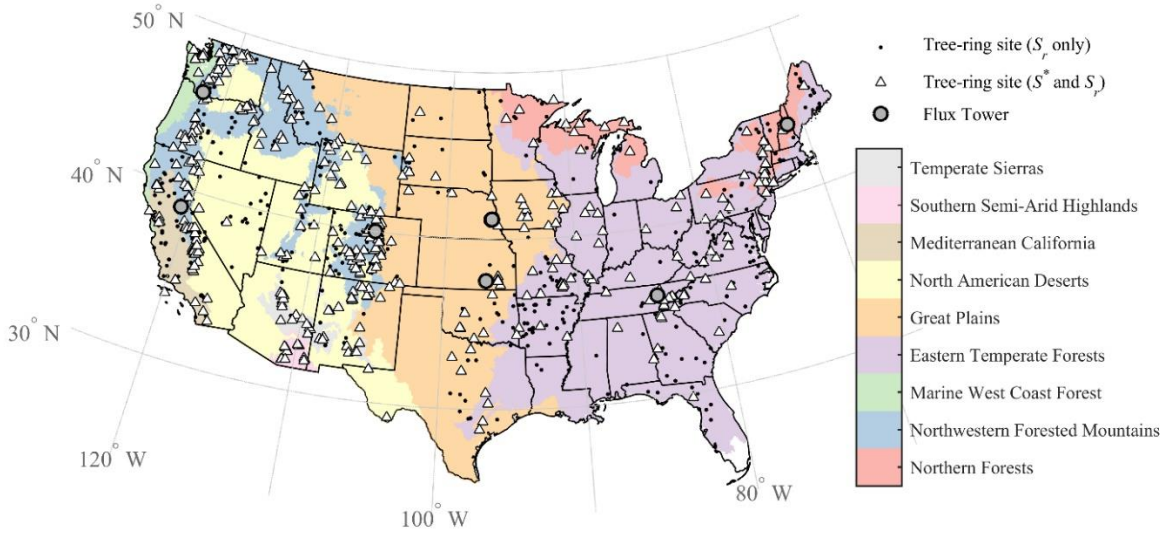


**Figure 3.1.** Level I ecoregions and distribution of tree-ring sites and flux towers used in this study. Open triangles show sites for which I was able to estimate both $S^*$ and $S_r$, and black dots show sites for which I was only able to estimate $S_r$. The AmeriFlux eddy covariance flux towers used in this study are shown as outlined gray circles.

*Evaluation of Tree-Ring Environmental Stress Estimates*

Any uncertainty in ring-width-based estimates of $D^*$ will propagate to estimates of both $\Delta D^*_{opt}$ and $S^*$. When increment cores extend to the pith of the tree (Figure A10a), this approach should provide relatively accurate estimates of annual tree diameter. However, it is likely to underestimate stem diameter in most cases for two reasons: 1) the width-based estimate does not include bark (which should have a minimal impact on diameter increment estimates), and 2) most increment cores do not extend to the pith of the tree due either to an off-center angle of the increment borer when it enter the tree (Figure A10b) or to heartwood rot in the center of the tree (Figure A10c). In these cases, the innermost portion of the tree will not be included in the diameter estimate. However, these uncertainties are mitigated by two factors. First, both of the above sources of error in $D^*$ are additive in nature. Thus, as trees age and stem diameter increases, the error in $D^*$ becomes proportionally smaller. Second, annual diameter growth generally decreases as trees age so $D^*$ changes little from year to year. While $\Delta D^*_{opt}$ increases rapidly in the early years of growth, it remains relatively constant thereafter. For applications involving relatively old trees where the recent past is of primary interest, the fact that $\Delta D^*_{opt}$ remains relatively constant reduces the impact of errors in $D^*$.

Using measured DBH at the six ponderosa pine sites in the Pacific Northwest, I evaluated the error introduced to $\Delta D^*_{opt}$ and $S^*$ when using the biased "inside-out" $D^*$ estimates. For each tree at these sites, I calculated $D$ based on measured DBH using an "outside-in" approach, wherein stem diameter in a given year is estimated by subtracting subsequent diameter increments from the measured DBH. Since DBH was accurately measured *in situ* at the time of sampling, these estimates of $D$ should be more accurate and should not suffer from the systematic underestimation of $D^*$ from the "inside-out" approach. This method still assumes that growth is homogeneous around the circumference of the tree,

that the extracted core is a representative sample of this growth, and that increment cores were extracted at breast height. In some cases, when growth is asymmetric around the circumference of the tree and increment cores extended near the pith of the tree, the "outside-in" method may result in negative diameter estimates in early years of growth. These were corrected by linearly scaling the $D$ time-series for these trees to range from 0 cm to DBH. I calculated both $\Delta D_{opt}$ and $S$ using these "outside-in" estimates of $D$, and compared them to the estimates based on the biased "inside-out" estimates of $D^*$. I acknowledge, however, that these tests are based solely on a single species (ponderosa pine) from a single region (the U.S. Pacific Northwest) for which *in situ* DBH measurements are available. A priority for future research is to perform this sensitivity test using additional species from different regions.

To assess the ability of $S^*$ to capture variation of primary production at a continental scale, I compared $S^*$ calculated at ITRDB sites to annual gross primary production (GPP) estimates from eddy covariance flux towers within 100 km of the tree-ring site (Figure 3.1). While this distance will likely result in comparisons between flux sites and ITRDB sites that are in different physiographic settings, a large search radius was needed in order to achieve a large enough sample size, since flux sites and tree-ring sites are not typically located very close to each other. In this dataset, for example, the minimum distance between a flux tower and a tree-ring site was approximately 24 km. However, significant correlations between the environmental stress index derived from tree rings and GPP estimated at flux towers would suggest that the index is adequately capturing the environmental stresses that influence primary production at a broad scale. For each flux tower, I obtained daily, level 4 GPP estimates from the AmeriFlux network (http://ameriflux.ornl.gov/) and calculated annual GPP as the sum of daily GPP over the calendar year. I excluded any year with missing level 4 daily data or which consisted of more than 25% gap-filled estimates.

*Climate, topography and soil data*

I assessed the responses of the tree-ring environmental stress indices to climatic, topographic, and soil factors. To understand climatic limitations to growth, I used mean monthly minimum temperatures (TMIN), mean monthly maximum temperatures (TMAX), mean monthly vapor pressure deficit (VPD), and a simple climatic water balance (WB) estimate, defined here as total monthly precipitation minus monthly potential evapotranspiration calculated using the FAO Penman-Monteith approach [*Monteith*, 1965; *Allen et al.*, 1998]. All climate data were obtained from the Parameter-elevation Relationships on Independent Slopes Model (PRISM) [*Daly et al.*, 2008] at approximately 4 km spatial resolution. Each of the monthly climate variables were aggregated to seasonal time-scales by taking the mean of the two temperature variables and summing the two water variables over four three-month seasons: September-November (SON) of the previous year, December-February (DJF) ending in the year of growth, March-May (MAM), and June-August (JJA).

Four topographic indicators were obtained at 1 km resolution from the USGS HYDRO1k dataset: elevation, slope, upslope accumulated area (UAA), and the topographic wetness index (TWI). UAA represents the total upslope surface area that could contribute runoff to a given point, while TWI adjusts UAA by the local slope to better capture the tendency of water to accumulate in a given area [*Beven and Kirkby*, 1979]. As indicators of soil texture and quality, I used six metrics from the gridded Global Soil Dataset for use in Earth System Models (GSDE) [*Wei et al.*, 2014]: proportions of the soil made up by sand, silt, and clay; acidity (pH); organic carbon content; and total nitrogen. For consistency, the 1 km gridded topographic and soil data were aggregated to the same spatial resolution as the climate data (4 km).

*Modeling the Environmental Drivers of Stress*

To assess the drivers of environmental stress in the conterminous U.S., I conducted a set of modeling experiments (Figure 3.2; Table 3.1) at three spatial scales within the spatially-hierarchical EPA ecoregion dataset [*Omernik*, 1987]: a coarse spatial scale (Level I; Figure 3.1), a medium spatial scale (Level II), and a fine spatial scale (Level III). Within each ecoregion, I located all tree-ring sites that fell within its bounds and pooled the annual stress indices from those sites into a single ecoregion-level attribute table. I also extracted the climatic, topographic, and soil information from the grid cell nearest to each site to use as predictor variables for the environmental stress model. To ensure that both temporal and spatial variability of environmental stress are captured within the modeling experiments, I used all environmental stress estimates from 1971 through the end of the tree-ring series (all of which end in 1980 or later), thus ensuring that each site within the ecoregion-level model has at least ten years of stress measurements included. The ecoregion-level attribute tables therefore contain variables that vary spatially (topography and soil variables) and that vary both spatially and temporally ($S^*$ and climate variables).

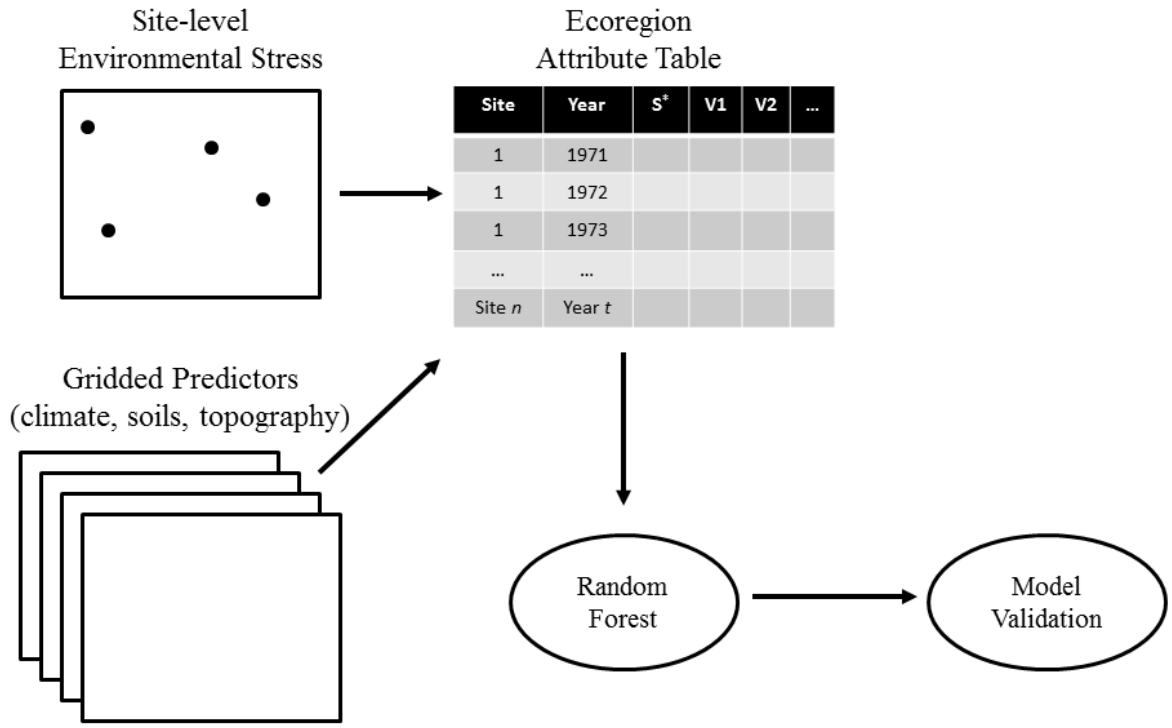


**Figure 3.2.** Flow chart of ecoregion-level environmental stress models. All site-level, annual environmental stress time-series, along with their associated climatic, topographic, and soil predictors (V1, V2, etc.), are pooled into a single ecoregion-level attribute table. This attribute table is used to train an ecoregion-level random forest (RF) regression model to predict environmental stress as a function of environmental factors, with approximately two-thirds of the data used to train the model and one-third left "out of bag" for evaluation.

After the ecoregion-level attribute tables were assembled, I used a series of random forest (RF) regression model experiments to assess the dominant drivers of environmental stress across the conterminous U.S. The RF machine learning method consists of a large ensemble of regression trees (here, I use 300 regression trees), in which each tree is "grown" using a random subset of observations and predictor variables [*Breiman*, 2001]. The RF method provides several desirable characteristics compared to other regression methods: they are not as susceptible to overfitting [*Breiman*, 2001; *Pal*, 2005; *Gislason et al.*, 2006; *Prasad et al.*, 2006], they are well suited for modeling nonlinearity and interactions among predictor variables [*Cutler et al.*, 2007], and they are relatively insensitive to noise and multicollinearity in predictor variables [*Breiman*, 2001; *Gislason et al.*, 2006]. The

environmental stress model experiments consisted of four RF models per ecoregion, each utilizing a different subset of predictor variables (Table 3.1): one model using climate only (C), one using soil and climate (SC), one using topography and climate (TC), and one using all predictors (TSC). The same modeling procedure was repeated using the relative tree-ring stress index ($S_r$), which varies temporally but has the same mean across all sites.

**Table 3.1.** Structure of the random forest model experiments.

| | Topography | Soil | Climate |
|---|---|---|---|
| C | | | x |
| SC | | x | x |
| TC | x | | x |
| TSC | x | x | x |

To assess the relative importance of climatic, topographic, and soil sources of environmental stress, I calculated the coefficient of determination ($r^2$) for each RF model using observations that were left "out of bag" (i.e., observations withheld from model calibration). For each "tree" in the random forest, approximately two-thirds of the observations were used for training, while the remaining observations were withheld for evaluation. To ensure that enough observations were present within each ecoregion, I only fit RF models for ecoregions that included at least 75 site-years of environmental stress estimates (i.e., approximately 50 for training and 25 for evaluation). In the conterminous U.S., all Level I ecoregions except Tropical Wet Forests (the southernmost tip of Florida) contained at least 75 site-years of environmental stress estimates (Figure A11). Many of the finer scale Level II and III ecoregions (e.g., Warm Deserts) did not include a sufficient number of observations (Figure A11) and were therefore excluded from further analyses. The full lists of ecoregions used in this study can be found in Tables A5 and A6 of Appendix 2. To further assess the seasonal climate drivers of stress, I also calculated Spearman's rank correlation coefficient ($\rho$) between the tree-ring environmental stress estimates and each

climate variable for each of the four seasons. These correlations were calculated at the level of whole ecoregions. In other words, the correlations were calculated using all site-years of environmental stress (and the climate variable corresponding to each environmental stress site-year) within a given ecoregion.

## Results

*Evaluation of the Tree-Ring Environmental Stress Index*

At the six ponderosa pine sites in the Pacific Northwest, DBH estimates based on the "inside-out" approach were biased relative to the measured DBH (Figure A12). While the "inside-out" estimates of DBH were significantly correlated with the *in situ* measurements of DBH (Spearman's $\rho = 0.56$; $n = 276$), they were consistently underestimated (mean bias = −23.9 cm; median bias = −19.4 cm). In extreme cases, the ring-width estimated diameters were underestimated by more than 50 cm. Diameters were very rarely overestimated, and these occurrences likely reflected rare cases where the increment core extended very near to pith and where increment cores were taken at a different height than the DBH measurement or where growth was asymmetric around the circumference of the tree.

The persistent low biases in $D^*$ estimates contributed to substantial biases in $\Delta D^*_{opt}$, but only in the early years of growth (Table 3.2; Figure A13). For $D^* = [0, 20]$ cm, $\Delta D^*_{opt}$ was underestimated with extreme outliers exceeding biases of 1 cm. Once $D^*$ exceeded 30 cm, estimates of $\Delta D^*_{opt}$ at the six ponderosa pine sites were relatively unbiased compared to estimates based on measured diameter. Beyond this diameter threshold, median differences between $\Delta D^*_{opt}$ and $\Delta D_{opt}$ never exceeded 0.01 cm and remained nearly unbiased for the remainder of the lifespan of the trees. Even the most extreme outliers never exceeded a bias of more than 0.05 cm.

**Table 3.2.** Median bias in $\Delta D^*_{opt}$ and $S^*$ for different diameter classes.

| $D^*$ (cm) | n | $\Delta D^*_{opt}$ (cm) | $S^*$ |
|---|---|---|---|
| [0,10] | 11701 | -0.086 | 0.155 |
| (10,20] | 12258 | -0.032 | 0.039 |
| (20,30] | 13292 | -0.016 | 0.016 |
| (30,40] | 13473 | -0.009 | 0.008 |
| (40,50] | 12719 | -0.004 | 0.003 |
| (50,60] | 10941 | 0.000 | 0.000 |
| (60,70] | 7259 | 0.002 | -0.001 |
| (70,80] | 3094 | 0.005 | -0.003 |
| (80,90] | 1248 | 0.005 | -0.004 |
| (90,100] | 331 | 0.005 | -0.003 |
| (100,110] | 84 | 0.004 | -0.003 |

The underestimation of $\Delta D^*_{opt}$ during the early years of growth propagated into overestimation $S^*$ in the early years of growth (Table 3.2; Figure A14). When $D^*$ was less than 30 cm, the magnitude of environmental stresses experienced by trees were substantially underestimated in most cases (i.e., $S^* > S$). When $D^*$ exceeded 30 cm, median biases were consistently near zero (never exceeding ±0.01), but with some extreme outliers where the environmental stresses experienced by trees were substantially overestimated (i.e., $S^* < S$).

Based on the evaluation of $S^*$ chronologies in the Pacific Northwest (Table 3.2; Figures A13-A14), I applied the environmental stress model to ITRDB tree-ring sites, excluding any years with $D^* < 30$ cm. While this threshold is based on only a single tree species from one region, *in situ* DBH measurements are unavailable from other tree-ring sites, which limits my ability to test the sensitivity of other tree species to bias in ring-width based $D^*$ estimates. Of the tree-ring sites in the conterminous U.S. that extend into the 1980s, 462 $S^*$ chronologies could be developed after removing sites where species-specific parameters could not be determined, where inadequate sample sizes and inter-series correlations prevented an adequate signal strength (EPS < 0.85), and where there were too few trees with $D^* > 30$ cm. The $S_r$ dataset, meanwhile, included 1,145 tree-ring sites.

Annual $S^*$ of ITRDB sites was positively and significantly correlated with the annual GPP of nearby flux towers. For sites within a 100 km radius, correlations between annual $S^*$ and annual GPP were $\rho$=0.48 (Figure 3.3; p<0.01). The relationship was stronger when the flux tower and tree-ring site were within 25 km of each other (Spearman's $\rho$=0.79; p<0.01), but only two tree-ring sites met this criterion.

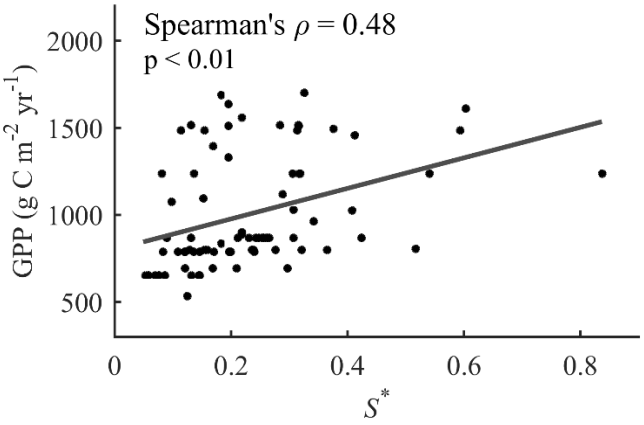


**Figure 3.3.** Relationship between annual $S^*$ and annual GPP at flux towers within 100 km of tree-ring sites.

*Environmental Drivers of Stress*

Correlations between $S^*$ and TMIN and TMAX indicate that ecoregions of the conterminous U.S. generally respond negatively to higher temperatures (Figure 3.4), with notable exceptions near the Great Lakes, New England, and along the west coast. The drier intermountain ecoregions of the western U.S. in particular exhibit relatively strong negative correlations to TMIN in spring and summer (MAM and JJA, respectively) and to TMAX across all four seasons, likely due to the positive relationship between temperature and evaporative demand. Correlations between $S_r$ and temperature at the ecoregion scale are generally weaker (particularly for TMIN), though this index remains negatively correlated with TMAX throughout much of the U.S., especially with spring (MAM) TMAX in the western U.S. and summer (JJA) TMAX in the eastern U.S. (Figure A15). There are very few ecoregions in which $S_r$ is positively correlated with TMAX.

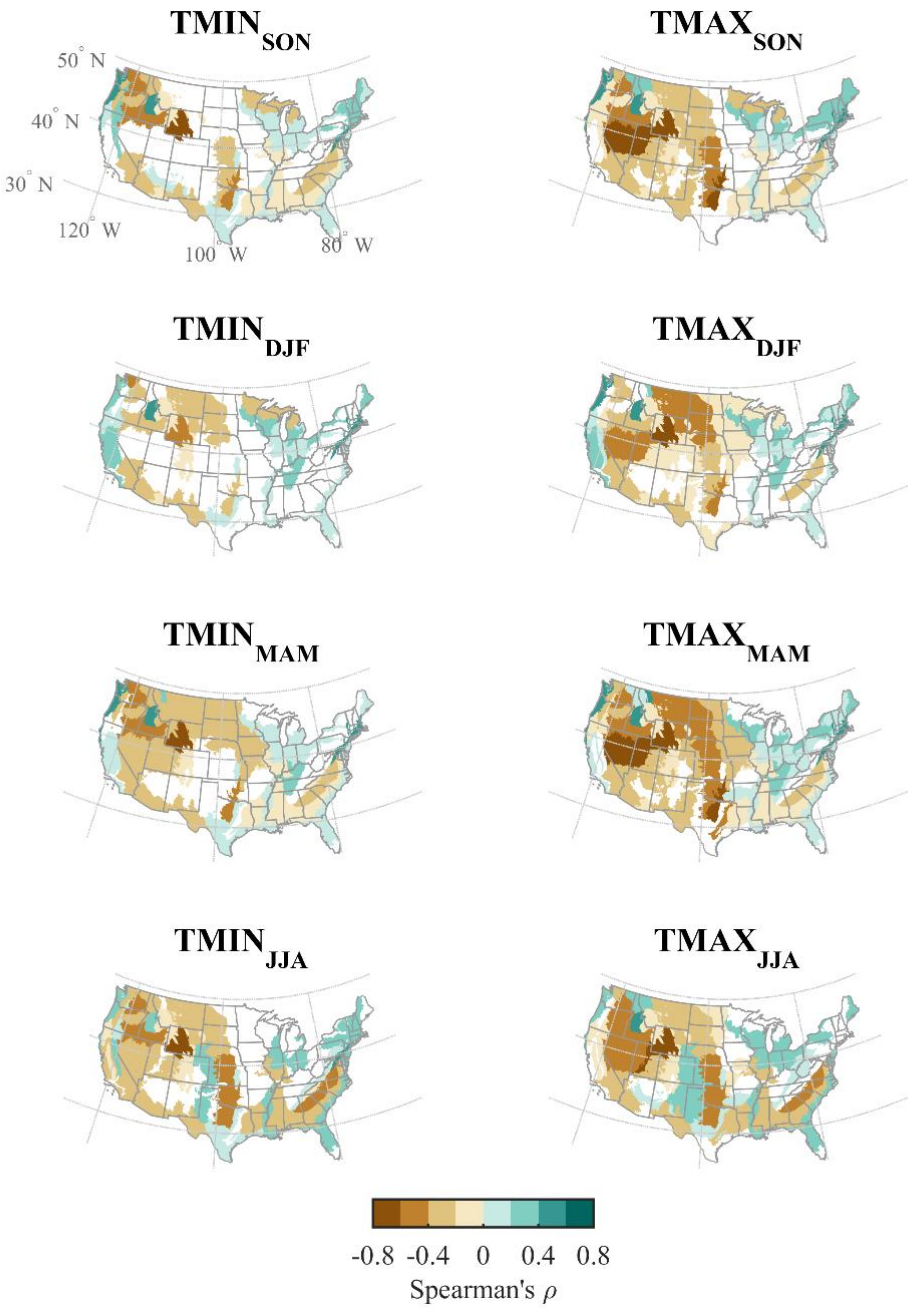


**Figure 3.4.** Spearman's rank correlation coefficient ($\rho$) between $S^*$ and seasonal minimum (TMIN) and maximum (TMAX) temperatures. Only ecoregions with significant correlations ($p<0.05$) are shown.

Correlations between $S^*$ and WB are positive and significant throughout the western U.S. (Figure 3.5). Notably, growth in the western U.S. tends to be most strongly correlated with WB from autumn of the previous year (SON) through spring in the year of growth (MAM), rather than with WB during the growing season. $S^*$ is negatively correlated with

VPD throughout much of the U.S., particularly west of the Mississippi River, where $S^*$ tends to be negatively correlated with VPD during all four seasons. In ecoregions of the Great Lakes and New England, $S^*$ tends to be positively, rather than negatively, correlated with VPD from autumn of the previous year (SON) through spring in the year of growth (MAM), likely due to the positive relationship between VPD and temperature, which can be a limiting factor in these ecoregions (as seen in Figure 3.4). Of ecoregions in the eastern U.S., those in the southeast exhibit the strongest correlations between $S^*$ and water variables, with positive correlations to summer (JJA) water balance and negative correlations to VPD. Correlations between $S_r$ and water variables are generally similar to those for $S^*$, though the correlations tend to be weaker in most ecoregions (Figure A16).

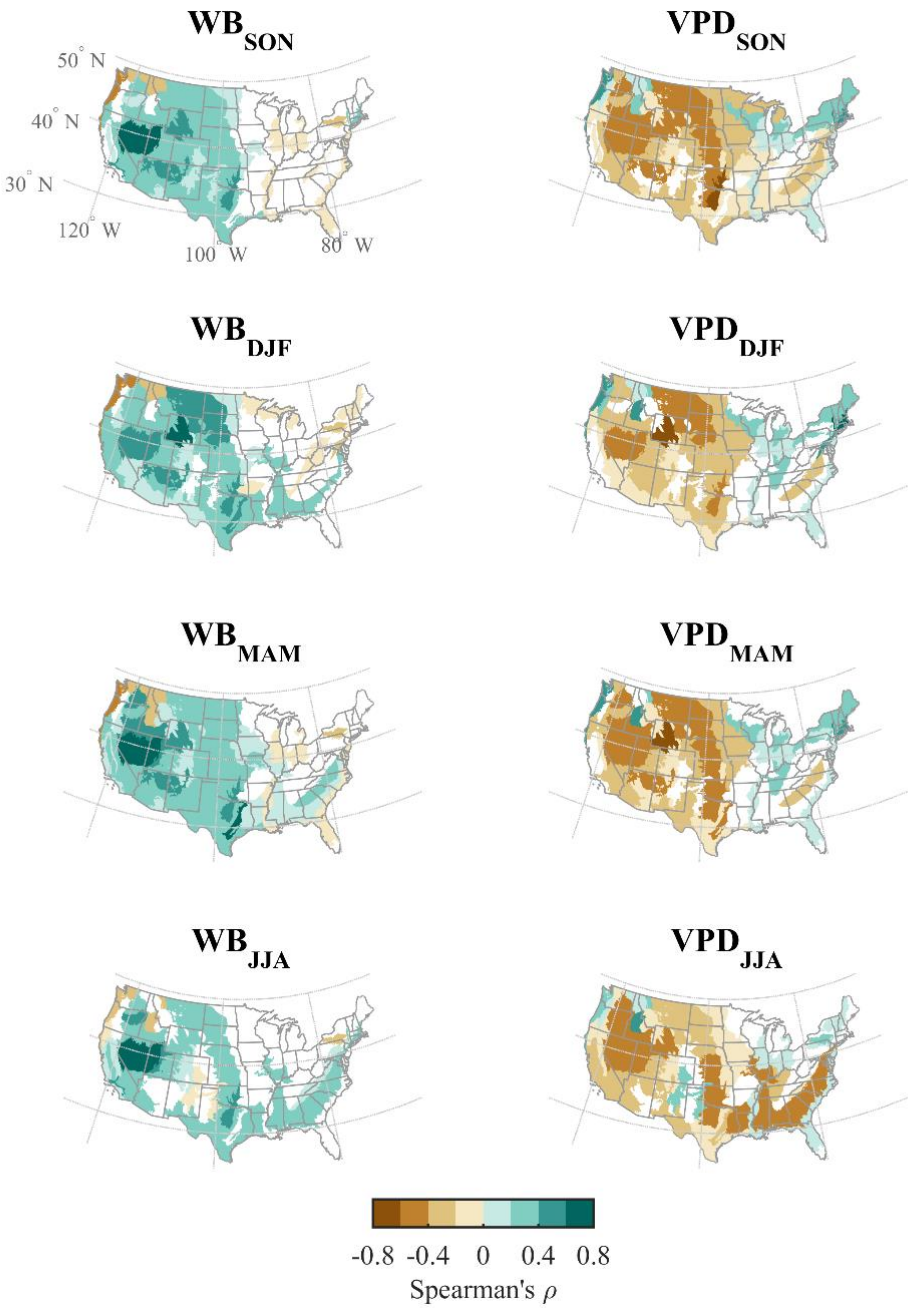


**Figure 3.5.** Spearman's rank correlation coefficient (ρ) between $S^*$ and seasonal vapor pressure deficit (VPD) and water balance (WB). Only ecoregions with significant correlations ($p<0.05$) are shown.

The ecoregion-level TSC models explain 50-95% of the $S^*$ variance in most of the U.S., with notably poorer performance in the Northern Cascades ecoregion and many ecoregions of the southern high plains and Appalachians (Figure 3.6 a-b; Table A5). By comparison, the model based on climate only (C) captures much less variance in $S^*$. The only

ecoregions in which the C models exhibit comparable skill to the TSC models are the driest regions of the western U.S. and parts of the southeastern U.S. Models that include either soil (SC) or topography (TC) in addition to climate perform comparably to the full TSC model (Table A5), in most cases explaining only 0-11% less variance that the full models.

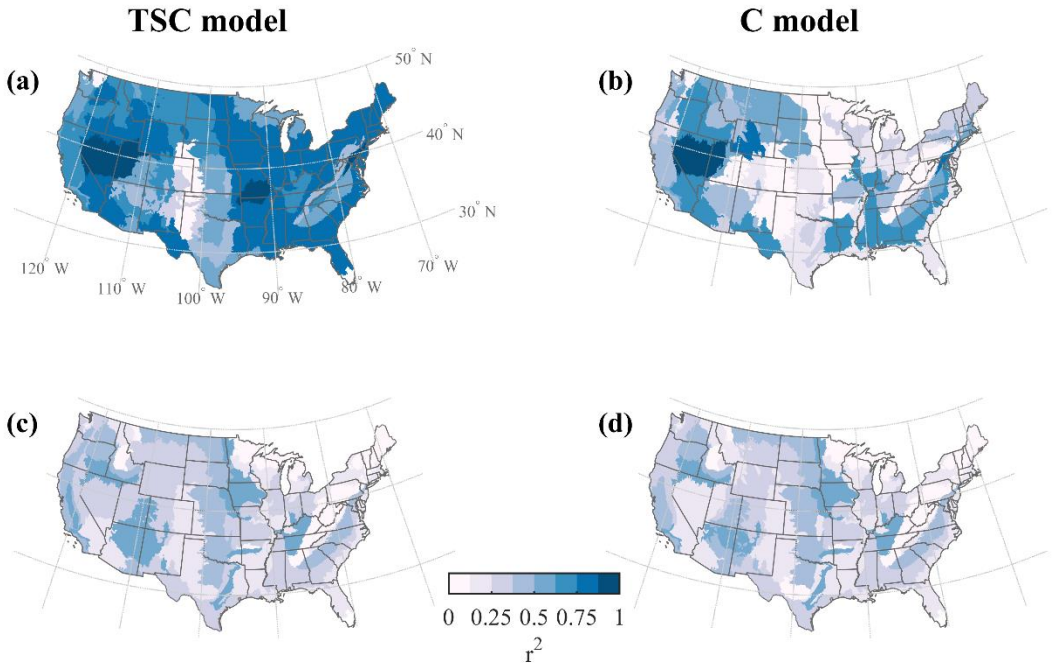


**Figure 3.6. Random forest model strength ($r^2$) for explaining variation in environmental stress.** Variance explained for $S^*$ with (a) the full TSC model and (b) the climate-only C model. Variance explained for $S_r$ with (c) the full TSC model and (d) the climate-only C model.

By comparison to the $S^*$ models, the ecoregion-level RF models of $S_r$ generally explain far less variance (Figure 3.6 c-d; Table A6). This can likely be explained by high within-ecoregion variability in mean $S^*$ among tree-ring sites, whereas this spatial variability is not represented by $S_r$, in which all sites have the same mean stress value. Given that all of the variance in $S_r$ is temporal (rather than spatial) in nature, the TC, SC, and TSC models do not perform substantially better than the C model.

**Discussion**

The global tree-ring network, which now contains ring-width measurements from more than 3,000 sites [*St. George*, 2014], represents a largely untapped yet promising resource for carbon cycle research [*Babst et al.*, 2014]. The tree-ring environmental stress index developed in this study, defined as the ratio of actual to optimal growth, has the potential to provide global coverage of a key component of primary production models that has historically been difficult to quantify and that contributes substantial error to carbon uptake estimates [*Song et al.*, 2013; *Cai et al.*, 2014; *Zhang et al.*, 2015]. This index depends on accurate estimation of optimal growth rate, which in turn requires accurate estimates of annual stem diameter and knowledge of basic species traits and growth forms. While ring-width based estimates of stem diameter are systematically underestimated, these errors get proportionally smaller as trees grow larger. Among the six intensively-sampled ponderosa pine sites, both $\Delta D_{opt}^{*}$ and $S^{*}$ are robust to bias in diameter estimates once trees attain DBH greater than 30 cm. Given that DBH is rarely measured or reported for most tree-ring sites, the fact that biased annual diameter estimates do not substantially contribute to error in this stress index is an encouraging sign for future applications.

The optimal growth model (Eqn. 1) requires five species-specific parameters that are difficult to obtain with equal reliability for all species [*Shugart*, 1984]. While DBH and height can be easily measured for individual trees, $D_{max}$ and $H_{max}$ for a given species cannot be directly observed but must be inferred based on available measurements of individuals. The remaining parameters ($G$, $b_2$, and $b_3$), which account for species-specific growth rates and tree forms, are estimated as functions of $D_{max}$, $H_{max}$, and the maximum age of the species. Any errors in $D_{max}$ and $H_{max}$ would therefore also propagate to the remaining parameters. Here, I attempted to minimize the uncertainty in these parameters by obtaining them predominantly from a single source [*Hardin et al.*, 2001], supplemented with

information from the forest gap model literature [*Shugart*, 1984; *Urban et al.*, 1993]. Future work could test the sensitivity of $\Delta D_{opt}^{*}$ and $S^{*}$ to these parameters or explore alternative methods of parameterization, such as empirical optimization approaches.

The tree-ring environmental stress index captured a significant amount of variance in continent-wide primary production. Even for distances up to 100 km between the tree-ring sites and flux towers, the correlation between $S^{*}$ and annual GPP remained positive and statistically significant at a 99% level. While there may be local factors that contribute to differences between the tree-ring sites and the flux tower sites, this result suggests that tree-ring data can provide valuable information on environmental stresses over large areas that could be assimilated into primary production models, including remotely sensed models based on the light-use efficiency paradigm.

While the global tree-ring database offers significant potential for informing carbon cycle models, including the environmental stress component of light-use efficiency models, there are several challenges and limitations of tree-ring data with respect to ecosystem carbon uptake that must be addressed and overcome. First, primary production of a given ecosystem results from growth of all individual plants, including both woody and herbaceous species, but tree ring networks only measure growth of a limited subset of woody plant species, usually long-lived and widespread species like pines, oaks, and firs. Any index of environmental stress based on tree-ring data must therefore assume that tree-ring chronologies developed from one woody plant species are reasonably representative of the environmental stresses experienced by all plants in the surrounding region. While this may not be strictly true, previous studies have shown that the normalized difference vegetation index over grasslands is significantly and positively correlated with nearby tree-ring width chronologies [*Liang et al.*, 2005, 2009], suggesting this may be a reasonable approximation. Likewise, ring width chronologies developed from a single tree species can capture

significant variance in normalized difference vegetation index over relatively large regions [*Beck et al.*, 2013; *Bunn et al.*, 2013], demonstrating that chronologies from one tree species may be reasonably representative of primary production over entire landscapes.

A second potential limitation is that the ITRDB contains sites with a wide range of sample designs, which differ by site and investigator but which are not typically reported in the site metadata. Since one of the primary applications of dendrochronology is for paleoclimate reconstructions, investigators often target old trees that are predominantly limited by climatic factors. The most common sample design therefore involves selecting large, dominant trees growing in physiographically-stressful landscape positions (e.g., steep, south-facing rocky slopes) and that show minimal signs of damage from lightning, fires, or forest pests and pathogens [*Cherubini et al.*, 1998; *Nehrbass-Ahles et al.*, 2014]. While other sample designs are also used [*Nehrbass-Ahles et al.*, 2014 and references therein], many of the sites in the ITRDB are likely biased towards old trees with relatively low growth rates that may not be representative of the entire stand or region. This is particularly problematic for studies using tree-ring data to directly calculate primary productivity or long-term growth trends [*Cherubini et al.*, 1998; *Brienen et al.*, 2012; *Bowman et al.*, 2013; *Nehrbass-Ahles et al.*, 2014], while inferences regarding the environmental drivers of growth are relatively robust to choice of sample design [*Nehrbass-Ahles et al.*, 2014]. Formally testing the impact of sample design on the tree-ring environmental stress index remains a priority for future research. Further work is also necessary to determine if species other than ponderosa pine are robust to uncertainties in ring-width based estimates of $D^*$.

Beyond the potential relevance of a tree-ring environmental stress index for potential assimilation into existing primary production models, my results illustrate two key findings regarding environmental stresses in the conterminous U.S. First, I demonstrate the importance of pre-growing season climate for forest growth and productivity. In particular,

ecosystems of the western U.S. rely on water that is delivered prior to the growing season, including during the previous growing season (which likely reflects carryover of carbohydrates from one year to the next [*Kagawa et al.*, 2006; *Offermann et al.*, 2011]) and during winter prior to the start of the growing season. In contrast, many primary production models assume instantaneous responses of stomata to current soil moisture or vapor pressure deficit but do not include physically-meaningful lags between the hydroclimatic system and ecosystem carbon uptake, except insofar as these lags are implicitly represented in the vegetation index used to estimate the fraction of photosynthetically active radiation absorbed by the canopy. In snow-dominated hydroclimates, such as the western U.S., incorporation of functions that capture lags between water delivery and carbon uptake could improve the representation of environmental stress in these models.

A second key finding is my demonstration of the importance of both topographic and edaphic conditions for determining spatial gradients in mean environmental stress. The model experiments show that climate gradients alone cannot capture spatial variation of environmental stress, except in ecoregions that are strongly limited by climate, such as the driest regions of the western U.S. Including either topographic or soil variables in addition to climate variables can substantially improve model performance. These variables are not typically included in the current generation of light-use efficiency models, partly due to challenges in accurately representing soil properties at a fine resolution on a continental scale. Updating the present generation of environmental stress models to include physically-meaningful lags between climate and ecosystem carbon uptake and to represent site factors that influence stress would therefore likely improve primary production estimates.

# CHAPTER 4: SHIFTING PACIFIC STORM TRACKS AS STRESSORS TO ECOSYSTEMS OF WESTERN NORTH AMERICA

## Introduction

In much of western North America (hereafter, "the West"), water is a scarce resource for both natural [Chapter 3; *Vicente-Serrano et al.*, 2013, 2014] and social [*Mekonnen and Hoekstra*, 2016] systems. In these dry regions, variation of precipitation and evaporative demand drive many ecosystem processes, including vegetation phenology [*Tang et al.*, 2015] and primary production [*Nemani et al.*, 2003; *Berner and Law*, 2015; *Barnes et al.*, 2016], as well as the size and severity of wildfires [*Littell et al.*, 2009; *Williams et al.*, 2015]. Overlain on the natural internal variability of the Western hydroclimate are anthropogenic perturbations to the climate system, which are likely to have significant impacts on the structure and function of terrestrial ecosystems, including on the ability of terrestrial vegetation to remain a large sink for anthropogenic $CO_2$ emissions [*Settele et al.*, 2014]. Beyond the direct effects of temperature on physiological processes and biochemical reactions of vegetation, higher temperatures have a nonlinear effect on vapor pressure deficit, leading to likely increases in drought frequency and severity due to increased evaporative demand as climate warming continues [*Cook et al.*, 2014]. Temperature increases have already had detectable impacts on wildfire [*Westerling et al.*, 2006; *Dennison et al.*, 2014] and vegetation phenology [*Zhang et al.*, 2007b; *Körner and Basler*, 2010], and further increases in evaporative demand are likely to have significant negative consequences for ecosystems of the West [*Williams et al.*, 2013; *Restaino et al.*, 2016].

While increases in temperature and evaporative demand are highly likely over the 21st century, changes in the supply-side of the water balance are far less certain and will depend on both global and regional factors [*Collins et al.*, 2013; *Kirtman et al.*, 2013]. In the West in particular, much of the annual precipitation arrives during the cool season via extratropical cyclones, which are preferentially generated and steered within westerly storm tracks [*Chang et al.*, 2002; *Shaw et al.*, 2016]. Midlatitude Pacific storm tracks are therefore one of the primary water delivery mechanisms to this region and an important feature of Western hydroclimate [*Wise*, 2010a]. The latitudinal positions, intensities, and trajectories of Pacific storm tracks vary on interannual [*Archer and Caldeira*, 2008] to millennial [*Oster et al.*, 2015] timescales, and this variation is largely responsible for hydroclimatic variability in the West.

The average latitudinal positions of Pacific storm tracks are expected to shift under a warming climate [*Yin*, 2005; *Salathé*, 2006; *Lorenz and DeWeaver*, 2007; *Shaw et al.*, 2016]. On average, climate models project midlatitude storm tracks to migrate towards the poles [*Kirtman et al.*, 2013; *Mbengue and Schneider*, 2013], though the direction and magnitude of future storm track shifts remain highly uncertain due to the competing influences of climate change on the diverse atmospheric processes that affect storm tracks [*Shaw et al.*, 2016]. Since storm tracks are such a critical component of water delivery to the West, any sustained shift in Pacific storm track position or intensity over the 21st century will likely alter the hydroclimate of the region. Given the importance of these storm tracks for water delivery to this region, where both social and natural systems are limited by water availability, it is critical to understand how shifting storm tracks have affected water resources and ecosystems in the recent past. In this chapter, I examine the sensitivity of both hydrological and ecological systems in the West (defined in this study as the region from 30°N to 70°N latitude and 100°W to 145°W longitude) to variation of the annual mean Pacific storm track

position and intensity during the October to March cool season. This research is driven by two main questions: 1) how have the hydroclimate and water resources of the West responded to historical Pacific storm track variability, and 2) how have storm track-induced changes in water supply affected primary production, phenology, and fire regimes in the West?

## Materials and Methods

*Estimation of the historical Pacific storm track*

I estimated the position of the historic annual cool-season Pacific storm track based on the maximum variance of daily mean October – March meridional wind velocity (*v*-wind) at 300 hPa, following application of a first-difference filter [*Quadrelli and Wallace*, 2002; *McAfee and Russell*, 2008; *Wise*, 2010a] (Figure 4.1). Using gridded *v*-wind from the North American Regional Reanalysis (NARR) for the period 1979-2014 [*Mesinger et al.*, 2006], I derived cool-season storm track estimates for the study period 1980-2014. Due to data availability for other climate and ecological datasets used in this study, not all subsequent analyses cover this full study period. The *v*-wind variance was resampled from the native 32 km horizontal resolution to a 0.5 degree grid using a nearest neighbor resampling method, from which I obtained the latitude of maximum cool-season *v*-wind variance and smoothed the resulting storm track using a robust loess curve 10% the length of the domain to reduce noise (Figure 4.1). For subsequent analyses, I defined cool-season Pacific storm track position as the mean latitude of maximum *v*-wind variance in the region from 130°W to 115°W (Figure 4.1). I also obtained a 2°×2° gridded cool-season (Oct-Mar) 500 hPa geopotential height climatology for the period 1981-2010 from the 20$^{th}$ Century Reanalysis project [*Compo et al.*, 2011] for visual comparison to the estimated storm track trajectories.

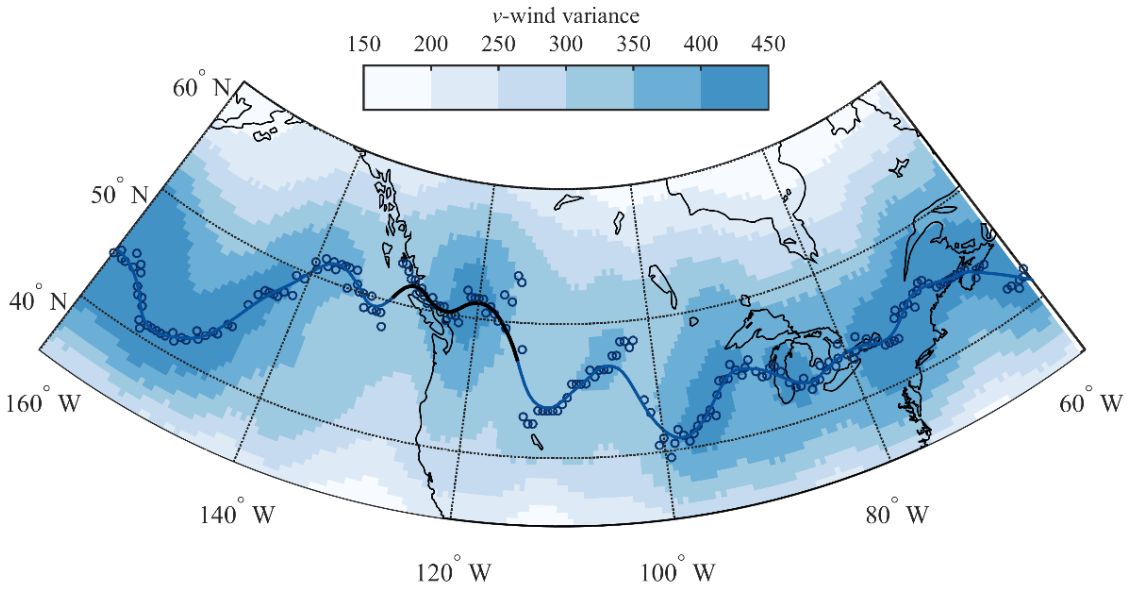


**Figure 4.1.** Delineation of the cool-season storm track in an example year (1988). The storm track was estimated as the latitude of maximum cool-season (October – March) 300 hPa meridional wind variance (blue circles), smoothed with a robust loess filter (blue line). Storm track position over western North America was defined as the mean latitude of the smoothed storm track between 130°W and 115°W (highlighted in black).

In addition to the seasonal analysis of storm track position, I also conducted analyses on monthly storm track position and on cool-season storm track intensity. First, using the methods described above, I estimated the mean storm track position for each individual month within the cool season (October through March) and examined how sub-seasonal storm track variability affects water delivery to the West. Second, following *Chang and Fu* [2002], I estimated annual mean cool-season storm track intensity as the mean maximum cool-season *v*-wind variance in the region from 130°W to 115°W.

*Hydrological variables and analyses*

For assessing impacts of storm track position on moisture supply, I obtained the 0.5°×0.5° gridded cool-season (October – March) Standardized Precipitation-Evapotranspiration Index (SPEI) for the period 1980-2013 [*Vicente-Serrano et al.*, 2010a, 2010b], which accounts for both the supply (precipitation) and demand (potential

evapotranspiration) aspects of the water balance. For comparison, I also calculated the Standardized Precipitation Index (SPI) [*McKee et al.*, 1993], which only includes the supply side of the water balance, from 0.5°×0.5° gridded Climate Research Unit TS3.22 monthly precipitation [*Harris et al.*, 2014]. I assessed the impacts of shifting Pacific storm tracks on these hydrological variables using the Pearson correlation coefficient.

I obtained 1 April SWE records for the period 1980-2013 from the Snow Telemetry (SNOTEL) and Snow Course networks through the USDA Natural Resources Conservation Service National Water and Climate Center. The SNOTEL network provides automated, daily measurements of SWE by converting the weight of snowpack on snow pillows to its equivalent depth in liquid form. Snow Course data is recorded manually once per month, but it is typically measured on or near the first of the month [*USDA Natural Resources Conservation Service*, 2016]. Only SNOTEL and Snow Course sites with at least 20 years of non-zero April SWE measurements were used for subsequent analyses. I also obtained water year (October – September) mean daily streamflow from the USDA National Water and Climate Center for all U.S. Geological Survey stream gauges that fall within the study area and that include at least 20 years of measurements between 1980-2013.

*Ecological variables and analyses*

I assessed the impacts of shifting Pacific storm track positions on ecosystem processes in the West using remotely sensed estimates of land surface phenology and wildfire area, as well as tree-ring widths as a proxy for forest growth and net primary production. I derived land surface phenology estimates from the fortnightly, 8 km resolution 3$^{rd}$ generation Global Inventory Modeling and Mapping Studies (GIMMS) normalized difference vegetation index (NDVI) for the period 1982-2012 [*Pinzon and Tucker*, 2014]. The NDVI, which is based on the difference between near infrared and red reflectance from the land surface, is sensitive to

vegetation health, abundance, and photosynthetic capacity. I removed poor quality observations (based on quality flags provided with the GIMMS data) and spatially aggregated the 8 km NDVI to the level of whole ecoregions by taking the mean value within each of the Environmental Protection Agency's Level III ecoregions (Figure 4.2) [*Omernik*, 1987]. This spatial aggregation was performed in order to minimize the effect of noise in the pixel-level NDVI time series, to reduce computation time, and to simplify the presentation and interpretation of results [e.g., *White et al.*, 2009].

To reduce noise in the ecoregion-level NDVI time-series, I applied outlier and modified best index slope extraction filters [*Hwang et al.*, 2011a, 2011b; *Dannenberg et al.*, 2015], discarded any ecoregion-level NDVI time-series without significant power at annual frequencies using a wavelet filter [*Torrence and Compo*, 1998], and smoothed the annual NDVI time-series using a difference logistic function [*Fisher et al.*, 2006; *Hwang et al.*, 2011a, 2011b; *Dannenberg et al.*, 2015]:

$$\hat{y}(t) = c \times \left(\frac{1}{1+e^{a+bt}} - \frac{1}{1+e^{a'+b't}}\right) + d, \quad (1)$$

Where $\hat{y}(t)$ is the smoothed NDVI for time *t*, *a* and *b* (*a'* and *b'*) are fitting parameters for the leaf onset (leaf senescence) phases of the growing season, *c* is the amplitude of the annual smoothed NDVI time-series, and *d* is the annual minimum of the smoothed NDVI time-series (Figure 4.2, Figure 4.3). The start and end of the "green season" were defined as the day of year when the annual smoothed NDVI crossed a local half-amplitude threshold during the leaf onset and leaf senescence phases of the growing season, respectively, while the total length of the green season was defined as the difference (in days) between the start and end of the green season (Figure 4.3). Annual peak NDVI ($NDVI_{max}$) was defined as the maximum of the smoothed NDVI time-series for each year (Figure 4.3).

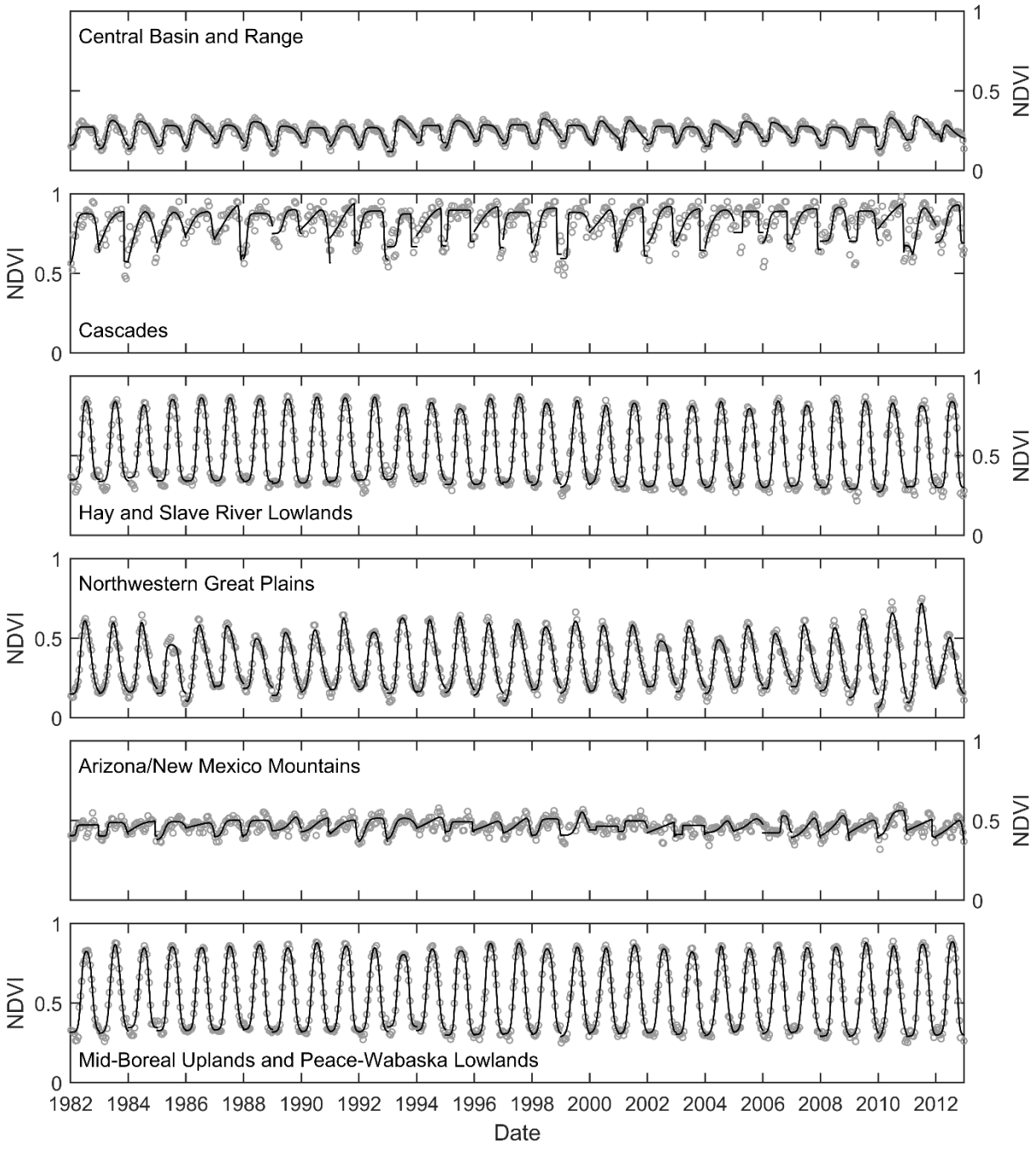


**Figure 4.2.** Raw and smoothed NDVI time series for six example Level III EPA ecoregions. Fortnightly, ecoregion-aggregated 3rd generation Global Inventory Modeling and Mapping Studies normalized difference vegetation index (NDVI; gray circles), with annual difference logistic curves (black lines) for 1982-2012.

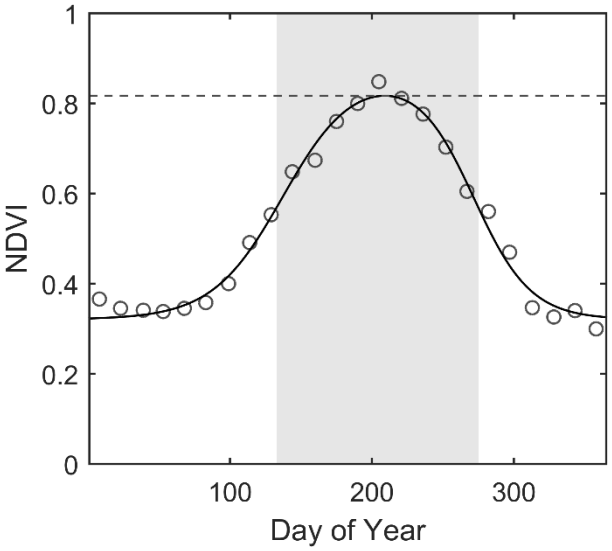


**Figure 4.3.** Calculation of land surface phenology metrics. Annual, ecoregion-aggregated NDVI (circles) was smoothed and interpolated from fortnightly to daily temporal resolution using a difference logistic function (black line). The start and end of the "green season" (shown as a gray box) were defined as the points where the smoothed NDVI crossed the half-amplitude threshold of the smoothed NDVI in the green-up and senescence phases of the growing season, respectively. The length of the green season was defined as the number of days from the start to the end of the green season. Peak NDVI (dashed line) was defined as the maximum of the difference logistic function.

I calculated phenology anomalies for each ecoregion during years with extreme northerly storm tracks (upper latitude quartile) and extreme southerly storm tracks (lower latitude quartile), as well as during years with extremely strong storm tracks (upper intensity quartile) and extremely weak storm tracks (lower intensity quartile). I assessed statistical significance of these anomalies using a permutation resampling method [*Wise*, 2010b], in which the mean and variance of the observed phenology within each ecoregion was used to randomly generate 10,000 possible realizations for each of the extreme storm track quartiles. I consider observed anomalies statistically significant if they exceed the magnitude of the 5$^{th}$ or 95$^{th}$ percentile of the randomly permuted anomalies.

To assess the sensitivity of forest growth to Pacific storm track position and intensity, I obtained tree-ring widths from 431 sites across the West from the International Tree-Ring Data Bank [*Grissino-Mayer and Fritts*, 1997], plus seven additional ponderosa pine

chronologies from Washington State (see Chapter 2). Each site included measurements for at least the 20-year period from 1980-1999. I detrended each ring width series in the dplR program [*Bunn*, 2008] using a cubic smoothing spline two-thirds the length of the total series with a 50% frequency response [*Cook and Peters*, 1981]. Detrended ring widths were averaged using Tukey's biweight robust mean to obtain site-level growth indices, and the relationship between these indices and Pacific storm track position and intensity was assessed using Pearson's correlation coefficient. Since I conducted a large number of local significance tests ($n$ = 438), there is a high probability of type I errors (i.e., false positive tests). I therefore compared the observed p-value distribution to the uniform distribution that would be expected if the null hypothesis were true for all sites and conducted a "field significance" test that accounts for the false discovery rate [*Wilks*, 2006]. I also assessed the overall response of western U.S. forest growth to storm track variability using an unweighted mean of all U.S. tree-ring chronologies located west of 100°W, after first normalizing each tree-ring series to a mean of zero and unit variance.

Fire is a natural feature of ecosystems in the West, particularly in the dry forests and shrublands of the western U.S. While many factors play a role in the ignition and spread of fire, including antecedent climate, fuel abundance, ignition sources, topographic relief, and land management [*Bowman et al.*, 2009; *Littell et al.*, 2009], moisture balance is particularly important for determining the spread and intensity of fire [*Williams et al.*, 2015]. I assessed the role of cool-season storm tracks on Western wildfire using annual burn area estimates from the U.S. Forest Service Monitoring Trends in Burn Severity program, which maps fire boundaries and burn severities for the conterminous U.S. based on near and middle infrared reflectance from Landsat imagery [*Eidenshink et al.*, 2007]. I focused on the northwestern U.S. (defined here as the region from 41°N to 49°N and west of 100°W) due to its hydrological responsiveness to cool-season storm tracks (see Results) and the prevalence of

fires throughout the region. After excluding all prescribed fires and any fires mapped with low confidence [*Dennison et al.*, 2014], I derived the annual area burned by moderate and high severity wildfires and the annual average moderate and high severity burn area per fire. I assessed the relationship between storm track position and wildfire using the Theil-Sen slope estimate [*Wilcox*, 2005; *Dennison et al.*, 2014], a nonparametric regression technique that is robust to outliers. I contextualized the observed response of the burn area to storm track variability by randomly permuting the wildfire time series 10,000 times, recalculating the Theil-Sen slope for each permuted time series, and comparing the observed slope to the distribution of slopes from the 10,000 random realizations [*Dennison et al.*, 2014].

## Results

### *Historical variation of cool-season Pacific storm tracks*

From 1980-2014, cool-season Pacific storm tracks entered western North America between approximately 41°N to 53°N (Figure 4.4), with the median storm track positioned at 45.3°N. The distribution of storm track positions during this period approximates a normal distribution (Lilliefors test of normality; $P = 0.09$) with a small, but not statistically significant ($P = 0.31$), increase in storm track position of +0.05°N $yr^{-1}$ over the study period. However, the time period examined in this study is relatively short due to the temporal limitations of the NARR dataset. While this dataset is suitable for examining recent storm track variability, any robust assessment of long-term storm track trends would require a longer dataset.

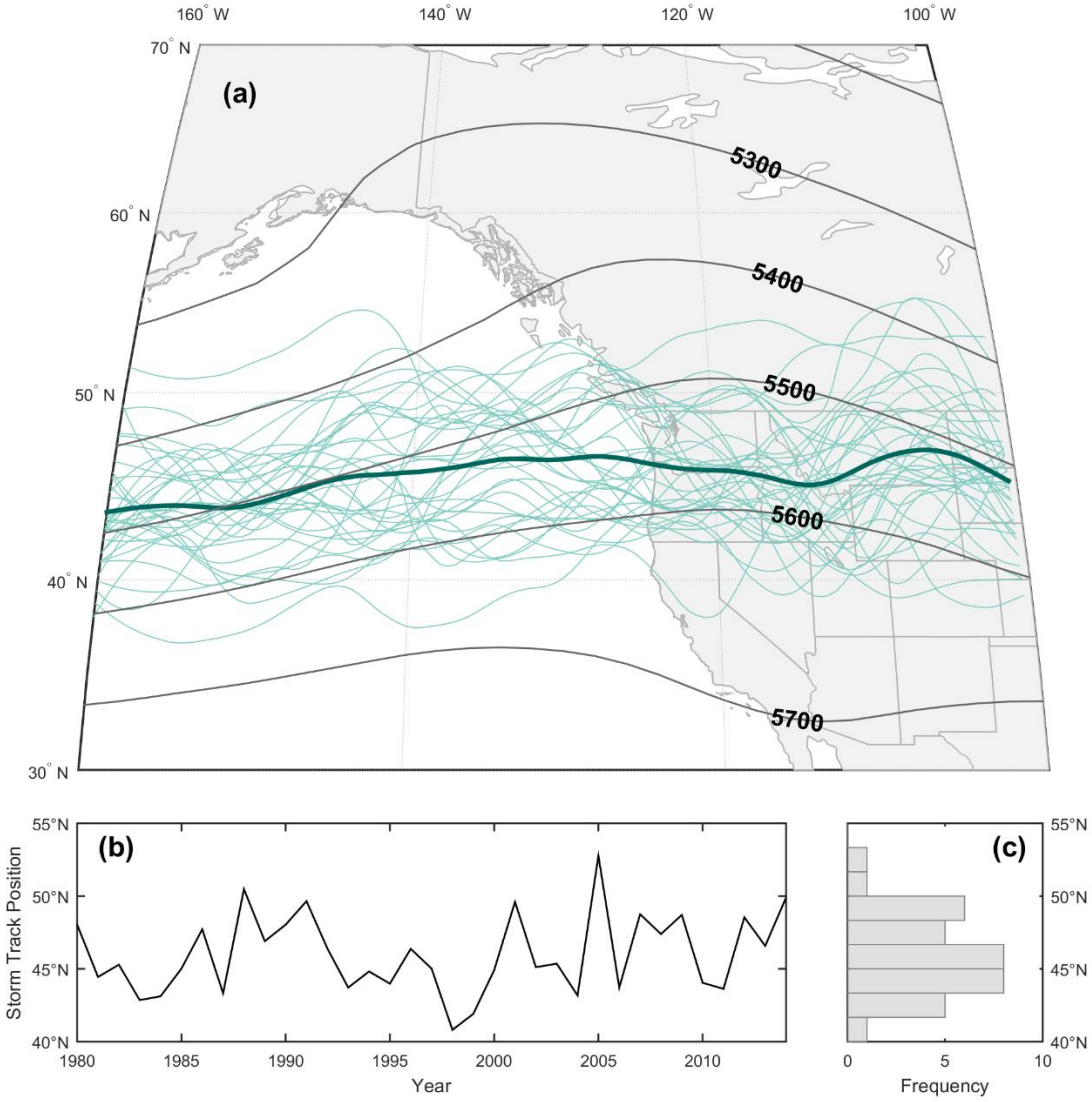


**Figure 4.4.** Storm track trajectories from 1980-2014. (a) Annual cool-season storm track trajectories, based on 300 hPa meridional wind variance from the North American Regional Reanalysis, are shown as light green lines, with the mean storm track shown in dark green. The 1981-2010, 500 hPa geopotential height climatology (in meters) from the 20th Century Reanalysis is shown as dark gray contours. (b) Time series and (c) histogram of mean cool-season Pacific storm track position for the region 130°W to 115°W.

*Hydrological responses to shifting Pacific storm tracks*

Cool-season moisture supply in the West exhibits opposite responses to variation in the latitudinal position of the Pacific storm track on either side of the 50°N parallel (Figure 4.5a). North of 50°N, the SPEI tends to be positively correlated with storm track latitude (except in the eastern Northwest Territories and western Nunavut territory), with a

particularly strong response throughout the Yukon Territory and northwestern British Columbia as well as in northeastern Alberta. However, in the northwestern U.S., the SPEI is negatively correlated with storm track latitude, particularly in the states of Washington, Oregon, Idaho, and northern California but also in eastern Montana, Wyoming, and the Dakotas. Correlations between storm track position and the SPEI in the southwestern U.S. are generally positive but not statistically significant. North-shifted storm tracks therefore result in greater water delivery to western Canada, but reduced moisture supply throughout the northwestern U.S.

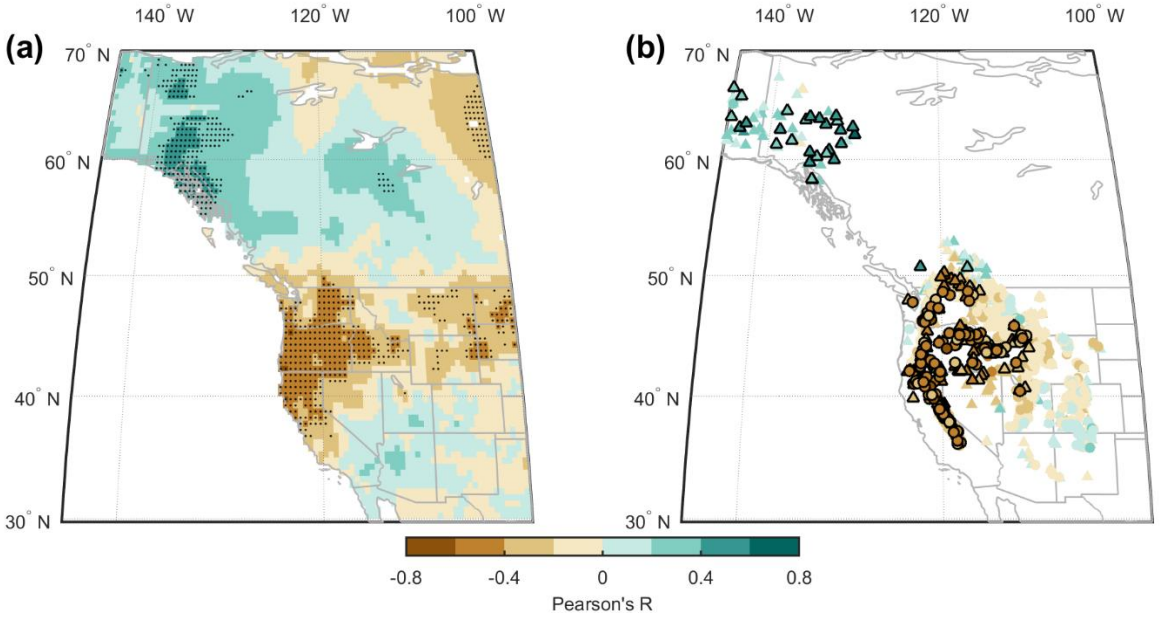


**Figure 4.5.** Relationship between Pacific storm track position and drought and snow pack**.** Pearson's correlation coefficient, R, between cool-season storm track position and (a) the October-March standardized precipitation-evapotranspiration index (SPEI) and (b) April snow water equivalent (SWE). SPEI Grid cells with significant correlations ($P < 0.05$) to cool-season storm track position are shown with black dots. SWE stations with significant correlations to cool-season storm track position are highlighted with black edges. SNOTEL sites are shown as circles, and Snow Course sites are shown as triangles.

The association between cool-season Pacific storm track position and the SPEI is driven almost entirely by the precipitation side of the water balance, as demonstrated by the nearly identical correlation patterns of the SPEI (Figure 4.5a) and the SPI (Figure A17) to storm track position. Additionally, visual assessment of correlation patterns between the SPEI

and monthly storm track positions suggest that cool-season moisture supply in the West is more responsive to storm track position in late autumn (October and November) and early spring (March) than in midwinter months (Figure A18), though January storm tracks are negatively correlated with the SPEI throughout much of the northwestern U.S. This finding is consistent with observations that eddy amplitude of the Pacific storm track exhibits a midwinter minimum [*Nakamura*, 1992; *Chang et al.*, 2002; *Chang*, 2003; *Penny et al.*, 2013].

The increased water delivery to northwestern Canada and reduced water delivery to the northwestern U.S. associated with poleward shifts of cool-season storm tracks translate to significant spring snowpack anomalies throughout montane regions of western North America (Figure 4.5b). In the mountains of the Yukon Territories and northwestern British Columbia, April SWE is positively correlated with storm track latitude, reflecting greater cool-season water delivery to this region when the storm track is displaced poleward. By contrast, April SWE is negatively correlated with storm track latitude throughout many of the mountain ranges of the western U.S., including the Sierra Nevadas, the Cascades, and parts of the central Rockies. Even more than the SPEI, the April SWE correlation patterns are largely driven by storm track position during the shoulder months of October, November, and March (Figure A19), though correlations between April SWE and February storm track actually exhibit opposite patterns from the overall cool-season response (i.e., positive correlations between February storm track position and April SWE in the northwestern U.S.; Figure A19e). Water resources in the western U.S. are dependent on mountain snowpack as a natural reservoir that is gradually released during spring and summer [*Stewart et al.,* 2005]. Given that streamflow in this region is largely generated from snowmelt [*Pederson et al.*, 2011; *Littell et al.*, 2016], water year streamflow is also negatively correlated with Pacific storm track position throughout the northwestern U.S., particularly in the states of Oregon, southern Idaho, and northern California (Figure A20).

Correlations between water variables and cool-season Pacific storm track intensity exhibit very different spatial patterns than they did with storm track position (Figure A21). While the moisture supply of the U.S. Southwest was not strongly correlated to Pacific storm track position, it is negatively and significantly correlated with Pacific storm track intensity (Figure A21a). North of the 40°N parallel, very few SPEI grid cells are significantly correlated with storm track intensity, with the exception of small regions of western Washington, Vancouver Island, and southeastern Alaska (Figure A21a). This suggests that while the cool-season hydroclimate of the Pacific Northwest is largely responsive to storm track *position*, the Southwest is most responsive to storm track *intensity*. However, April SWE is positively and significantly correlated with storm track intensity throughout the U.S. Pacific Northwest (Figure A21b). Since the overall precipitation response to storm track intensity is relatively small in this region (Figure A21a), there may be an interaction between storm track intensity and cool-season temperature that affects how much cool-season precipitation is delivered as snow and how much remains in the snowpack in April.

*Ecosystem responses to shifting Pacific storm tracks*

The response of land surface $NDVI_{max}$ to cool-season Pacific storm track position follows similar spatial patterns as the SPEI. When the storm track is positioned anomalously to the north, western Canadian ecosystems tend to be greener than average, significantly so in several ecoregions (the North Cascades, Canadian Rockies, Mid-Boreal Uplands and Peace-Wabaska Lowlands, and Coppermine River and Tazin Lake Uplands), while ecosystems of the western U.S. tend to be browner than average (Figure 4.6a). When the storm track is positioned abnormally far south, however, $NDVI_{max}$ is browner than average throughout most of western Canada and significantly greener than average in much of the western U.S. (Figure 4.6b), likely due to increases in vegetation health and abundance following increased cool-

season water delivery to this region. Other land surface phenology metrics besides peak greenness show weak or inconsistent relationships to storm track position, including start (Figure A22), end (Figure A23), and total length (Figure A24) of the "green season." Generally speaking, $NDVI_{max}$ in the West is less sensitive to storm track intensity than it is to storm track position (Figure A25). In particular, relatively few ecoregions exhibit significant $NDVI_{max}$ anomalies when storm track intensity is stronger than normal (Figure A25a). However, several ecoregions of western Canada and the Cascades do tend to be significantly browner than average when storm track intensity is anomalously low (Figure A25b).

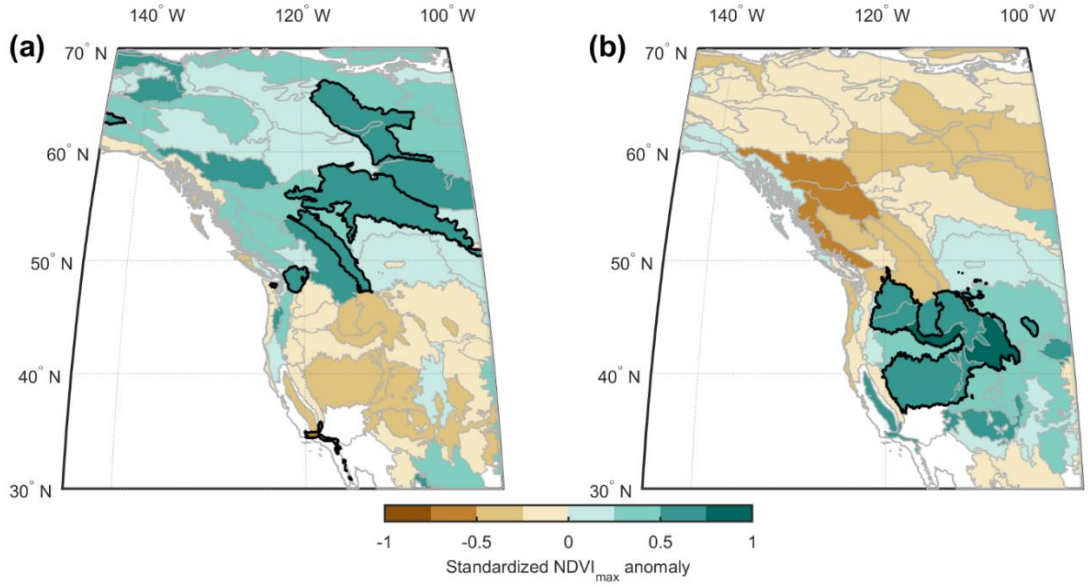


**Figure 4.6.** Relationship between Pacific storm track position and $NDVI_{max}$**.** Standardized $NDVI_{max}$ anomalies in years between 1982-2012 with storm track positions in (a) the northernmost 25$^{th}$ percentile and (b) the southernmost 25$^{th}$ percentile. Ecoregions with significant anomalies are outlined in black.

Forest growth in the dry regions of the western U.S. is largely dependent on water availability [*Nemani et al.*, 2003; *Boisvenue and Running*, 2006], including precipitation stored as snowpack during the cool-season [*St. George and Ault*, 2014]. Though other environmental factors affect growth, particularly evaporative demand during summer months [*Williams et al.*, 2013; *Restaino et al.*, 2016], most tree-ring widths in the West are negatively correlated with cool-season storm track position (Figure 4.7a), particularly for sites located

south of 49°N that receive less precipitation when the storm track is displaced north (Figure 4.7b). While some tree-ring series would be expected to exhibit significant correlations to storm track position due to type I errors associated with conducting a large number of hypothesis tests, the distribution of *P*-values from the local tests is smaller than expected if the null hypothesis were true for all sites (Figure 4.7c). A field significance test that accounts for the false discovery rate [*Wilks*, 2006] also suggests that there is a significant influence of cool-season storm track position on forest growth in the western U.S. ($P < 0.1$). A simple composite index of all tree-ring widths in the western U.S. further shows that forests in this region experience greater stress in years with north-shifted storm tracks (Pearson's R = −0.35; $P = 0.04$; Figure 4.7d). By contrast, the relationship between tree-ring width and storm track intensity is relatively weak throughout the West and is not statistically significant in either the field significance test nor in the composite index (Figure A26).

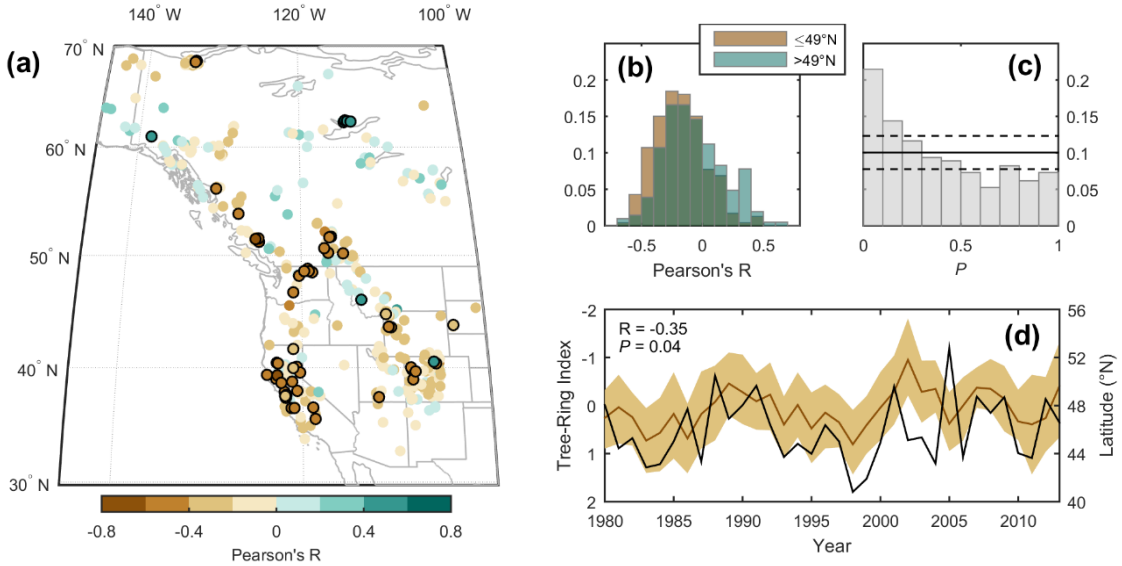


**Figure 4.7.** Relationship between Pacific storm track position and forest growth. (a) Pearson's correlation coefficient, R, between tree-ring widths and cool-season Pacific storm track position. Significant correlations ($P < 0.05$) are highlighted with black edges. (b) Distribution of R-values for tree-ring sites south of 49°N (brown bars) and north of 49°N (green bars). (c) Distribution of *P*-values from local significance tests (gray bars; n=438). The expected number of sites with *P*-values falling within each 0.1 increment range is shown as a black line, with dashed lines showing the 5$^{th}$ and 95$^{th}$ percentiles based on the binomial distribution. (d) Correlation between storm track position (black line) and a mean growth index for all sites south of 49°N (dark brown line), with the 20$^{th}$ to 80$^{th}$ percentile range shown in light brown. Note that the left y-axis is inverted.

Moisture delivery via cool-season Pacific storm tracks likely plays a role in the size and severity of wildfires in the northwestern U.S. (Figure 4.8), a region characterized by relatively frequent and extensive wildfire and by a negative hydrological response to north-shifted storm tracks (Figure 4.5, Figures A17-A20). During the period 1984-2014, an average of more than 2,600 $km^2$ per year of the northwestern U.S. was burned by moderate to high severity wildfire following extreme north-shifted cool-season storm tracks (Figure 4.8a). By contrast, in years with extreme southerly storm tracks, only an average of about 1,100 $km^2$ per year was burned by moderate to high severity wildfire. The total area burned by moderate and high severity fires in the northwestern U.S. increased by approximately 80 $km^2$ for every 1° poleward shift of the storm track (Figure 4.8b). Likewise, the average size of each fire increased by about 0.6 $km^2$ per 1° poleward shift of the cool-season Pacific storm track (Figure 4.8d). Random permutations of the fire time series show that for total moderate to high severity burn area, only 21% of the randomly permuted slopes are more extreme than the observed slope (Figure 4.8c), while only 7% of the randomly permuted slopes are more extreme than the observed slope for the moderate and high severity burn area per fire (Figure 4.8e).

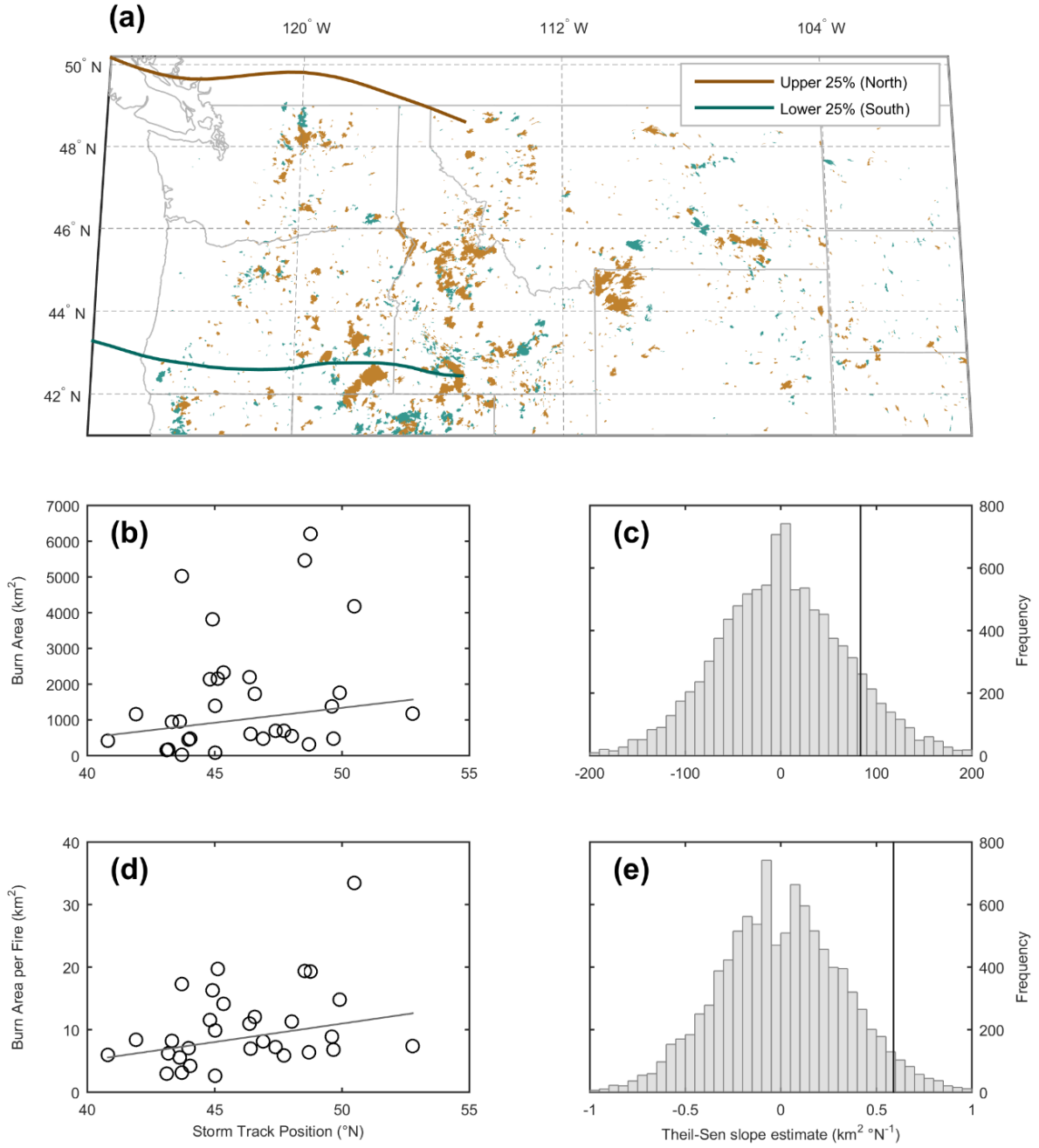


**Figure 4.8.** Relationship between Pacific storm track position and fire area. (a) Fire extents during years between 1984-2014 with storm track positions in the northernmost 25$^{th}$ percentile (brown) and the southernmost 25$^{th}$ percentile (green). The mean storm tracks during these extremes are shown as brown and green lines. Scatterplots of cool-season Pacific storm track position versus total annual moderate and high severity burn area (b) and average moderate and high severity burn area per fire (d), with the Theil-Sen regression line. Distribution of Theil-Sen slopes from 10,000 random permutations of the total annual moderate and high severity burn area time series (c) and the average moderate and high severity burn area per fire time series (e), with observed slopes shown as vertical lines.

## Discussion

Over the next century, changes on both the supply and demand sides of the water balance are likely to occur. While there are relatively large intermodel disagreements on the direction and magnitude of 21st century precipitation change [*Collins et al.*, 2013], increased temperatures and vapor pressure deficits (VPD) are robust features of climate model projections [*Williams et al*., 2013; *Cook et al.,* 2014]. Increased temperatures are likely to reduce snowpack and lead to a more rain-dominated hydroclimate in the West [*Barnett et al.*, 2008]. Evaporative demand is also expected to increase in response to higher temperatures and VPD, leading to more frequent and severe droughts even in the absence of changes in the supply side of the water balance [*Cook et al.*, 2014]. The expected increases in the demand side of the water balance over the 21st century will likely pose significant threats to the ecosystems of the West, since forest growth responds negatively to increases in VPD [*Williams et al.*, 2013; *Restaino et al.*, 2016] while wildfire size and severity respond positively to increases in VPD [*Williams et al.*, 2015].

Given the expected warming-induced increases in evaporative demand, it is crucial to better understand the drivers of moisture supply into the West and to characterize ecosystem responses to hydroclimatic change. Persistent changes in the position of cool-season Pacific storm tracks have the potential either to amplify or alleviate the hydrological and ecological consequences of increased evaporative demand, depending on the direction and magnitude of the shift. My results demonstrate the high sensitivity of water resources and ecosystem processes in the West to shifting Pacific storm tracks in the historical record. Cool-season water supply and snowpack both responded positively to north-shifted storm tracks throughout eastern Alaska and western Canada but negatively in the northwestern U.S. These hydroclimatic responses to storm track variability also translated to significant impacts on ecosystem processes, with enhanced greenness of Canadian ecosystems following

anomalously north-shifted storm tracks, but enhanced greenness in the western U.S. following anomalously south-shifted storm tracks. Reductions in water supply during years with north-shifted storm tracks negatively affected the ecosystems of the western U.S., which experience reduced forest growth and increased risk of moderate to high severity wildfires.

Based on these results, a persistent shift of cool-season storm tracks would likely have strong impacts on hydrological and ecological processes in the West. In general, midlatitude storm tracks are projected to shift towards the poles [*Kirtman et al.*, 2013; *Mbengue and Schneider*, 2013], though the exact direction and magnitude of this shift remain uncertain due to the "opposing influences" of climate change on the position of westerly storm tracks [*Shaw et al.*, 2016]. If the mean position of Pacific storm tracks does indeed shift northward, my results suggest that this would likely result in greater water delivery during the cool season in much of Canada and Alaska. On the other hand, in the western U.S., where human and natural systems depend on limited water resources, these results show that a persistent poleward shift of cool-season Pacific storm tracks would likely reduce cool-season moisture delivery. This could further exacerbate the water deficit expected due to increases in evaporative demand and pose additional stresses on the hydrology and ecology of this region, including decreases in ecosystem productivity and increases in wildfire area resulting from lower fuel moisture following dry winters.

# CHAPTER 5: SUMMARY AND CONCLUSIONS

Vegetation provides many of the key resources on which humanity depends, including mitigation of climate change through uptake of anthropogenic $CO_2$ emissions. The vegetation processes that provide these resources—including plant primary production and phenology—can be limited by unfavorable environmental conditions, such as non-optimal climate conditions and topographic and soil characteristics that limit the ability of plants to obtain belowground resources. In this dissertation, I used tree rings and remote sensing to examine how these environmental limitations to plant growth vary spatially and temporally in North American ecosystems.

In chapter 2, I examined how the seasonality of temperature and precipitation affect the growth of ponderosa pine using sub-annual tree-ring metrics from a small network of sites in the U.S. Pacific Northwest. In chapter 3, I developed a new "environmental stress" index from tree-ring data and used this index to model how unfavorable climatic, topographic, and edaphic conditions affect tree growth across the conterminous U.S., particularly within the context of improving the way that environmental stresses are represented in remotely sensed light-use efficiency models. Finally, in chapter 4, I used historical climate data, tree rings, and remote sensing to examine how variability of the Pacific storm track, an important atmospheric circulation feature, affects hydrological and ecological systems in western North America.

The findings from this research regarding environmental limitations to vegetation activity make three primary contributions within the fields of physical geography and biogeoscience:

**(1) Improving tree-ring-based reconstructions of past climate.** Tree rings are effective proxies for past climate only when they are limited by their local environment. In other words, dendroclimatic reconstructions are only possible for climatic variables that are actually limiting to growth. In chapter 2 of this dissertation, I examined the seasonality of climatic limitations to tree growth in the U.S. Pacific Northwest, which contributes towards ongoing efforts to improve tree-ring reconstructions of past precipitation and drought, many of which contain significant seasonal biases [*St. George et al.*, 2010; *Steinman et al.*, 2012]. For example, in the Pacific Northwest, tree-ring widths tend to be most sensitive to summer precipitation, resulting in drought reconstructions that underrepresent the contribution of cool-season precipitation to the overall water balance of the region [*Steinman et al.*, 2012]. In this research, I showed that the seasonal precipitation signals embedded in ponderosa pine tree rings vary substantially among different sites and tree-ring metrics. It is therefore possible to develop seasonally-resolved precipitation and drought reconstructions through careful site selection procedures and by measuring sub-annual ring widths in addition to the traditional total ring width.

**(2) Improving the representation of "environmental stress" in remotely sensed primary production models.** My dissertation research also lays a framework for improving the way that "environmental stress" is represented in remotely sensed light-use efficiency models of primary production. At present, these models typically assume instantaneous responses of plants to simple meteorological variables like temperature and vapor pressure deficit. However, many studies have shown that these environmental stress functions struggle to simulate water stress [e.g., *Zhang et al.*, 2015], leading to significant error in primary production estimates [*Cai et al.*, 2014]. In chapter 3, I demonstrated that tree growth throughout much of the western U.S. depends on water delivery across multiple seasons and that topographic and soil characteristics are significant spatial constraints on ecosystem

productivity. Accounting for these climate lags and for land surface characteristics in light-use efficiency models may improve primary production estimates. In particular, directly combining information from tree rings (e.g., the tree-ring "environmental stress" index developed in chapter 3) with remotely sensed imagery could represent a promising approach for improving the way that environmental limitations to growth are represented in these models.

**(3) Understanding impacts of climate change on terrestrial ecosystems.** This dissertation offers new insights into how vegetated ecosystems of North America will respond to a changing climate, particularly regarding three likely outcomes of future warming: (1) changes in the phase and seasonality of precipitation, (2) long-term shifts of synoptic-scale circulation features like midlatitude storm tracks, and (3) increases in VPD and evaporative demand due to higher temperatures. I demonstrated that vegetation activity in North America, particularly in the drier western regions, are quite sensitive to precipitation delivered during the cool season. Likely shifts from snow to rain [*Kapnick and Hall*, 2012; *Pierce and Cayan*, 2013] and changes in the seasonality and variability of precipitation [*Mote and Salathé*, 2010; *Rupp et al.*, 2016] could therefore pose significant threats to many of the ecosystems that rely on snowpack as a source of water availability. Furthermore, much of this water is delivered to North America via Pacific storm tracks. Current climate model projections suggest that these storm tracks will likely migrate towards the poles during the 21$^{st}$ century [*Mbengue and Schneider*, 2013], though there is still considerable uncertainty surrounding the exact direction and magnitude of this shift [*Shaw et al.*, 2016]. In chapter 4, I demonstrated that the latitudinal position of these storm tracks is an important driver of hydrological and ecological systems throughout much of western North America. Given the sensitivity of these systems to storm track position, any long-term shift of the storm track will likely have substantial consequences for both water resources and ecosystem services

throughout the region. Finally, on the other side of the water balance, I showed in chapter 3 that tree growth throughout the United States is negatively correlated with the vapor pressure deficit of the atmosphere. Since saturation vapor pressure is an exponential function of temperature [*Campbell and Norman*, 1998], higher temperatures will likely lead to higher vapor pressure deficits and therefore to more severe droughts [*Cook et al.*, 2014] and to greater stress on ecosystems [*Williams et al.*, 2013; *Restaino et al.*, 2016].

In summary, this dissertation examines connections among the biosphere, atmosphere, hydrosphere, and lithosphere, with a specific emphasis on understanding the environmental drivers of vegetation activity in North American ecosystems. In this research, I show that ecosystem primary productivity, as measured by tree rings and remote sensing, is significantly influenced by the seasonality of climate, particularly by the seasonality of moisture supply. Westerly Pacific storm tracks are largely responsible for delivery of moisture to western North America, and my work shows that northerly shifts of these storm tracks tend to reduce both cool-season water supply and subsequent primary production in much of the northwestern U.S. Using a set of machine learning model experiments based on a continent-wide network of tree-ring data, I also demonstrate that models of tree growth that incorporate topographic and soil characteristics substantially outperform those based solely on climate. Taken together, these findings provide a framework for improving the models used to reconstruct past climate from tree-ring data and to monitor primary production with remote sensing, while also providing additional insight into the potential influences of a warming climate on the biosphere.

## APPENDIX 1: SUPPLEMENTAL FIGURES

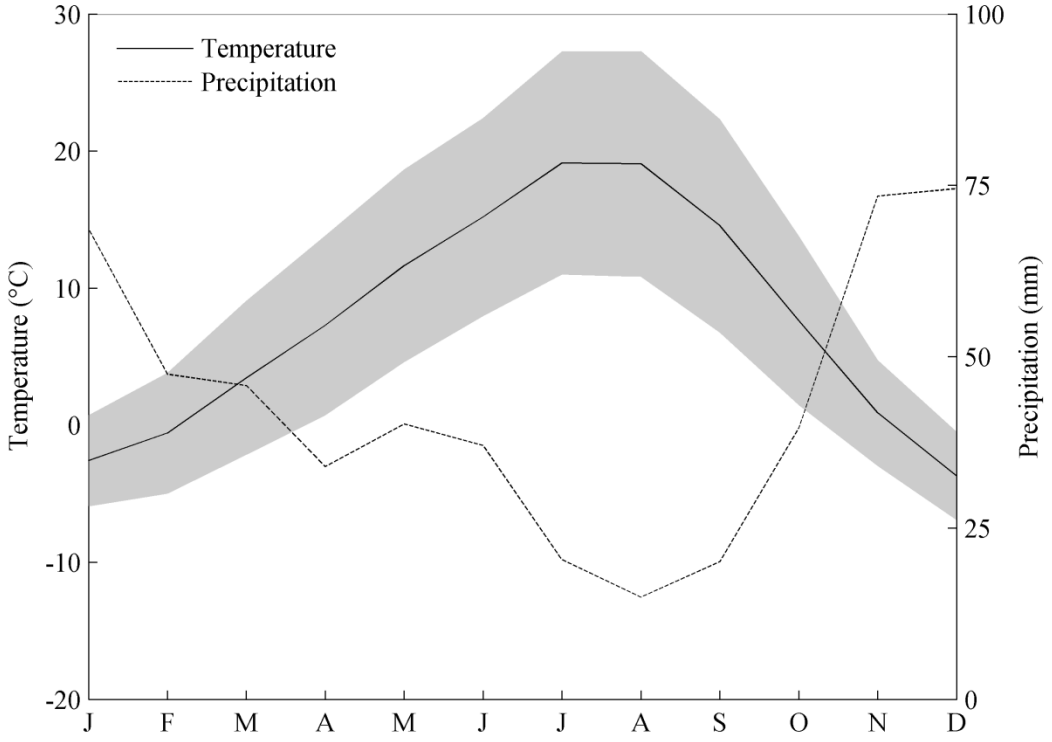


**Figure A1.** Mean monthly temperature (solid line) and precipitation (dotted line) for the period 1981-2010 in the upper CRB. Grey shading shows the range of mean monthly minimum and maximum temperatures.

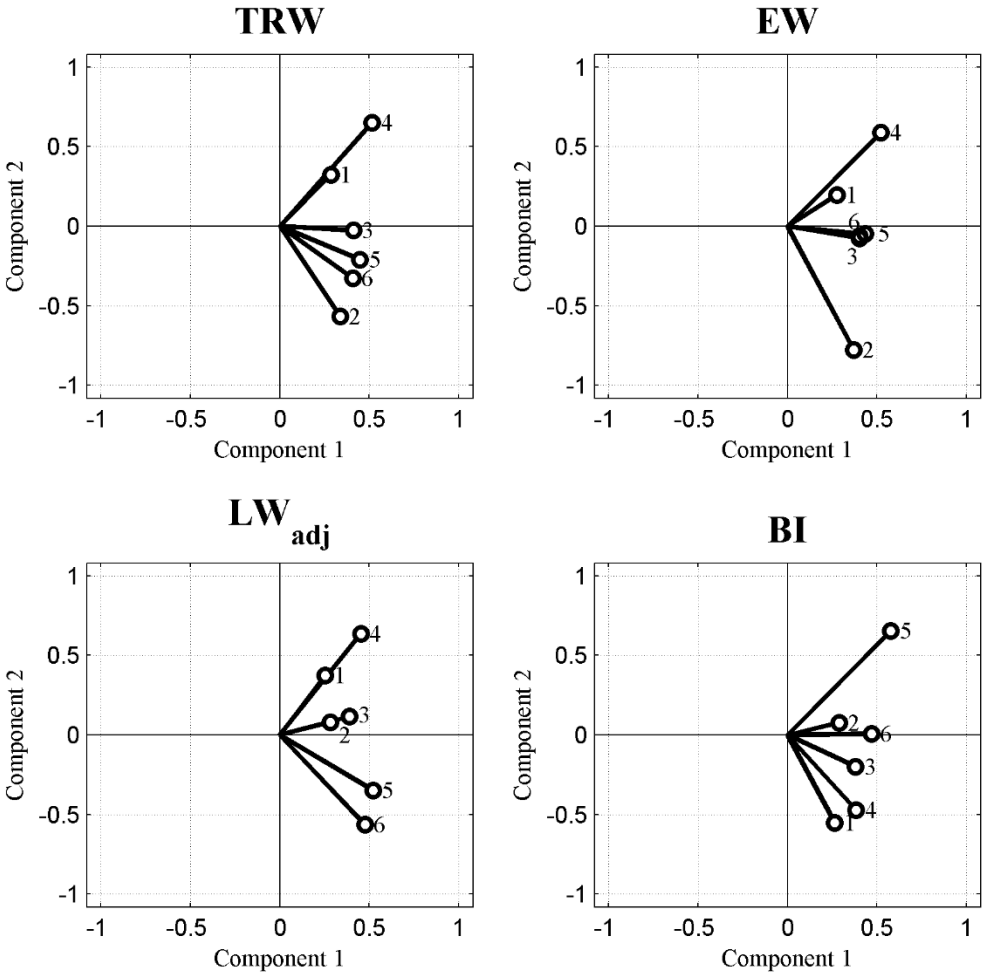


**Figure A2.** Biplot of factor loadings for the first two principal components for each metric.

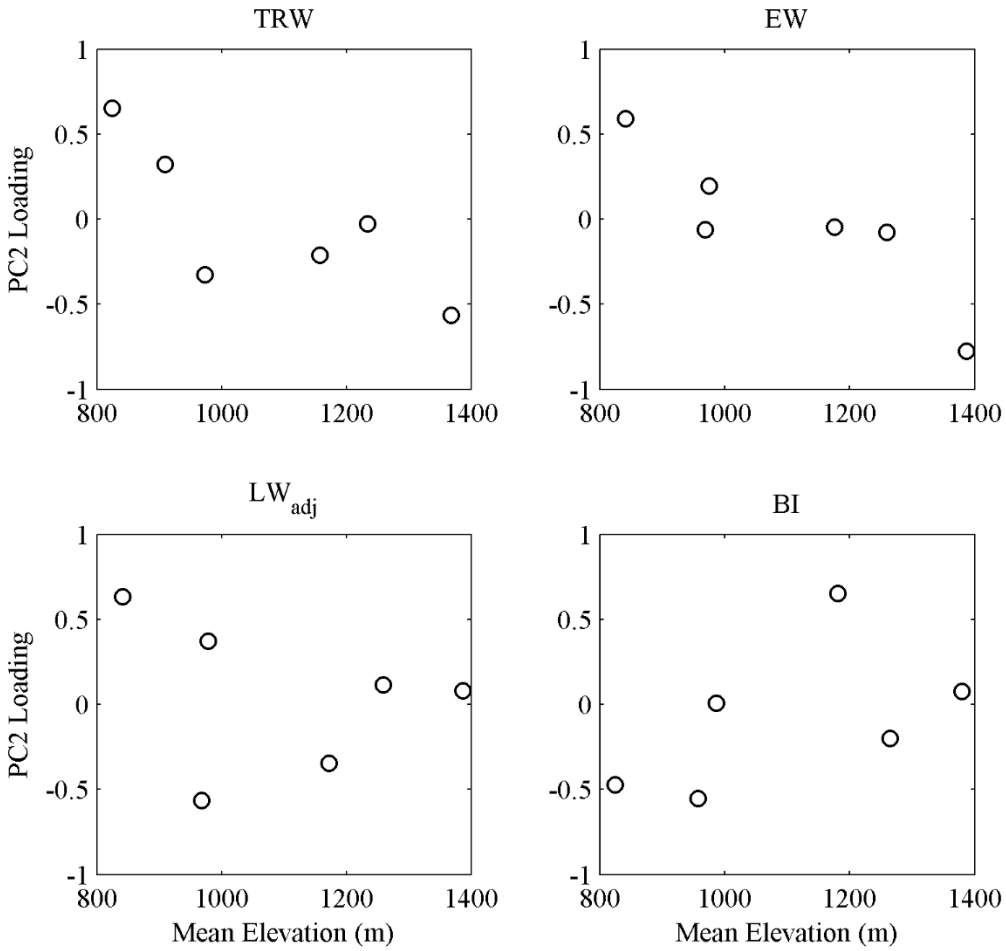


**Figure A3.** Relationship between mean elevation of trees included in each site chronology and PC2 loadings.

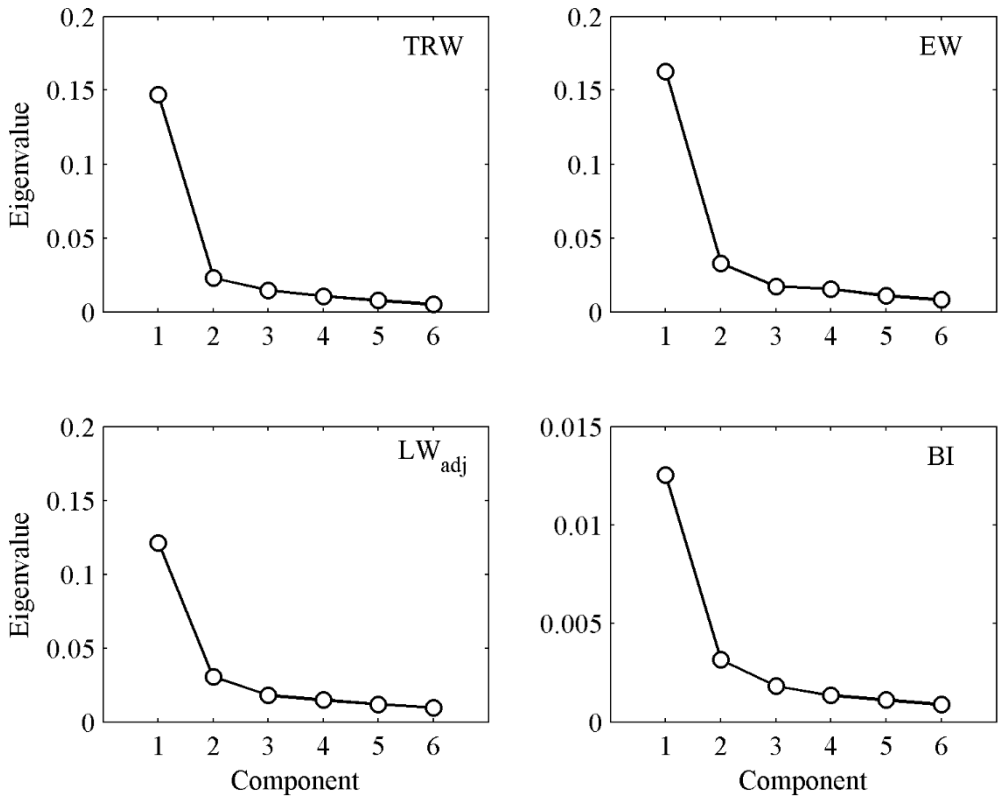


**Figure A4.** Scree plot of PC eigenvalues for each tree-ring metric.

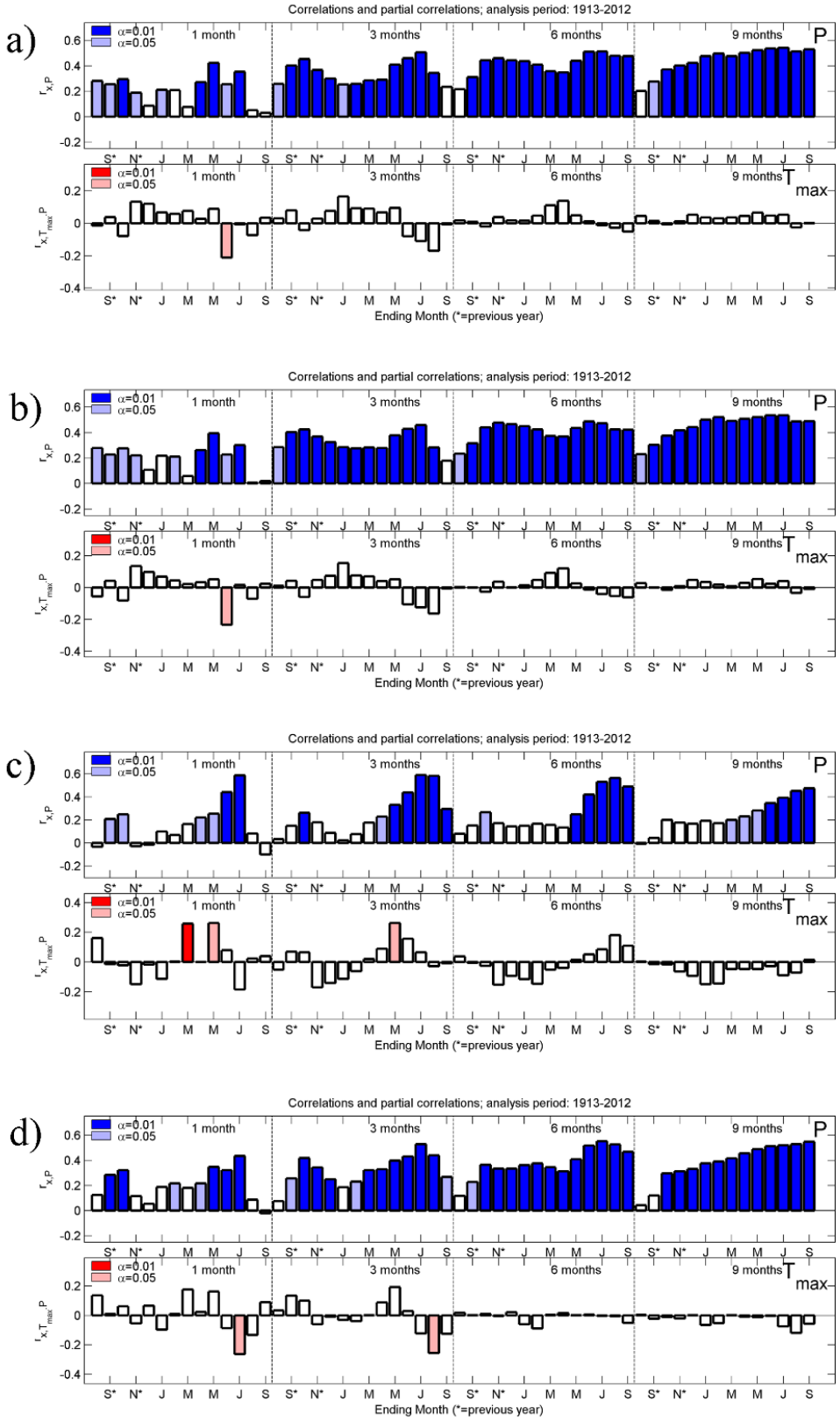


**Figure A5.** Seasonal correlations between precipitation (P; upper panel of each subplot) and maximum temperature ($T_{max}$; lower panel of each subplot) and PC1 of residual chronologies of (a) TRW, (b) EW, (c) $LW_{adj}$, and (d) BI. Figures exported from Seascorr.

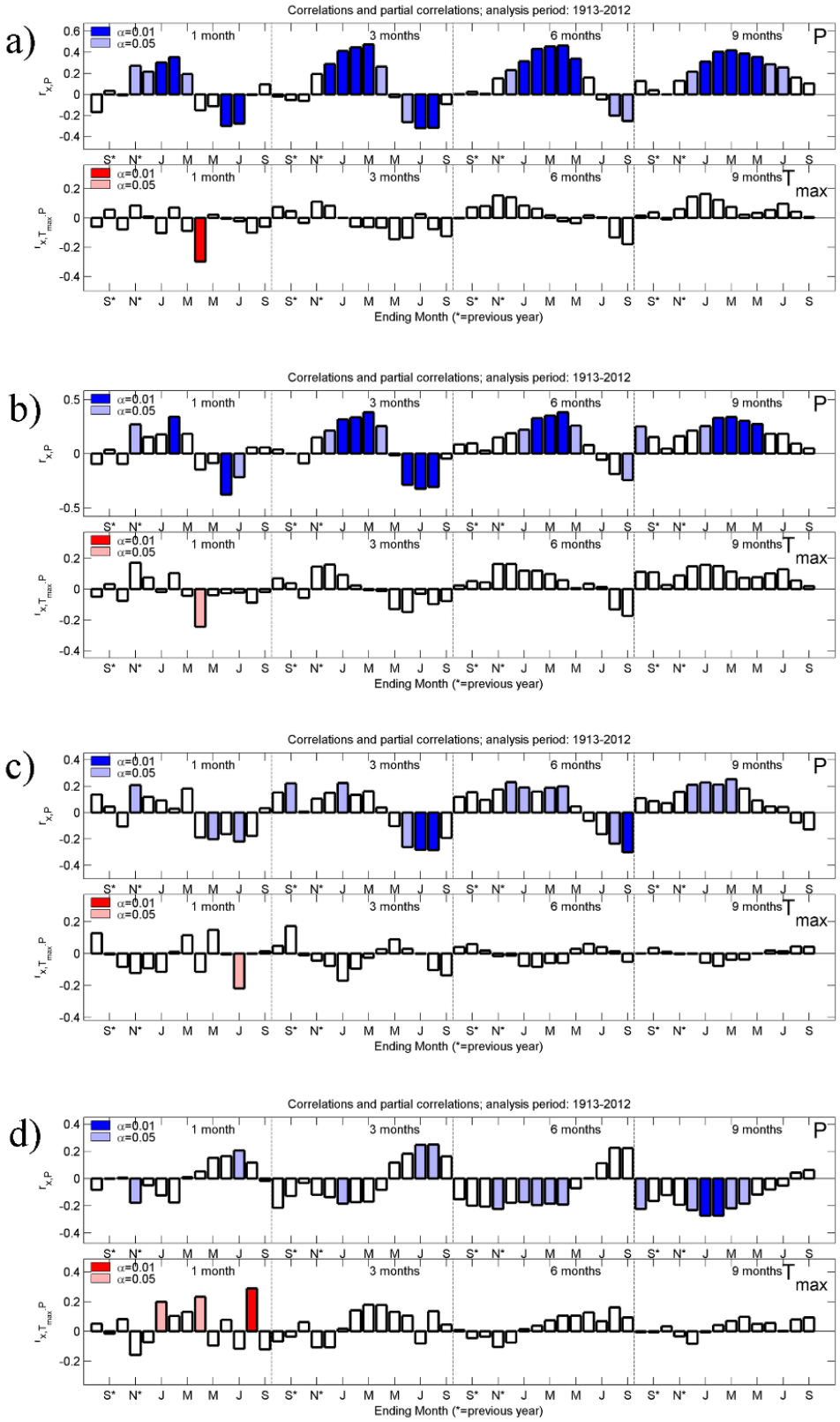


**Figure A6.** Seasonal correlations between precipitation (P; upper panel of each subplot) and maximum temperature ($T_{max}$; lower panel of each subplot) and PC2 of residual chronologies of (a) TRW, (b) EW, (c) $LW_{adj}$, and (d) BI. Figures exported from Seascorr.

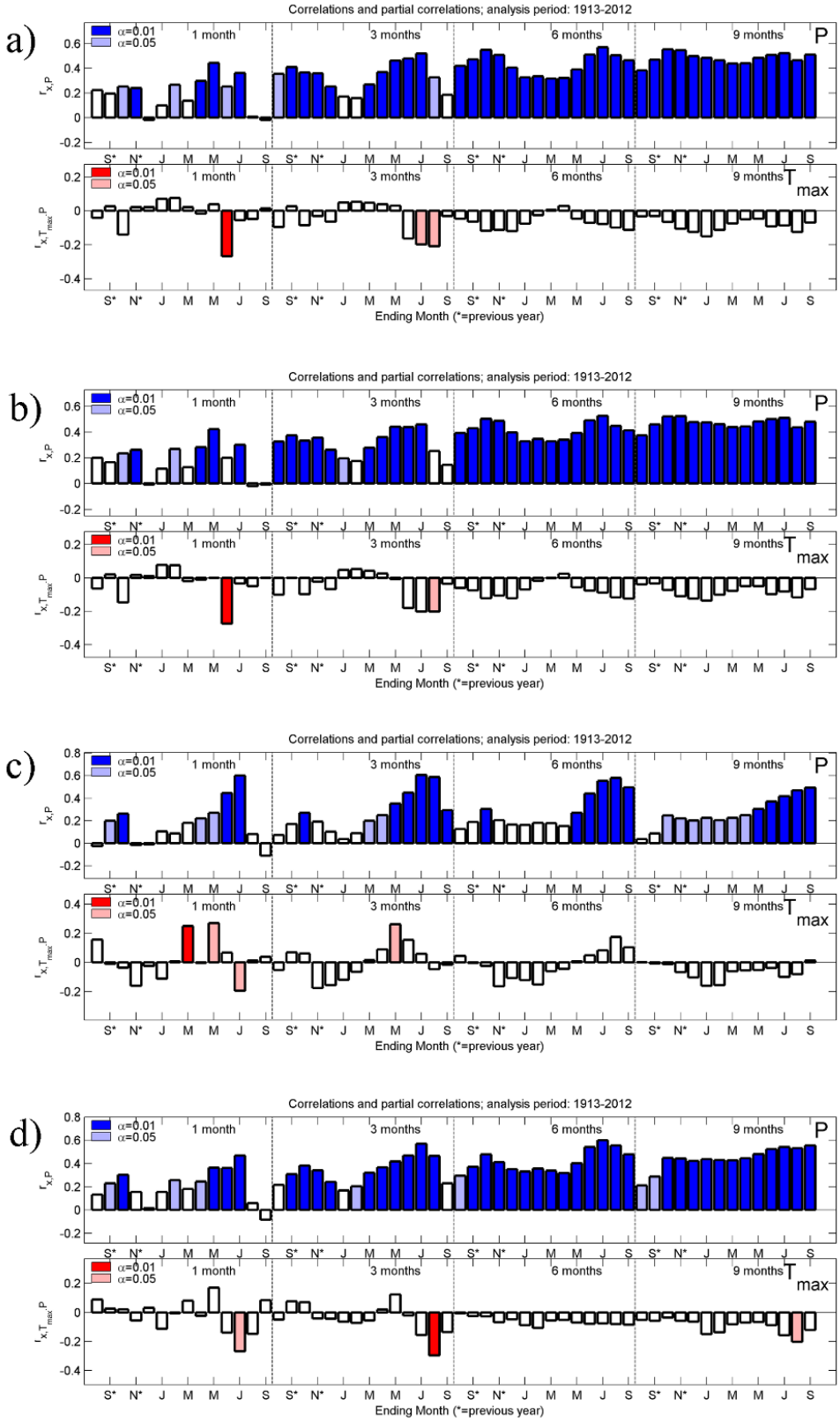


**Figure A7.** Seasonal correlations between precipitation (P; upper panel of each subplot) and maximum temperature ($T_{max}$; lower panel of each subplot) and PC1 of standard chronologies of (a) TRW, (b) EW, (c) $LW_{adj}$, and (d) BI. Figures exported from Seascorr.

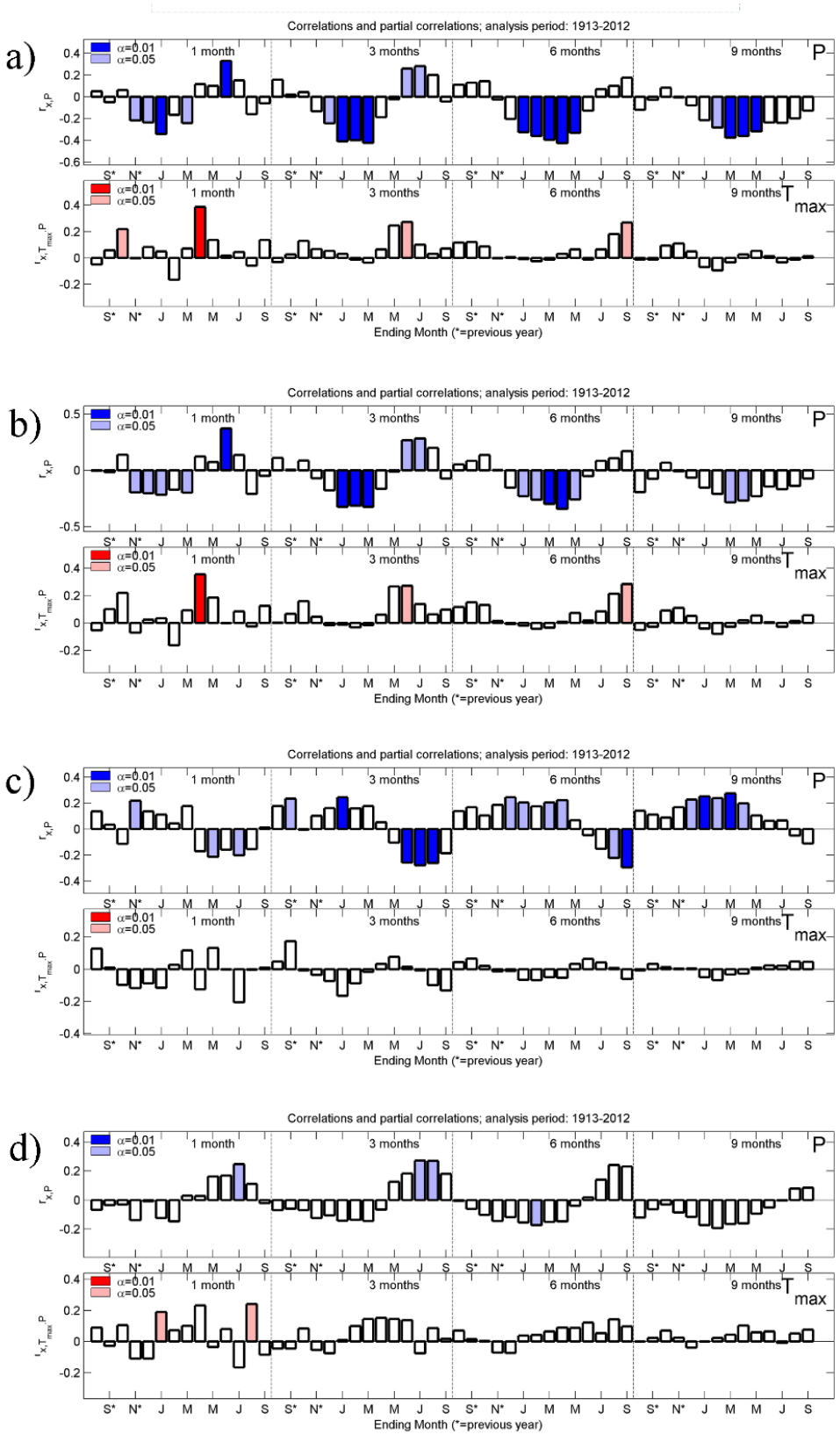


**Figure A8.** Seasonal correlations between precipitation (P; upper panel of each subplot) and maximum temperature ($T_{max}$; lower panel of each subplot) and PC2 of standard chronologies of (a) TRW, (b) EW, (c) $LW_{adj}$, and (d) BI. Figures exported from Seascorr.

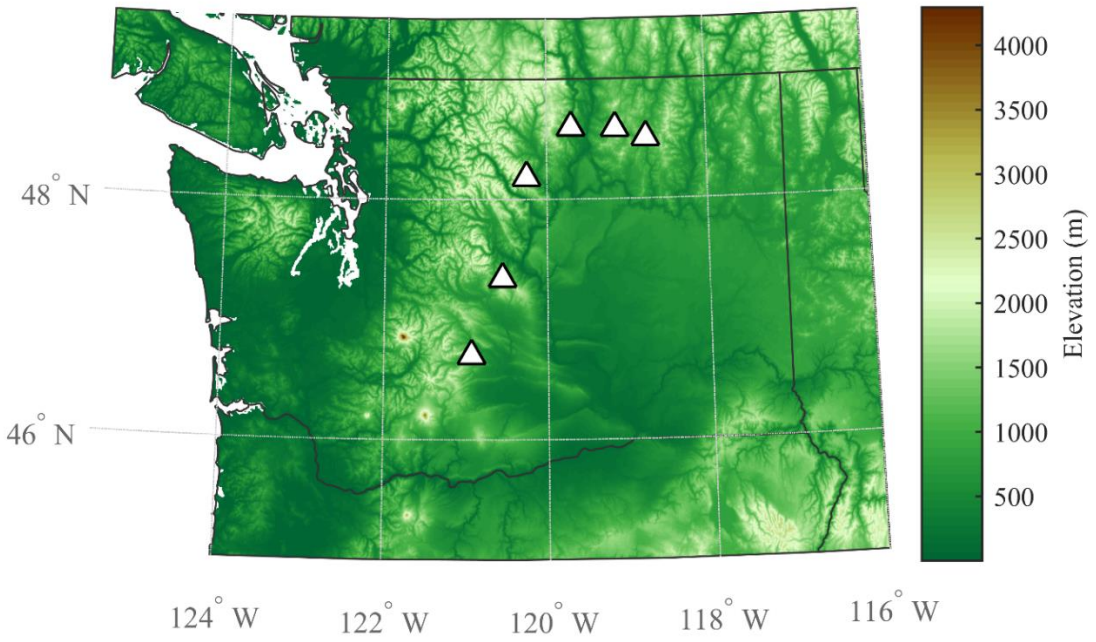


**Figure A9.** Six ponderosa pine tree-ring sites in the Pacific Northwest, where *in situ* DBH measurements are available.

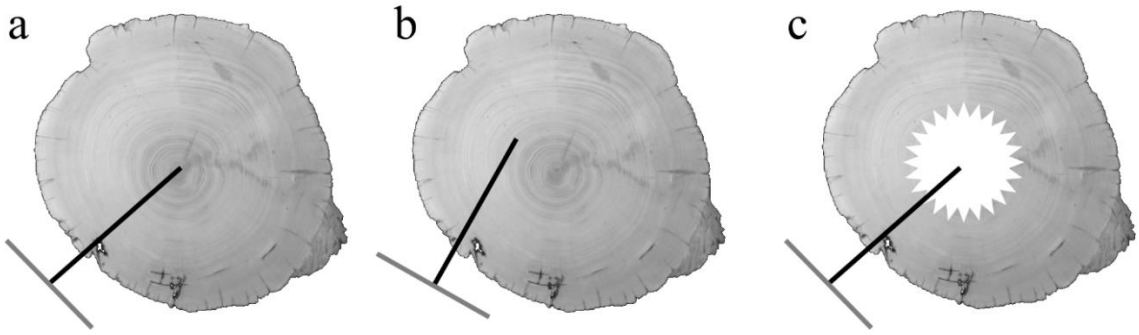


**Figure A10.** Potential outcomes from increment cores. (a) The ideal case where the increment core includes the pith of the tree. (b) Off-center increment core that does not include the inner portion of the tree. (c) Increment core of tree with heartwood rot.

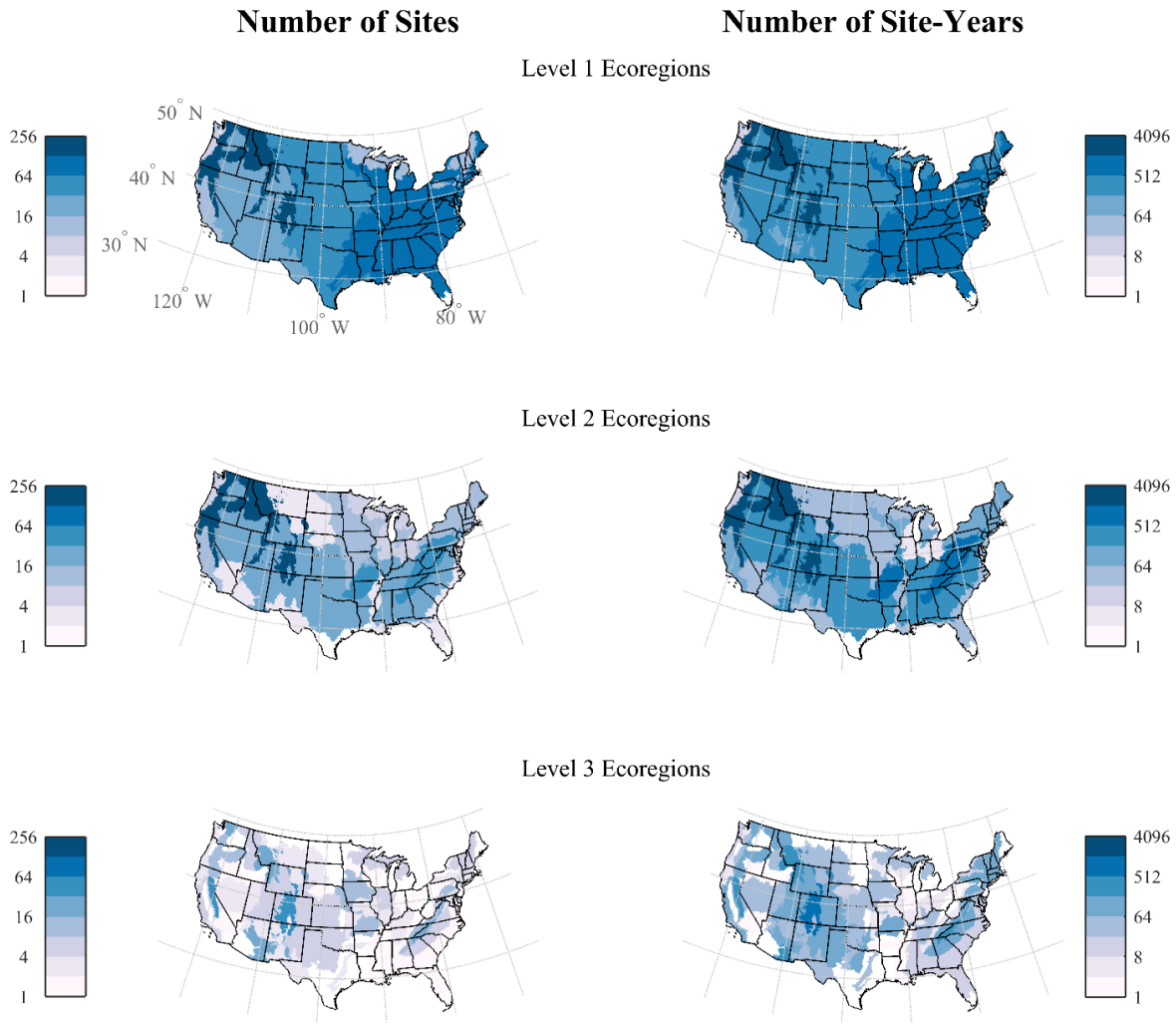


**Figure A11.** Number of tree-ring sites and site-years within each ecoregion.

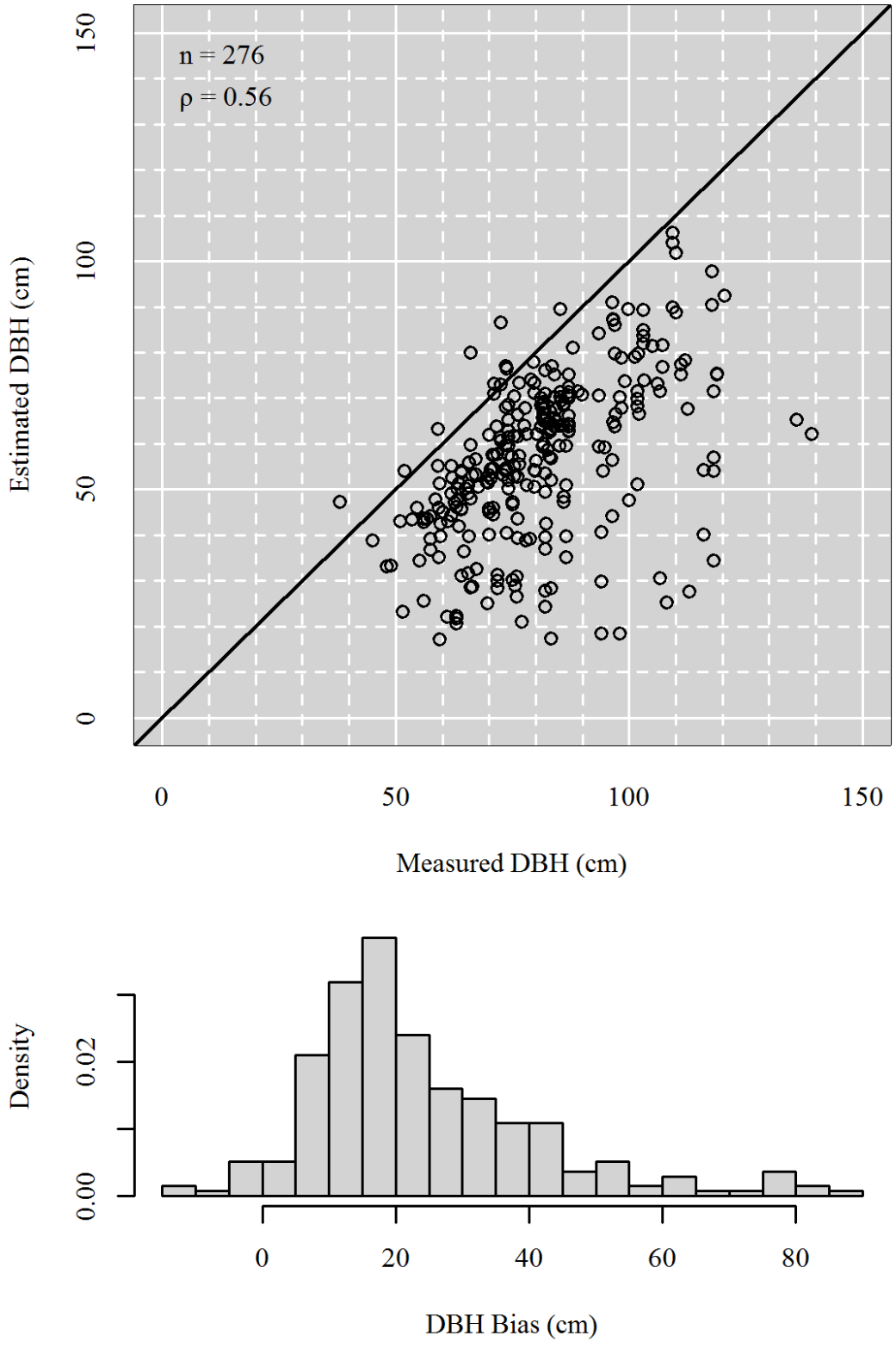


**Figure A12.** Comparison of *in situ* measured DBH to ring-width-based estimates of DBH for 276 increment cores from six sites in the Pacific Northwest.

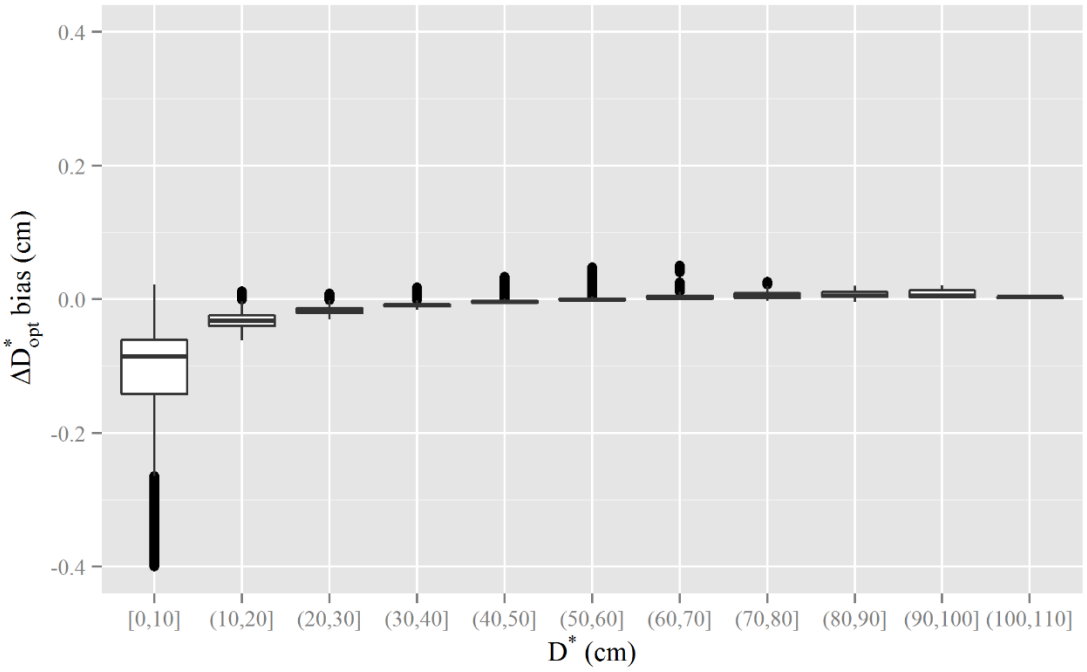


**Figure A13.** Bias in $\Delta D^*_{opt}$ (relative to $\Delta D_{opt}$) for 10 cm diameter classes at six ponderosa pine sites in the Pacific Northwest. Some outliers for $D^*$ = [0,10] lie outside the plot bounds.

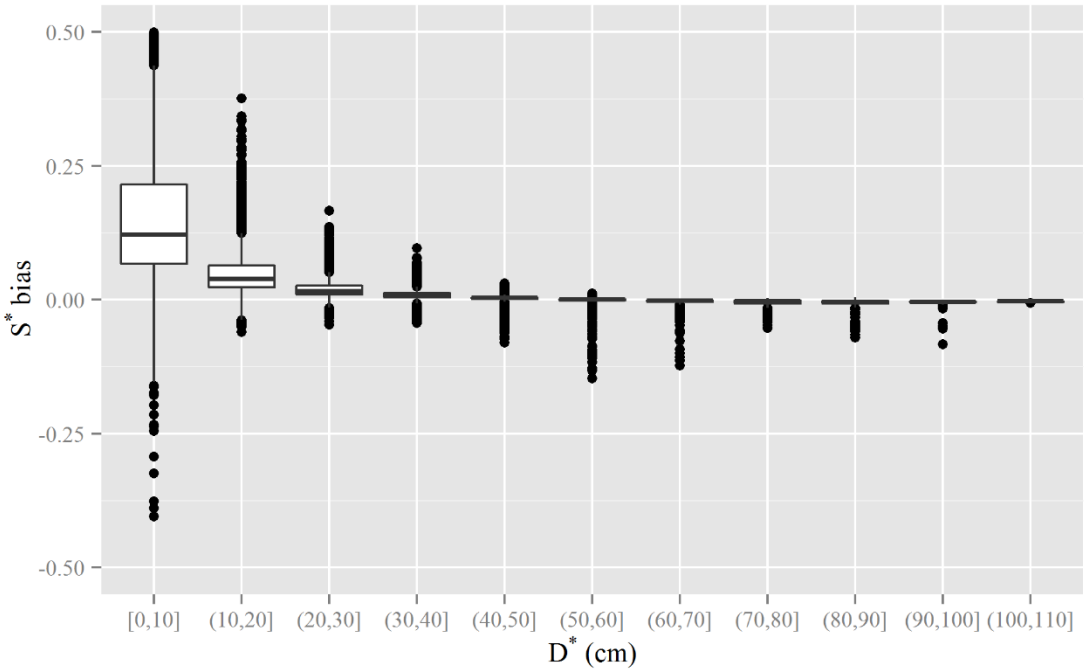


**Figure A14.** Bias in $S^*$ (relative to $S$) for 10 cm diameter classes at six ponderosa pine sites in the Pacific Northwest. Some outliers for $D^*$ = [0,10] lie outside the plot bounds.

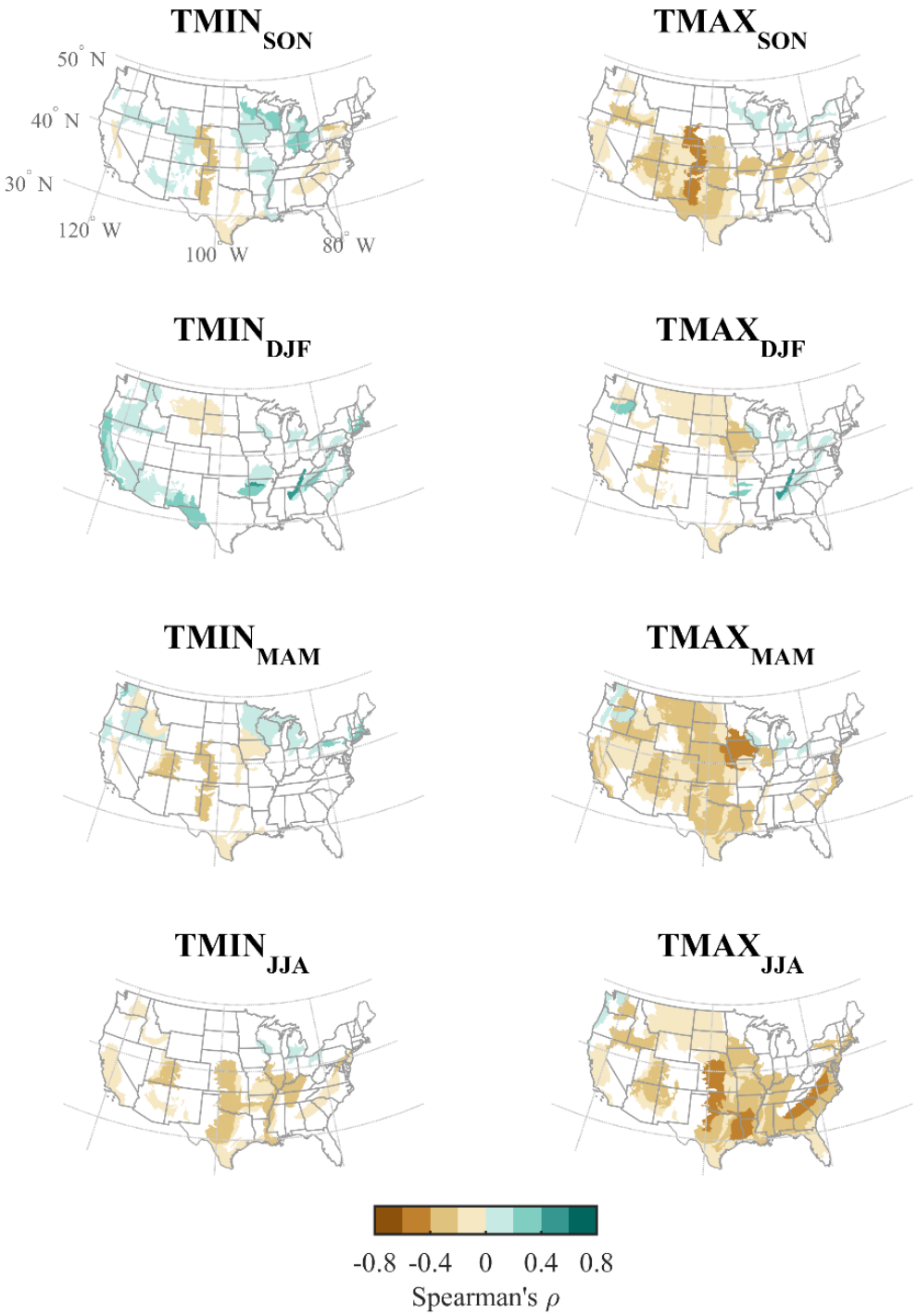


**Figure A15.** Spearman's rank correlation coefficient (ρ) between $S_r$ and seasonal minimum (TMIN) and maximum (TMAX) temperatures. Only ecoregions with significant correlations ($p<0.05$) are shown.

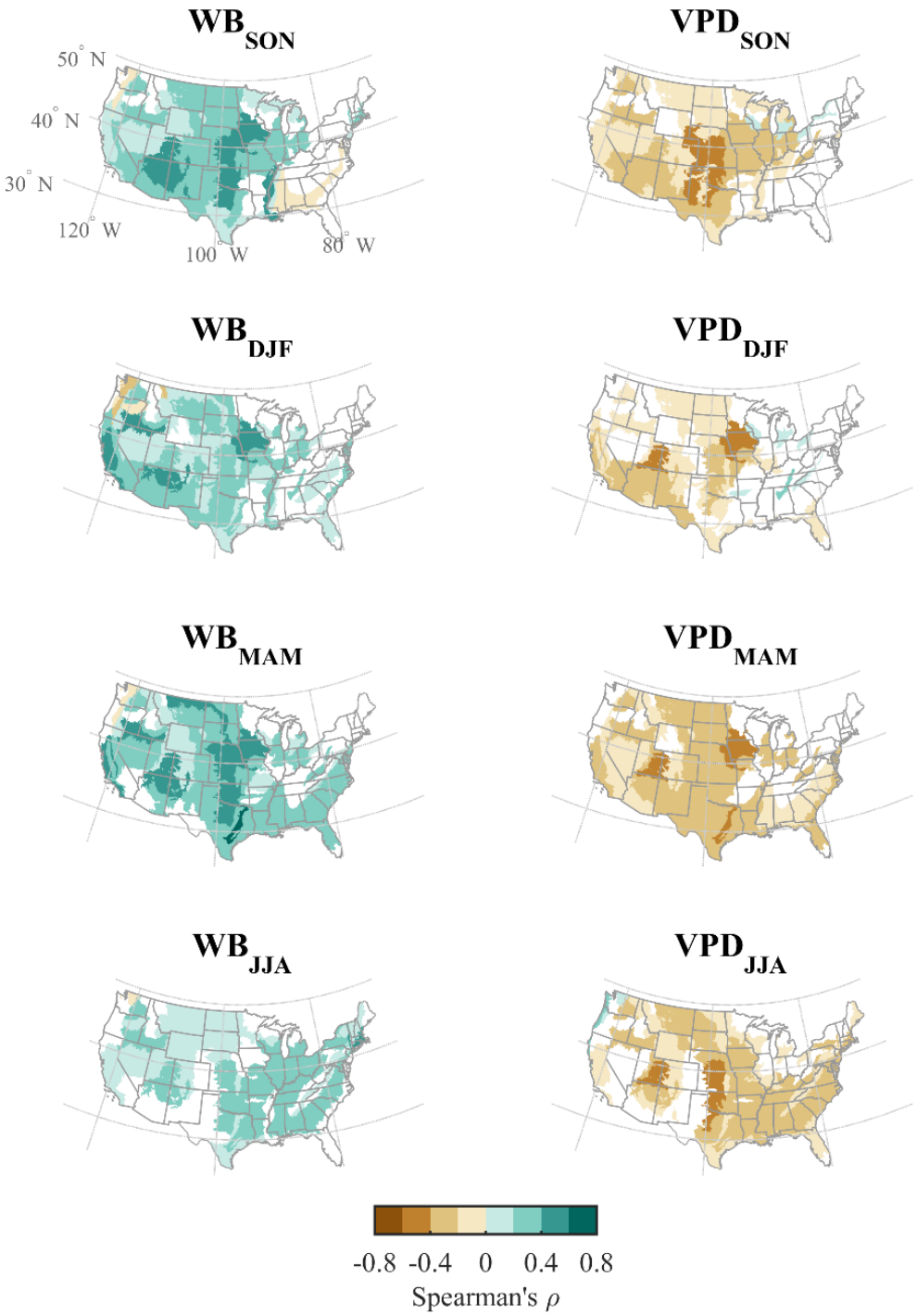


**Figure A16.** Spearman's rank correlation coefficient (ρ) between $S_r$ and seasonal vapor pressure deficit (VPD) and water balance (WB). Only ecoregions with significant correlations ($p<0.05$) are shown.

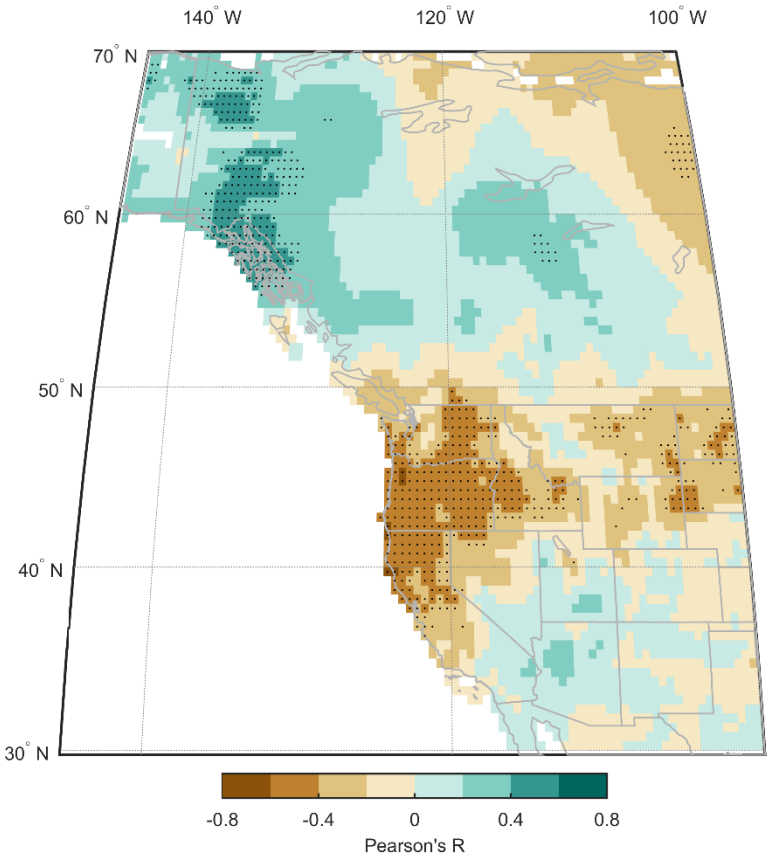


**Figure A17.** Relationship between Pacific storm track position and precipitation. Pearson's correlation coefficient, R, between cool-season Pacific storm track position and the October-March standardized precipitation index (SPI). Grid cells with significant correlations ($P <$ 0.05) to cool-season storm track position are shown with black dots.

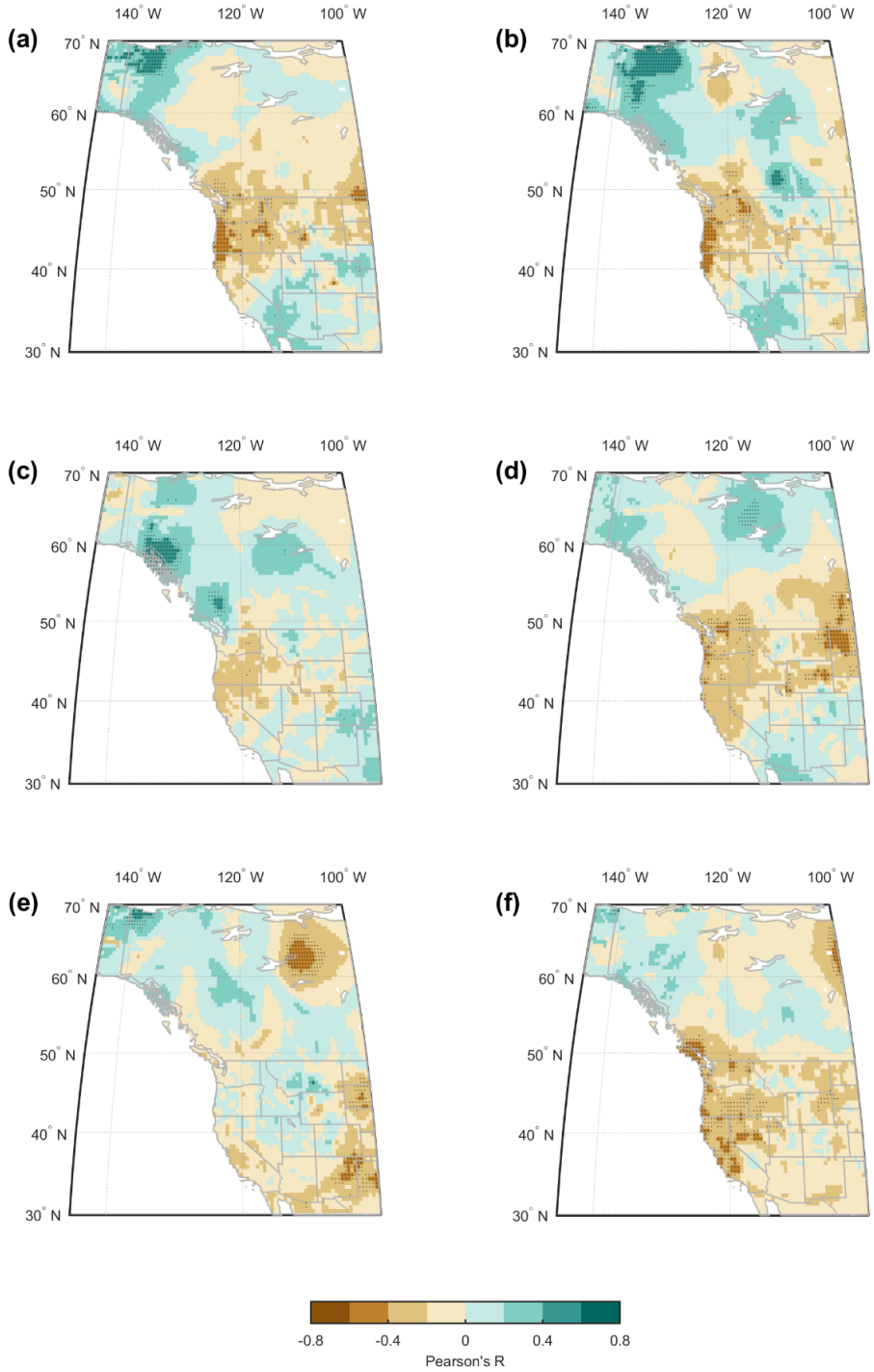


**Figure A18.** Relationship between monthly Pacific storm track position and drought**.** Pearson's correlation coefficient, R, between the October-March standardized precipitation-evapotranspiration index (SPEI) and Pacific storm track position during (a) October, (b) November, (c) December, (d) January, (e) February, and (f) March. SPEI Grid cells with significant correlations ($P < 0.05$) to cool-season storm track position are shown with black dots.

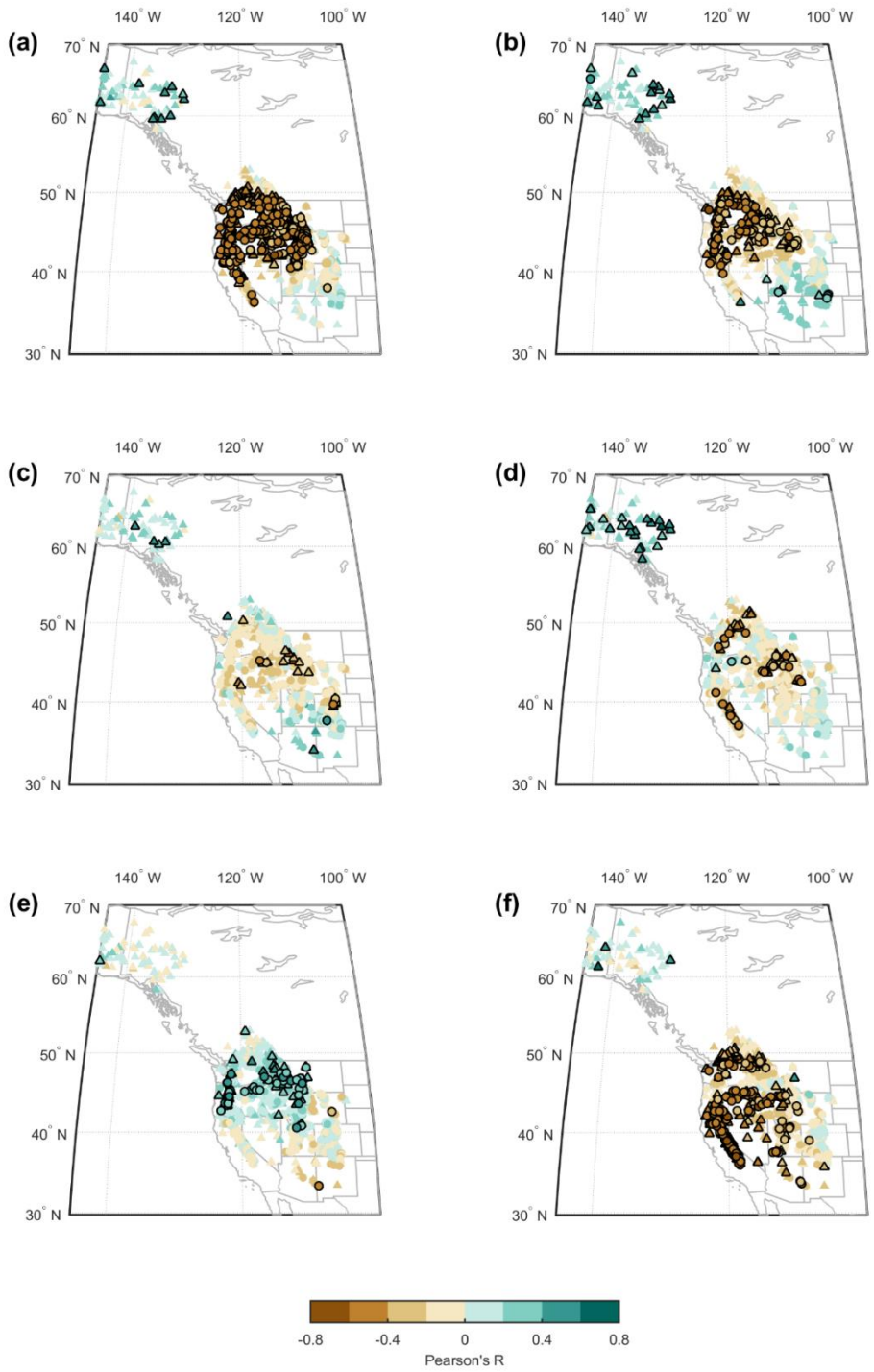


**Figure A19.** Relationship between monthly Pacific storm track position and snowpack**.** Pearson's correlation coefficient, R, between April snow water equivalent (SWE) and Pacific storm track position during (a) October, (b) November, (c) December, (d) January, (e) February, and (f) March. SWE stations with significant correlations to cool-season storm track position are highlighted with black edges. SNOTEL sites are shown as circles, and Snow Course sites are shown as triangles.

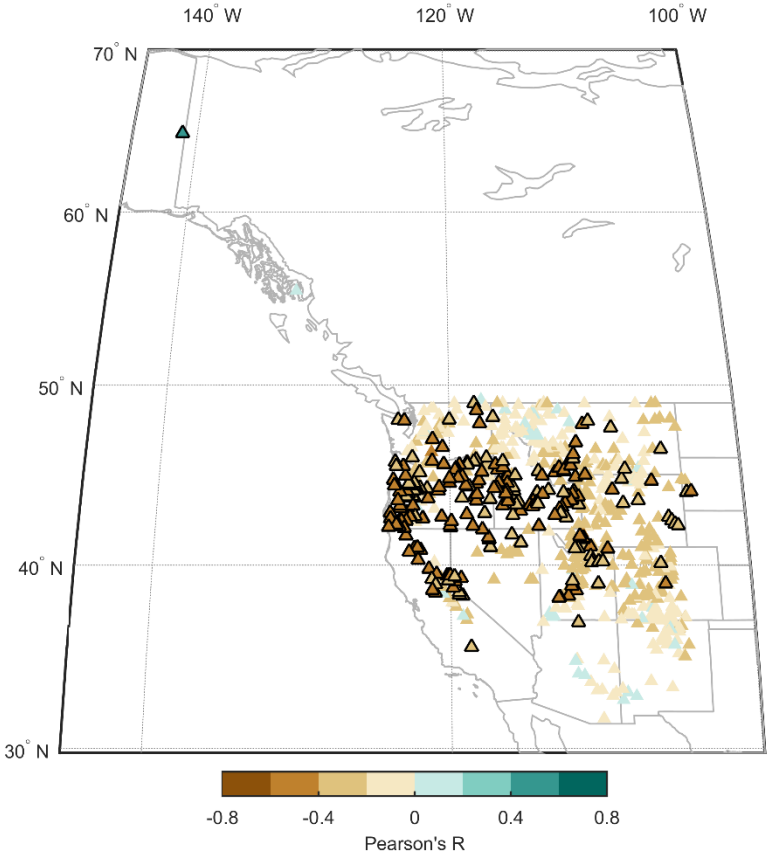


**Figure A20.** Relationship between Pacific storm track position and streamflow. Pearson's correlation coefficient, R, between cool-season storm track position and mean daily stream discharge over the water year from a USGS gauge network. Gauges with significant correlations ($P < 0.05$) to cool-season storm track position are highlighted with black edges.

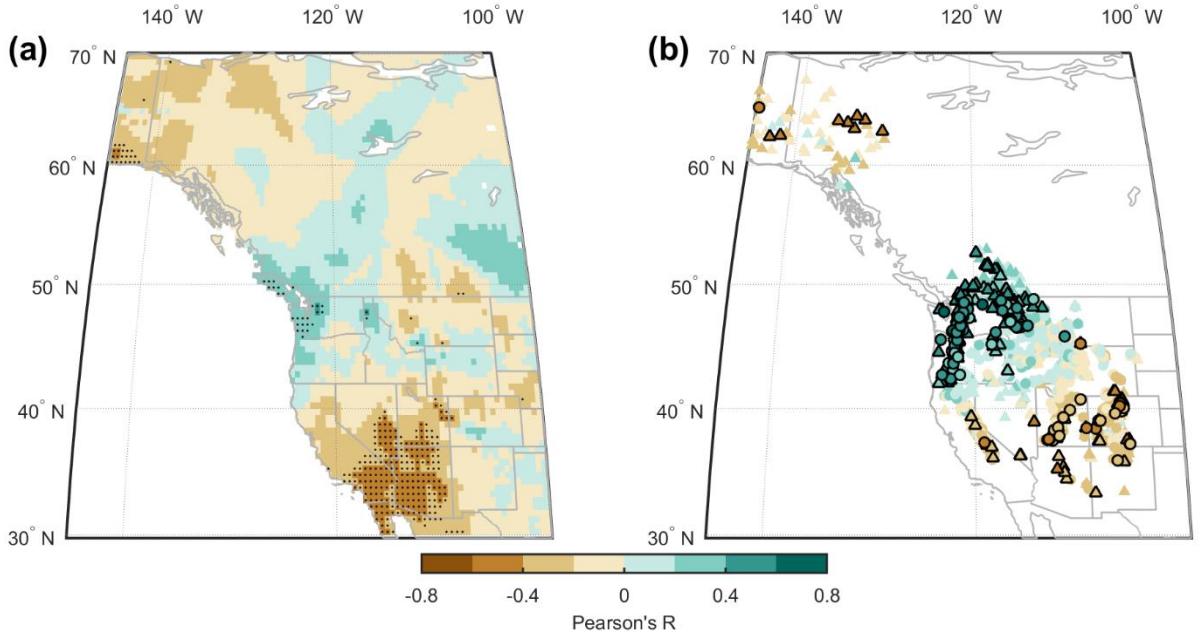


**Figure A21.** Relationship between Pacific storm track intensity and drought and snowpack**.** Pearson's correlation coefficient, R, between cool-season storm track intensity and (a) the October-March standardized precipitation-evapotranspiration index (SPEI) and (b) April snow water equivalent (SWE). SPEI Grid cells with significant correlations ($P < 0.05$) to cool-season storm track intensity are shown with black dots. SWE stations with significant correlations to cool-season storm track intensity are highlighted with black edges. SNOTEL sites are shown as circles, and Snow Course sites are shown as triangles.

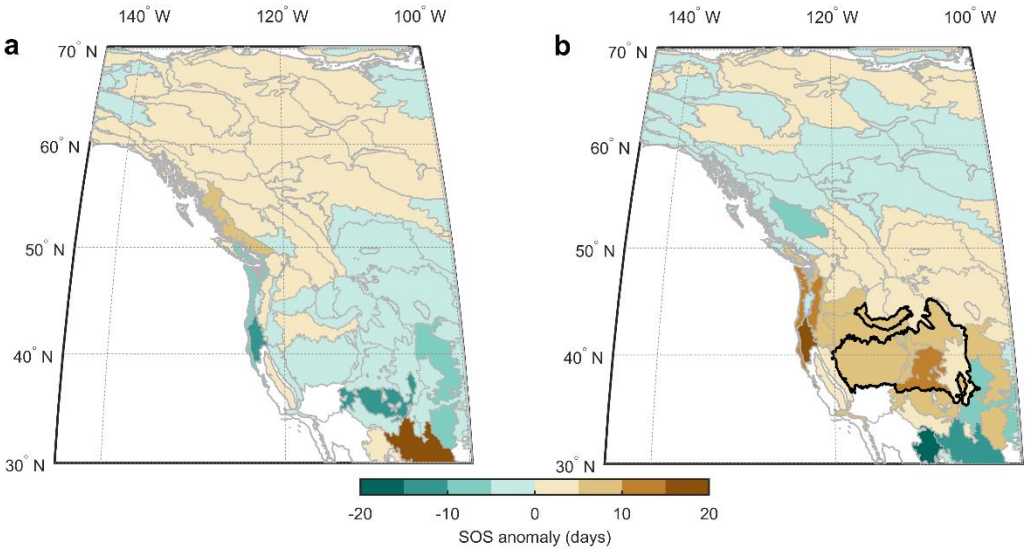


**Figure A22.** Relationship between Pacific storm track position and start of green season. Start of season (SOS) anomalies in years between 1982-2012 with storm track positions in (A) the northernmost 25$^{th}$ percentile and (B) the southernmost 25$^{th}$ percentile. Ecoregions with significant anomalies were determined using a random permutation resampling method (see Methods), and are outlined in black. The mean storm track for each extreme is shown as a dark gray line.

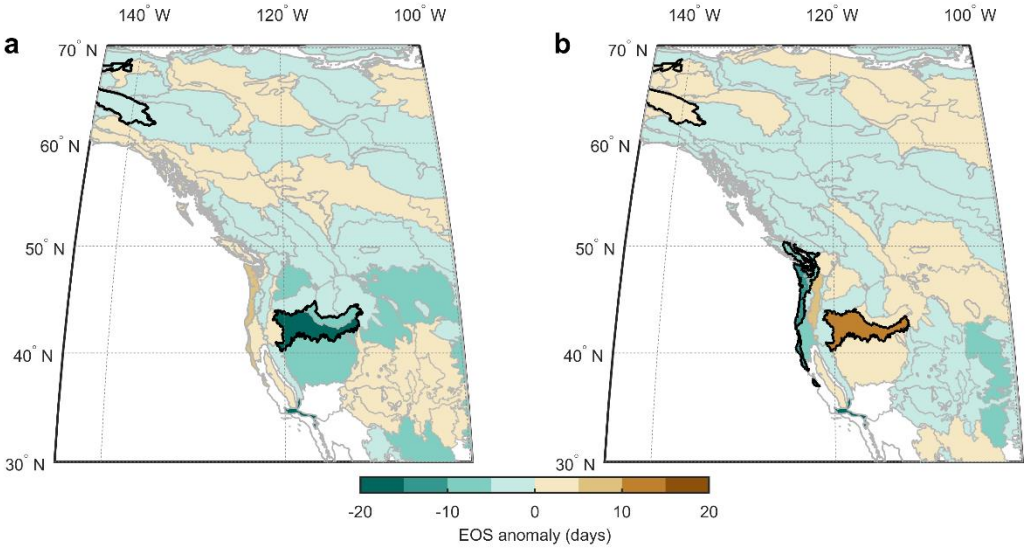


**Figure A23.** Relationship between Pacific storm track position and end of green season. End of season (EOS) anomalies in years between 1982-2012 with storm track positions in (A) the northernmost 25$^{th}$ percentile and (B) the southernmost 25$^{th}$ percentile. Ecoregions with significant anomalies were determined using a random permutation resampling method (see Methods), and are outlined in black. The mean storm track for each extreme is shown as a dark gray line.

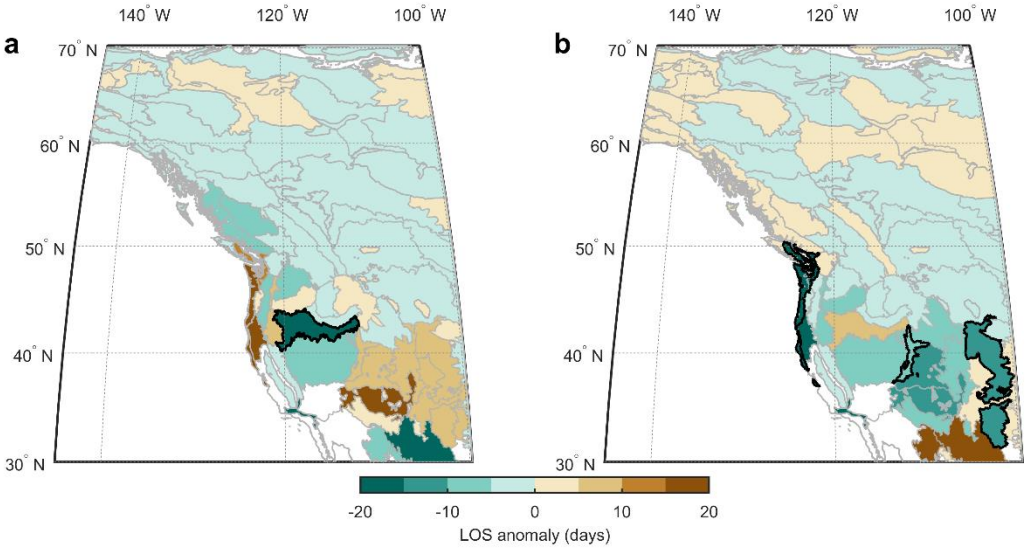


**Figure A24.** Relationship between Pacific storm track position and length of green season. Length of season (LOS) anomalies in years between 1982-2012 with storm track positions in (A) the northernmost 25$^{th}$ percentile and (B) the southernmost 25$^{th}$ percentile. Ecoregions with significant anomalies were determined using a random permutation resampling method (see Methods), and are outlined in black. The mean storm track for each extreme is shown as a dark gray line.

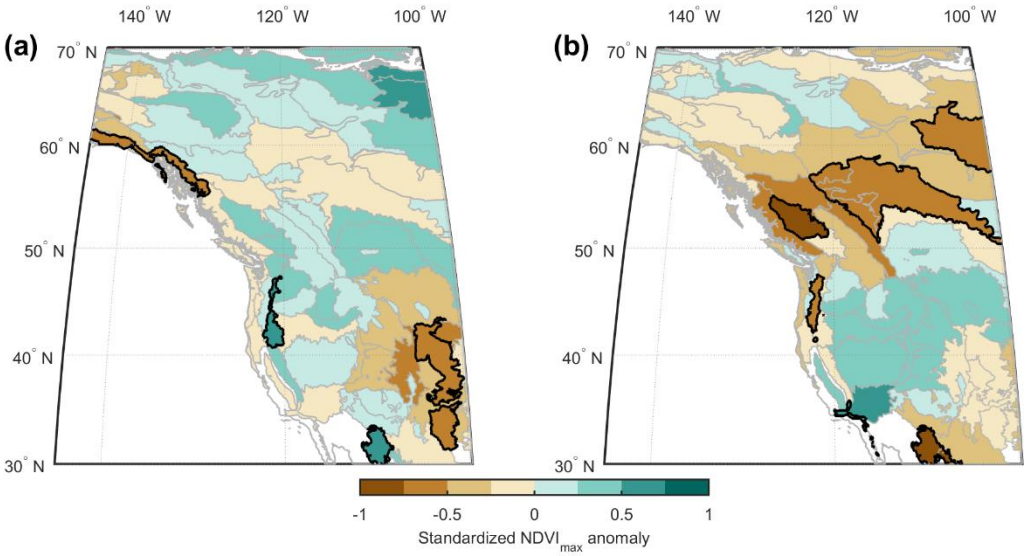


**Figure A25.** Relationship between Pacific storm track intensity and $NDVI_{max}$**.** Standardized $NDVI_{max}$ anomalies in years between 1982-2012 with storm track intensities in (a) the upper 25$^{th}$ percentile and (b) the lower 25$^{th}$ percentile. Ecoregions with significant anomalies are outlined in black.

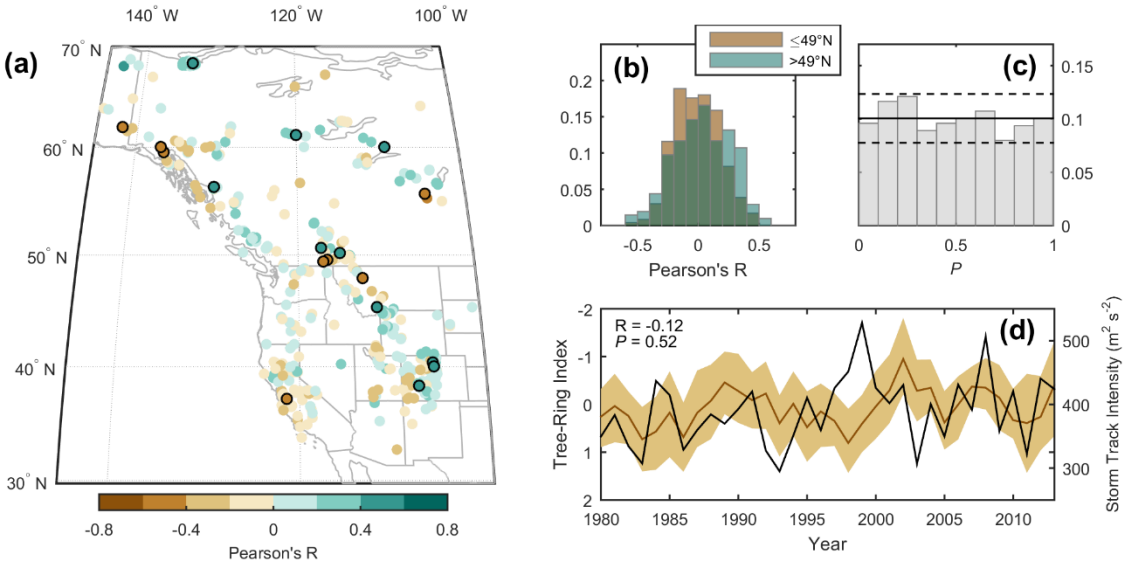


**Figure A26.** Relationship between Pacific storm track intensity and forest growth. (a) Pearson's correlation coefficient, R, between tree-ring widths and cool-season Pacific storm track intensity. Significant correlations ($P < 0.05$) are highlighted with black edges. (b) Distribution of R-values for tree-ring sites south of 49°N (brown bars) and north of 49°N (green bars). (c) Distribution of *P*-values from local significance tests (gray bars; n=438). The expected number of sites with *P*-values falling within each 0.1 increment range is shown as a black line, with dashed lines showing the 5$^{th}$ and 95$^{th}$ percentiles based on the binomial distribution. (d) Correlation between storm track intensity (black line) and a mean growth index for all sites south of 49°N (dark brown line), with the 20$^{th}$ to 80$^{th}$ percentile range shown in light brown. Note that the left y-axis is inverted.

## APPENDIX 2: SUPPLEMENTAL TABLES

**Table A1.** Summary of tree-ring chronologies over the period 1913-2012.

| | # of trees | # of cores | $RBAR_{eff}$ | EPS |
|---|---|---|---|---|
| Site 1 | | | | |
| TRW | 23 | 42 | 0.286 | 0.897 |
| EW | 16 | 24 | 0.278 | 0.856 |
| $LW_{adj}$ | 15 | 22 | 0.223 | 0.806 |
| BI | 10 | 15 | 0.280 | 0.794 |
| Site 2 | | | | |
| TRW | 38 | 55 | 0.328 | 0.948 |
| EW | 12 | 19 | 0.419 | 0.896 |
| $LW_{adj}$ | 12 | 19 | 0.264 | 0.810 |
| BI | 11 | 15 | 0.307 | 0.820 |
| Site 3 | | | | |
| TRW | 40 | 62 | 0.437 | 0.968 |
| EW | 14 | 24 | 0.428 | 0.913 |
| $LW_{adj}$ | 14 | 24 | 0.306 | 0.860 |
| BI | 9 | 16 | 0.380 | 0.846 |
| Site 4 | | | | |
| TRW | 26 | 40 | 0.545 | 0.968 |
| EW | 12 | 18 | 0.625 | 0.951 |
| $LW_{adj}$ | 12 | 16 | 0.294 | 0.827 |
| BI | 9 | 14 | 0.355 | 0.828 |
| Site 5 | | | | |
| TRW | 29 | 50 | 0.495 | 0.965 |
| EW | 13 | 23 | 0.457 | 0.915 |
| $LW_{adj}$ | 12 | 20 | 0.374 | 0.877 |
| BI | 6 | 12 | 0.441 | 0.825 |
| Site 6 | | | | |
| TRW | 26 | 43 | 0.484 | 0.960 |
| EW | 11 | 18 | 0.529 | 0.925 |
| $LW_{adj}$ | 11 | 16 | 0.344 | 0.851 |
| BI | 7 | 13 | 0.466 | 0.857 |

**Table A2.** Mean inter-series correlations between trees ($RBAR_{bt}$), within trees ($RBAR_{wt}$), and total ($RBAR_{tot}$); effective mean inter-series correlations ($RBAR_{eff}$); signal-to-noise ratio (SNR); and expressed population signal (EPS) for CooRecorder parameter sets over the period 1913-2012.

| Width | Depth | % Blue | $RBAR_{eff}$ | EPS |
|---|---|---|---|---|
| 40 | 10 | 15 | 0.376 | 0.707 |
| 40 | 10 | 30 | 0.373 | 0.704 |
| 40 | 10 | 60 | 0.363 | 0.695 |
| 40 | 10 | 90 | 0.347 | 0.680 |
| 40 | 50 | 15 | 0.363 | 0.695 |
| 40 | 50 | 30 | 0.362 | 0.694 |
| 40 | 50 | 60 | 0.346 | 0.679 |
| 40 | 50 | 90 | 0.331 | 0.664 |
| 100 | 10 | 15 | 0.376 | 0.706 |
| **100** | **10** | **30** | **0.380** | **0.710** |
| 100 | 10 | 60 | 0.382 | 0.712 |
| 100 | 10 | 90 | 0.376 | 0.706 |
| 100 | 50 | 15 | 0.368 | 0.699 |
| 100 | 50 | 30 | 0.367 | 0.699 |
| 100 | 50 | 60 | 0.350 | 0.683 |
| 100 | 50 | 90 | 0.333 | 0.667 |
| 160 | 10 | 15 | 0.335 | 0.667 |
| 160 | 10 | 30 | 0.345 | 0.678 |
| 160 | 10 | 60 | 0.349 | 0.682 |
| 160 | 10 | 90 | 0.344 | 0.677 |
| 160 | 50 | 15 | 0.311 | 0.643 |
| 160 | 50 | 30 | 0.318 | 0.651 |
| 160 | 50 | 60 | 0.298 | 0.630 |
| 160 | 50 | 90 | 0.285 | 0.615 |
| 240 | 10 | 15 | 0.350 | 0.682 |
| 240 | 10 | 30 | 0.349 | 0.682 |
| 240 | 10 | 60 | 0.353 | 0.686 |
| 240 | 10 | 90 | 0.341 | 0.674 |
| 240 | 50 | 15 | 0.332 | 0.665 |
| 240 | 50 | 30 | 0.333 | 0.667 |
| 240 | 50 | 60 | 0.312 | 0.644 |
| 240 | 50 | 90 | 0.290 | 0.620 |
| 40 | - | - | 0.358 | |
| **100** | **-** | **-** | **0.367** | |
| 160 | - | - | 0.323 | |
| 240 | - | - | 0.333 | |
| **-** | **10** | **-** | **0.359** | |
| - | 50 | - | 0.331 | |

| | | | |
|---|---|---|---|
| - | - | 15 | 0.351 |
| **-** | **-** | **30** | **0.353** |
| - | - | 60 | 0.344 |
| - | - | 90 | 0.331 |

**Table A3.** Percent variance explained by PC1 and PC2 of each tree-ring metric.

| | PC1 | PC2 | Total |
|---|---|---|---|
| TRW | 70.7 | 11.0 | 81.7 |
| EW | 65.8 | 13.3 | 79.2 |
| $LW_{adj}$ | 58.8 | 14.8 | 73.6 |
| BI | 60.1 | 15.2 | 75.3 |

**Table A4.** Species present in ITRDB sites used in this study (with the number, *n*, of sites for each species), and parameters used in the optimal growth model: growth rate factor (G), maximum diameter ($D_{max}$, in cm), maximum height ($H_{max}$, in cm), and maximum age ($AGE_{max}$).

| Code | Species | Common Name | *n* | G | $D_{max}$ | $H_{max}$ | $AGE_{max}$ |
|---|---|---|---|---|---|---|---|
| ABAM | *Abies amabilis* | Pacific Silver Fir | 1 | 84.5 | 260 | 7190 | 725 |
| ABCO | *Abies concolor* | White Fir | 6 | 106.3 | 270 | 7500 | 600 |
| ABLA | *Abies lasiocarpa* | Subalpine Fir | 3 | 90.8 | 210 | 5270 | 500 |
| ABMA | *Abies magnifica* | Calif. Red Fir | 7 | 130.7 | 300 | 7680 | 500 |
| CADE | *Calocedrus decurrens* | Calif. Incense Cedar | 1 | 64.1 | 390 | 6980 | 933 |
| CYGL | *Carya glabra* | Pignut Hickory | 1 | 131 | 120 | 4570 | 300[a] |
| LALY | *Larix lyalli* | Subalpine Larch | 6 | 34.5 | 210 | 3080 | 800 |
| LITU | *Liriodendron tulipifera* | Tulip-poplar | 11 | 115.6 | 340 | 5330 | 400 |
| PCEN | *Picea engelmannii* | Engelman Spruce | 23 | 68.1 | 240 | 6800 | 852 |
| PCRU | *Picea rubens* | Red Spruce | 3 | 92.9 | 150 | 4630 | 430 |
| PIAL | *Pinus albicaulis* | Whitebark Pine | 3 | 27.2 | 270 | 2620 | 880 |
| PIBA | *Pinus balfouriana* | Foxtail Pine | 7 | 15.2 | 260 | 3600 | 2100 |
| PICO | *Pinus contorta* | Lodgepole Pine | 6 | 66.2 | 210 | 4570 | 600 |
| PIEC | *Pinus echinata* | Shortleaf Pine | 7 | 95.8 | 120 | 4450 | 400 |
| PIFL | *Pinus flexilis* | Limber Pine | 8 | 14.1 | 230 | 2590 | 1670 |
| PIJE | *Pinus jeffreyi* | Jeffrey Pine | 14 | 77.1 | 240 | 6310 | 700[b] |
| PILA | *Pinus lambertiana* | Sugar Pine | 7 | 89.4 | 350 | 7990 | 760 |
| PIPO | *Pinus ponderosa* | Ponderosa Pine | 114 | 66.2 | 270 | 7800 | 1000 |
| PIRE | *Pinus resinosa* | Red Pine | 4 | 88.8 | 150 | 3540 | 350 |
| PIST | *Pinus strobus* | Eastern White Pine | 4 | 124 | 180 | 6710 | 460 |
| PITA | *Pinus taeda* | Loblolly Pine | 1 | 122.8 | 210 | 4970 | 350[a] |
| PSMA | *Pseudotsuga macrocarpa* | Bigcone Douglas-Fir | 3 | 75.8 | 230 | 5270 | 600 |
| PSME | *Pseudotsuga menziesii* | Douglas-Fir | 94 | 56.7 | 425[b] | 8500[b] | 1275 |
| QUAL | *Quercus alba* | White Oak | 46 | 88.6 | 270 | 4570 | 450 |
| QUCO | *Quercus coccinea* | Scarlet Oak | 2 | 69 | 150 | 3110 | 400 |
| QULO | *Quercus lobata* | Valley Oak | 3 | 170.4 | 370 | 4880 | 250 |
| QULY | *Quercus lyrata* | Overcup Oak | 3 | 84.4 | 210 | 3840 | 400 |
| QUMA | *Quercus macrocarpa* | Bur Oak | 4 | 76.2 | 210 | 3810 | 440 |
| QUPR | *Quercus prinus* | Chestnut Oak | 8 | 99.3 | 210 | 4570 | 400 |
| QURU | *Quercus rubra* | Red Oak | 4 | 93.4 | 240 | 4270 | 400[a] |
| QUST | *Quercus stellata* | Post Oak | 21 | 70.8 | 150 | 3200 | 400 |
| QUVE | *Quercus velutina* | Black Oak | 5 | 199 | 240 | 4570 | 200 |
| TSCA | *Tsuga canadensis* | Eastern Hemlock | 22 | 82.9 | 210 | 5180 | 539 |
| TSME | *Tsuga mertensiana* | Mountain Hemlock | 10 | 63.3 | 210 | 5910 | 800[b] |

[a] Shugart (1984)

[b] Urban *et al.* (1993)

**Table A5.** Variance explained ($r^2$) by ecoregion RF models of absolute stress (based on out-of-bag observations) for the four model experiments.

| | | | $r^2$ | | | |
|---|---|---|---|---|---|---|
| Ecoregion | Sites | n | TSC | TC | SC | C |
| 5.0 Northern Forests | 16 | 343 | 0.81 | 0.80 | 0.81 | 0.16 |
| 5.2 Mixed Wood Shield | 7 | 104 | 0.52 | 0.50 | 0.54 | 0.06 |
| 5.2.1 Northern Lakes and Forests | 7 | 104 | 0.53 | 0.50 | 0.54 | 0.04 |
| 5.3 Atlantic Highlands | 9 | 239 | 0.81 | 0.81 | 0.80 | 0.25 |
| 5.3.1 Northern Appalachians and Atlantic Maritime Highlands | 7 | 217 | 0.81 | 0.81 | 0.80 | 0.26 |
| 6.0 Northwestern Forested Mountains | 214 | 4875 | 0.69 | 0.65 | 0.66 | 0.36 |
| 6.2 Western Cordillera | 214 | 4875 | 0.69 | 0.65 | 0.65 | 0.36 |
| 6.2.3 Columbia Mountains/Northern Rockies | 6 | 199 | 0.72 | 0.71 | 0.71 | 0.53 |
| 6.2.4 Canadian Rockies | 4 | 116 | 0.54 | 0.55 | 0.53 | 0.29 |
| 6.2.5 North Cascades | 23 | 369 | 0.07 | 0.06 | 0.08 | 0.05 |
| 6.2.7 Cascades | 11 | 159 | 0.56 | 0.57 | 0.55 | 0.53 |
| 6.2.8 Eastern Cascades Slopes and Foothills | 14 | 317 | 0.65 | 0.65 | 0.54 | 0.23 |
| 6.2.9 Blue Mountains | 10 | 204 | 0.74 | 0.75 | 0.73 | 0.71 |
| 6.2.10 Middle Rockies | 20 | 602 | 0.78 | 0.77 | 0.78 | 0.45 |
| 6.2.12 Sierra Nevada | 46 | 925 | 0.64 | 0.63 | 0.60 | 0.38 |
| 6.2.13 Wasatch and Uinta Mountains | 7 | 228 | 0.91 | 0.89 | 0.87 | 0.59 |
| 6.2.14 Southern Rockies | 64 | 1603 | 0.64 | 0.62 | 0.63 | 0.18 |
| 6.2.15 Idaho Batholith | 5 | 107 | 0.64 | 0.63 | 0.63 | 0.50 |
| 7.0 Marine West Coast Forest | 6 | 81 | 0.53 | 0.49 | 0.51 | 0.40 |
| 7.1 Marine West Coast Forest | 6 | 81 | 0.53 | 0.48 | 0.51 | 0.39 |
| 8.0 Eastern Temperate Forests | 97 | 1980 | 0.82 | 0.80 | 0.82 | 0.17 |
| 8.1 Mixed Wood Plains | 13 | 298 | 0.83 | 0.82 | 0.81 | 0.27 |
| 8.1.3 Northern Appalachian Plateau and Uplands | 4 | 107 | 0.86 | 0.86 | 0.86 | 0.41 |
| 8.1.7 Northeastern Coastal Zone | 3 | 95 | 0.83 | 0.83 | 0.83 | 0.59 |
| 8.3 Southeastern USA Plains | 22 | 478 | 0.83 | 0.82 | 0.83 | 0.63 |
| 8.3.1 Northern Piedmont | 4 | 77 | 0.94 | 0.94 | 0.94 | 0.87 |
| 8.3.3 Interior Plateau | 4 | 96 | 0.73 | 0.73 | 0.73 | 0.38 |
| 8.3.4 Piedmont | 5 | 150 | 0.53 | 0.53 | 0.51 | 0.52 |
| 8.3.8 East Central Texas Plains | 4 | 81 | 0.41 | 0.39 | 0.37 | 0.35 |
| 8.4 Ozark, Ouachita-Appalachian Forests | 53 | 1084 | 0.81 | 0.80 | 0.80 | 0.01 |
| 8.4.1 Ridge and Valley | 14 | 257 | 0.46 | 0.45 | 0.46 | 0.03 |
| 8.4.4 Blue Ridge | 20 | 479 | 0.70 | 0.69 | 0.69 | 0.29 |
| 8.4.5 Ozark Highlands | 12 | 261 | 0.95 | 0.94 | 0.95 | 0.39 |
| 9.0 Great Plains | 42 | 805 | 0.58 | 0.52 | 0.56 | 0.13 |
| 9.2 Temperate Prairies | 16 | 213 | 0.84 | 0.80 | 0.76 | 0.10 |
| 9.2.3 Western Corn Belt Plains | 12 | 166 | 0.84 | 0.84 | 0.77 | 0.09 |
| 9.3 West Central Semi-Arid Prairies | 4 | 88 | 0.71 | 0.71 | 0.67 | 0.55 |
| 9.4 South Central Semi-Arid Prairies | 22 | 504 | 0.44 | 0.42 | 0.41 | 0.20 |
| 9.4.1 High Plains | 6 | 128 | 0.12 | 0.11 | 0.10 | 0.05 |
| 9.4.2 Central Great Plains | 5 | 105 | 0.55 | 0.48 | 0.53 | 0.18 |
| 9.4.3 Southwestern Tablelands | 5 | 138 | 0.28 | 0.28 | 0.27 | 0.09 |
| 9.4.5 Cross Timbers | 6 | 133 | 0.58 | 0.58 | 0.58 | 0.33 |
| 10.0 North American Deserts | 23 | 554 | 0.78 | 0.76 | 0.78 | 0.71 |
| 10.1 Cold Deserts | 19 | 481 | 0.84 | 0.81 | 0.83 | 0.73 |

| | | | | | | |
|---|---|---|---|---|---|---|
| 10.1.4 Wyoming Basin | 5 | 136 | 0.87 | 0.86 | 0.86 | 0.81 |
| 10.1.5 Central Basin and Range | 4 | 76 | 0.91 | 0.90 | 0.90 | 0.88 |
| 10.1.6 Colorado Plateaus | 6 | 175 | 0.60 | 0.56 | 0.56 | 0.06 |
| 10.1.7 Arizona/New Mexico Plateau | 3 | 83 | 0.48 | 0.45 | 0.49 | 0.43 |
| 11.0 Mediterranean California | 12 | 277 | 0.64 | 0.64 | 0.64 | 0.48 |
| 11.1 Mediterranean California | 12 | 277 | 0.64 | 0.63 | 0.64 | 0.48 |
| 11.1.1 California Coastal Sage, Chaparral, and Oak Woodlands | 8 | 196 | 0.63 | 0.62 | 0.63 | 0.48 |
| 11.1.3 Southern and Baja California Pine-Oak Mountains | 4 | 81 | 0.55 | 0.54 | 0.55 | 0.52 |
| 12.0 Southern Semi-Arid Highlands | 21 | 393 | 0.50 | 0.50 | 0.47 | 0.26 |
| 12.1 Western Sierra Madre Piedmont | 21 | 393 | 0.51 | 0.49 | 0.48 | 0.27 |
| 12.1.1 Madrean Archipielago | 21 | 393 | 0.50 | 0.50 | 0.47 | 0.27 |
| 13.0 Temperate Sierras | 27 | 443 | 0.66 | 0.64 | 0.62 | 0.43 |
| 13.1 Upper Gila Mountains | 27 | 443 | 0.66 | 0.65 | 0.63 | 0.43 |
| 13.1.1 Arizona/New Mexico Mountains | 27 | 443 | 0.66 | 0.65 | 0.63 | 0.43 |

**Table A6.** Variance explained ($r^2$) by ecoregion RF models of relative stress (based on out-of-bag observations) for the four model experiments.

| | | | $r^2$ | | | |
|---|---|---|---|---|---|---|
| Ecoregion | Sites | n | TSC | TC | SC | C |
| 5.0 Northern Forests | 56 | 1353 | 0.10 | 0.10 | 0.10 | 0.09 |
| 5.2 Mixed Wood Shield | 19 | 399 | 0.11 | 0.11 | 0.10 | 0.07 |
| 5.2.1 Northern Lakes and Forests | 19 | 399 | 0.11 | 0.11 | 0.10 | 0.07 |
| 5.3 Atlantic Highlands | 37 | 954 | 0.09 | 0.09 | 0.09 | 0.08 |
| 5.3.1 Northern Appalachians and Atlantic Maritime Highlands | 31 | 867 | 0.08 | 0.08 | 0.08 | 0.08 |
| 5.3.3 North Central Appalachians | 6 | 87 | 0.05 | 0.04 | 0.06 | 0.04 |
| 6.0 Northwestern Forested Mountains | 457 | 10876 | 0.32 | 0.31 | 0.30 | 0.28 |
| 6.2 Western Cordillera | 457 | 10876 | 0.32 | 0.31 | 0.30 | 0.28 |
| 6.2.3 Columbia Mountains/Northern Rockies | 7 | 212 | 0.14 | 0.12 | 0.13 | 0.14 |
| 6.2.4 Canadian Rockies | 6 | 183 | 0.01 | 0.01 | 0.01 | 0.00 |
| 6.2.5 North Cascades | 53 | 1012 | 0.38 | 0.37 | 0.38 | 0.36 |
| 6.2.7 Cascades | 43 | 872 | 0.37 | 0.38 | 0.38 | 0.37 |
| 6.2.8 Eastern Cascades Slopes and Foothills | 32 | 699 | 0.27 | 0.26 | 0.26 | 0.25 |
| 6.2.9 Blue Mountains | 21 | 495 | 0.42 | 0.42 | 0.41 | 0.42 |
| 6.2.10 Middle Rockies | 58 | 1708 | 0.26 | 0.26 | 0.24 | 0.23 |
| 6.2.11 Klamath Mountains | 10 | 199 | 0.39 | 0.35 | 0.39 | 0.34 |
| 6.2.12 Sierra Nevada | 81 | 1794 | 0.34 | 0.33 | 0.34 | 0.32 |
| 6.2.13 Wasatch and Uinta Mountains | 20 | 661 | 0.35 | 0.34 | 0.34 | 0.30 |
| 6.2.14 Southern Rockies | 118 | 2860 | 0.37 | 0.35 | 0.34 | 0.31 |
| 6.2.15 Idaho Batholith | 8 | 181 | 0.05 | 0.06 | 0.05 | 0.08 |
| 7.0 Marine West Coast Forest | 14 | 255 | 0.29 | 0.28 | 0.28 | 0.27 |
| 7.1 Marine West Coast Forest | 14 | 255 | 0.28 | 0.28 | 0.29 | 0.26 |
| 7.1.7 Strait of Georgia/Puget Lowland | 5 | 87 | 0.19 | 0.18 | 0.18 | 0.21 |
| 7.1.8 Coastal Range | 9 | 168 | 0.30 | 0.29 | 0.29 | 0.29 |
| 8.0 Eastern Temperate Forests | 297 | 6837 | 0.23 | 0.23 | 0.23 | 0.21 |
| 8.1 Mixed Wood Plains | 37 | 868 | 0.17 | 0.17 | 0.17 | 0.17 |
| 8.1.1 Eastern Great Lakes and Hudson Lowlands | 4 | 139 | 0.14 | 0.16 | 0.16 | 0.18 |
| 8.1.3 Northern Appalachian Plateau and Uplands | 5 | 141 | 0.18 | 0.18 | 0.18 | 0.16 |
| 8.1.4 North Central Hardwood Forests | 8 | 222 | 0.24 | 0.23 | 0.23 | 0.25 |
| 8.1.7 Northeastern Coastal Zone | 4 | 112 | 0.14 | 0.12 | 0.15 | 0.13 |
| 8.1.8 Maine/New Brunswick Plains and Hills | 9 | 166 | 0.05 | 0.03 | 0.03 | 0.03 |
| 8.2 Central USA Plains | 8 | 105 | 0.37 | 0.37 | 0.35 | 0.32 |
| 8.2.3 Central Corn Belt Plains | 7 | 90 | 0.35 | 0.34 | 0.31 | 0.28 |
| 8.3 Southeastern USA Plains | 64 | 1441 | 0.35 | 0.35 | 0.35 | 0.34 |
| 8.3.1 Northern Piedmont | 7 | 148 | 0.44 | 0.46 | 0.48 | 0.47 |
| 8.3.2 Interior River Valleys and Hills | 9 | 163 | 0.24 | 0.25 | 0.24 | 0.21 |
| 8.3.3 Interior Plateau | 5 | 131 | 0.51 | 0.52 | 0.52 | 0.54 |
| 8.3.4 Piedmont | 11 | 292 | 0.50 | 0.49 | 0.49 | 0.48 |
| 8.3.5 Southeastern Plains | 21 | 506 | 0.30 | 0.31 | 0.29 | 0.28 |
| 8.3.7 South Central Plains | 5 | 76 | 0.13 | 0.13 | 0.11 | 0.13 |
| 8.3.8 East Central Texas Plains | 6 | 125 | 0.59 | 0.56 | 0.57 | 0.59 |
| 8.4 Ozark, Ouachita-Appalachian Forests | 162 | 3914 | 0.19 | 0.19 | 0.19 | 0.18 |
| 8.4.1 Ridge and Valley | 34 | 805 | 0.09 | 0.10 | 0.09 | 0.08 |

| | | | | | | |
|---|---|---|---|---|---|---|
| 8.4.2 Central Appalachians | 5 | 173 | 0.08 | 0.07 | 0.08 | 0.07 |
| 8.4.3 Western Allegheny Plateau | 3 | 87 | 0.06 | 0.05 | 0.03 | 0.04 |
| 8.4.4 Blue Ridge | 38 | 962 | 0.16 | 0.16 | 0.17 | 0.15 |
| 8.4.5 Ozark Highlands | 53 | 1216 | 0.34 | 0.34 | 0.33 | 0.33 |
| 8.4.6 Boston Mountains | 5 | 116 | 0.07 | 0.08 | 0.09 | 0.08 |
| 8.4.7 Arkansas Valley | 4 | 122 | 0.52 | 0.56 | 0.55 | 0.56 |
| 8.4.8 Ouachita Mountains | 15 | 337 | 0.23 | 0.23 | 0.23 | 0.24 |
| 8.4.9 Southwestern Appalachians | 5 | 96 | 0.12 | 0.12 | 0.11 | 0.11 |
| 8.5 Mississippi Alluvial and Southeast USA Coastal Plains | 26 | 509 | 0.21 | 0.22 | 0.20 | 0.21 |
| 8.5.1 Middle Atlantic Coastal Plain | 7 | 127 | 0.15 | 0.15 | 0.16 | 0.19 |
| 8.5.2 Mississippi Alluvial Plain | 9 | 137 | 0.20 | 0.20 | 0.18 | 0.20 |
| 8.5.3 Southern Coastal Plain | 10 | 245 | 0.19 | 0.17 | 0.17 | 0.15 |
| 9.0 Great Plains | 96 | 2367 | 0.33 | 0.33 | 0.32 | 0.30 |
| 9.2 Temperate Prairies | 34 | 792 | 0.47 | 0.48 | 0.48 | 0.48 |
| 9.2.2 Lake Manitoba and Lake Agassiz Plain | 11 | 395 | 0.55 | 0.55 | 0.55 | 0.55 |
| 9.2.3 Western Corn Belt Plains | 12 | 166 | 0.58 | 0.59 | 0.59 | 0.60 |
| 9.2.4 Central Irregular Plains | 8 | 169 | 0.26 | 0.27 | 0.25 | 0.32 |
| 9.3 West Central Semi-Arid Prairies | 14 | 360 | 0.38 | 0.37 | 0.38 | 0.38 |
| 9.3.3 Northwestern Great Plains | 12 | 305 | 0.36 | 0.35 | 0.36 | 0.36 |
| 9.4 South Central Semi-Arid Prairies | 47 | 1176 | 0.27 | 0.27 | 0.26 | 0.24 |
| 9.4.1 High Plains | 8 | 188 | 0.20 | 0.20 | 0.21 | 0.21 |
| 9.4.2 Central Great Plains | 6 | 117 | 0.47 | 0.46 | 0.47 | 0.45 |
| 9.4.3 Southwestern Tablelands | 15 | 380 | 0.22 | 0.23 | 0.23 | 0.22 |
| 9.4.5 Cross Timbers | 13 | 340 | 0.47 | 0.48 | 0.48 | 0.47 |
| 9.4.6 Edwards Plateau | 4 | 115 | 0.15 | 0.15 | 0.17 | 0.10 |
| 10.0 North American Deserts | 88 | 2107 | 0.45 | 0.44 | 0.44 | 0.41 |
| 10.1 Cold Deserts | 80 | 1969 | 0.48 | 0.47 | 0.47 | 0.43 |
| 10.1.3 Northern Basin and Range | 13 | 309 | 0.60 | 0.61 | 0.61 | 0.60 |
| 10.1.4 Wyoming Basin | 7 | 197 | 0.38 | 0.36 | 0.37 | 0.29 |
| 10.1.5 Central Basin and Range | 31 | 606 | 0.29 | 0.28 | 0.29 | 0.25 |
| 10.1.6 Colorado Plateaus | 24 | 733 | 0.53 | 0.53 | 0.51 | 0.47 |
| 10.1.7 Arizona/New Mexico Plateau | 4 | 108 | 0.52 | 0.53 | 0.54 | 0.55 |
| 10.2 Warm Deserts | 8 | 138 | 0.22 | 0.23 | 0.23 | 0.22 |
| 10.2.4 Chihuahuan Desert | 6 | 113 | 0.24 | 0.27 | 0.26 | 0.25 |
| 11.0 Mediterranean California | 62 | 1624 | 0.51 | 0.49 | 0.51 | 0.48 |
| 11.1 Mediterranean California | 62 | 1624 | 0.51 | 0.49 | 0.50 | 0.49 |
| 11.1.1 California Coastal Sage, Chaparral, and Oak Woodlands | 37 | 1118 | 0.49 | 0.46 | 0.49 | 0.44 |
| 11.1.3 Southern and Baja California Pine-Oak Mountains | 23 | 438 | 0.59 | 0.58 | 0.59 | 0.59 |
| 12.0 Southern Semi-Arid Highlands | 30 | 551 | 0.44 | 0.44 | 0.43 | 0.43 |
| 12.1 Western Sierra Madre Piedmont | 30 | 551 | 0.43 | 0.43 | 0.43 | 0.43 |
| 12.1.1 Madrean Archipielago | 30 | 551 | 0.44 | 0.43 | 0.43 | 0.43 |
| 13.0 Temperate Sierras | 37 | 635 | 0.51 | 0.49 | 0.49 | 0.45 |
| 13.1 Upper Gila Mountains | 37 | 635 | 0.51 | 0.48 | 0.50 | 0.45 |
| 13.1.1 Arizona/New Mexico Mountains | 37 | 635 | 0.51 | 0.49 | 0.49 | 0.45 |

## APPENDIX 3: SUPPLEMENTAL TEXT

**Text A1.** In CooRecorder, BI was extracted from rectangular windows surrounding tree-ring latewood, and we adjusted the size of the windows (width, depth, and offset) as well as the percentage of latewood that was used for calculating BI (%blue) following *Rydval et al.* [2014]. We tested several parameter sets for a subset of cores and compared the effective mean inter-series correlations ($RBAR_{eff}$) from the different sets (Table A2). Variation of window width, depth, and %blue all had significant effects on series statistics, with an optimal width-offset-depth-%blue parameter set of 100-5-10-30. Raw BI from each core were inverted following *Rydval et al.* [2014] and *Wilson et al.* [2014] and then plotted to identify sharp transitions early in the BI series or other graphical forms that suggested the series is not suitable for further use. Each inverted BI series was detrended using linear and quadratic models (with no restrictions on the sign of the slope), and the Akaike information criterion [*Akaike*, 1974] was used to select the best fit between these two models. After checking the selected regression models for negative fitted values, we obtained standardized and detrended indices by dividing the fitted curves for each core into the inverted BI series. Site-level residual chronologies were then formed following the same procedure used for ring width series. All sites except site 1 (EPS=0.79) achieved EPS≥0.82 (Table A1).

**Text A2.** The composite-plus-scale (CPS) tests performed in Tables 1 & 2 required six steps:

1) Principal components analysis was performed separately for each tree-ring metric (TRW, EW, LWadj, and BI) with the six site-level chronologies as variables.
2) PCs 1 & 2 of each metric were transformed to z-scores, resulting in a total of eight PC time-series (two each for four metrics).
3) The Pearson correlation coefficient (R) was calculated between each z-scored PC time-series and the target climate variable ($P_{cool}$ or $P_{warm}$; rows 1-4 of the PC1 and PC2 columns in Tables 1 & 2).

4) For each target climate variable, 13 possible PC composites were formed (the COMBO column and rows 5-7 of the PC1 and PC2 columns in Tables 1 & 2) by taking a weighted average of different combinations of PC time-series, using $R^2$ as the weight [*McCarroll et al.*, 2003, 2011] and multiplying by the sign of the correlation coefficient so that each PC time series in the composite has a positive relationship with the target climate variable [*Wilson et al.*, 2010].
5) For the COMBO composites, the weighted average (composite) of tree-ring PCs was scaled to match the mean and variance of the target climate variable.
6) The effective correlation, variance-scaled $R^2$, and extreme value capture (EVC) statistics [*McCarroll et al.*, 2011, 2015] were calculated between the scaled tree-ring composites (predicted) and the instrumental target climate (observed).

For example, the EW+$LW_{adj}$ COMBO prediction of $P_{warm}$ (Table 2) was formed by performing a PCA on the six site-level EW chronologies and a separate PCA on the six site-level $LW_{adj}$ chronologies. The first two PCs from each PCA (a total of four PC time-series) were transformed to z-scores, and then the four transformed PC time-series were composited with a weighted average, with the weights determined by the $R^2$ between each PC and the observed $P_{warm}$ while retaining the sign of the correlation coefficient:

$$COMPOSITE = 0.18*PC1(EW) - 0.08*PC2(EW) + 0.28*PC1(LW_{adj}) - 0.06*PC2(LW_{adj})$$

$P_{warm}$ was then predicted by scaling this composite to match the mean and variance of the observed $P_{warm}$ during the study period (1913-2012).

## REFERENCES


Akaike, H. (1974), A new look at the statistical model identification, *IEEE Trans. Automat. Contr.*, *19*(6), 716–723.

Allakhverdiev, S. I., V. D. Kreslavski, V. V. Klimov, D. A. Los, R. Carpentier, and P. Mohanty (2008), Heat stress: an overview of molecular responses in photosynthesis, *Photosynth. Res.*, *98*(1–3), 541–550, doi:10.1007/s11120-008-9331-0.

Allen, C. D., D. D. Breshears, and N. G. McDowell (2015), On underestimation of global vulnerability to tree mortality and forest die-off from hotter drought in the Anthropocene, *Ecosphere*, *6*(8), 129, doi:10.1890/ES15-00203.1.

Allen, R. G., L. S. Pereira, D. Raes, and M. Smith (1998), Crop evapotranspiration-Guidelines for computing crop water requirements-FAO Irrigation and drainage paper 56, *FAO, Rome*, *300*(9), D05109.

Angert, A., S. Biraud, C. Bonfils, C. C. Henning, W. Buermann, J. Pinzon, C. J. Tucker, and I. Fung (2005), Drier summers cancel out the CO2 uptake enhancement induced by warmer springs, *Proc. Natl. Acad. Sci. U. S. A.*, *102*(31), 10823–10827, doi:10.1073/pnas.0501647102.

Archer, C. L., and K. Caldeira (2008), Historical trends in the jet streams, *Geophys. Res. Lett.*, *35*, L08803, doi:10.1029/2008GL033614.

Archibold, O. W. (1995), *Ecology of World Vegetation*, Chapman & Hall, London, UK.

Ashfaq, M., S. Ghosh, S.-C. Kao, L. C. Bowling, P. Mote, D. Touma, S. a. Rauscher, and N. S. Diffenbaugh (2013), Near-term acceleration of hydroclimatic change in the western U.S., *J. Geophys. Res. Atmos.*, *118*(19), 10,676-10,693, doi:10.1002/jgrd.50816.

Babst, F. et al. (2014), A tree-ring perspective on the terrestrial carbon cycle, *Oecologia*, 307–322, doi:10.1007/s00442-014-3031-6.

Ballantyne, A. et al. (2017), Accelerating net terrestrial carbon uptake during the warming hiatus due to reduced respiration, *Nat. Clim. Chang.*, (January), doi:10.1038/nclimate3204.

Barnes, M. L., M. S. Moran, R. L. Scott, T. E. Kolb, G. E. Ponce-Campos, D. J. P. Moore, M. A. Ross, B. Mitra, and S. Dore (2016), Vegetation productivity responds to sub-annual climate conditions across semiarid biomes, *Ecosphere*, *7*(5), 1–21, doi:10.1002/ecs2.1339.

Barnett, T. P., J. C. Adam, and D. P. Lettenmaier (2005), Potential impacts of a warming climate on water availability in snow-dominated regions, *Nature*, *438*(7066), 303–9, doi:10.1038/nature04141.

Barnett, T. P. et al. (2008), Human-induced changes in the hydrology of the western United States, *Science*, *319*, 1080–1083.

Beck, P. S. A., L. Andreu-Hayles, R. D'Arrigo, K. J. Anchukaitis, C. J. Tucker, J. E. Pinzón, and S. J. Goetz (2013), A large-scale coherent signal of canopy status in maximum

latewood density of tree rings at arctic treeline in North America, *Glob. Planet. Change*, *100*, 109–118, doi:10.1016/j.gloplacha.2012.10.005.

Berner, L. T., and B. E. Law (2015), Water limitations on forest carbon cycling and conifer traits along a steep climatic gradient in the Cascade Mountains, Oregon, *Biogeosciences*, *12*(22), 6617–6635, doi:10.5194/bg-12-6617-2015.

Beven, K. J., and M. J. Kirkby (1979), A physically based, variable contributing area model of basin hydrology, *Hydrol. Sci. J.*, *24*, 43–69.

Boisvenue, C., and S. W. Running (2006), Impacts of climate change on natural forest productivity - evidence since the middle of the 20th century, *Glob. Chang. Biol.*, *12*(5), 862–882, doi:10.1111/j.1365-2486.2006.01134.x.

Boisvenue, C., and S. W. Running (2010), Simulations show decreasing carbon stocks and potential for carbon emissions in Rocky Mountain forests over the next century, *Ecol. Appl.*, *20*(5), 1302–1319.

Botkin, D. B., J. F. Janak, and J. R. Wallis (1972), Some ecological consequences of a computer model of forest growth, *J. Ecol.*, *60*(3), 849–872.

Bowman, D. M. J. S. et al. (2009), Fire in the Earth System, *Science*, *324*(5926), 481–484, doi:10.1126/science.1163886.

Bowman, D. M. J. S., R. J. W. Brienen, E. Gloor, O. L. Phillips, and L. D. Prior (2013), Detecting trends in tree growth: not so simple, *Trends Plant Sci.*, *18*(1), 11–17, doi:10.1016/j.tplants.2012.08.005.

Breiman, L. (2001), Random forests, *Mach. Learn.*, *45*, 5–32.

Brienen, R. J. W., E. Gloor, and P. A. Zuidema (2012), Detecting evidence for CO2 fertilization from tree ring studies: The potential role of sampling biases, *Global Biogeochem. Cycles*, *26*(1), doi:10.1029/2011GB004143.

Briffa, K. R., T. J. Osborn, F. H. Schweingruber, I. C. Harris, P. D. Jones, S. G. Shiyatov, and E. A. Vaganov (2001), Low-frequency temperature variations from a northern tree ring density network, *J. Geophys. Res.*, *106*(D3), 2929–2941.

Briffa, K. R., T. J. Osborn, and F. H. Schweingruber (2004), Large-scale temperature inferences from tree rings: a review, *Glob. Planet. Change*, *40*(1–2), 11–26, doi:10.1016/S0921-8181(03)00095-X.

Brzostek, E. R., D. Dragoni, H. P. Schmid, A. F. Rahman, D. Sims, C. A. Wayson, D. J. Johnson, and R. P. Phillips (2014), Chronic water stress reduces tree growth and the carbon sink of deciduous hardwood forests, *Glob. Chang. Biol.*, *20*(8), 2531–2539, doi:10.1111/gcb.12528.

Bunn, A. G. (2008), A dendrochronology program library in R (dplR), *Dendrochronologia*, *26*(2), 115–124, doi:10.1016/j.dendro.2008.01.002.

Bunn, A. G., M. K. Hughes, A. V. Kirdyanov, M. Losleben, V. V. Shishov, L. T. Berner, A. Oltchev, and E. A. Vaganov (2013), Comparing forest measurements from tree rings and

a space-based index of vegetation activity in Siberia, *Environ. Res. Lett.*, *8*(3), 35034, doi:10.1088/1748-9326/8/3/035034.

Cai, W., W. Yuan, S. Liang, S. Liu, W. Dong, Y. Chen, D. Liu, and H. Zhang (2014), Large Differences in Terrestrial Vegetation Production Derived from Satellite-Based Light Use Efficiency Models, *Remote Sens.*, *6*(9), 8945–8965, doi:10.3390/rs6098945.

Campbell, G. S., and J. M. Norman (1998), *An Introduction to Environmental Biophysics*, 2nd ed., Springer-Verlag, New York, NY.

Campbell, R., D. McCarroll, N. J. Loader, H. Grudd, I. Robertson, and R. Jalkanen (2007), Blue intensity in Pinus sylvestris tree-rings: developing a new palaeoclimate proxy, *The Holocene*, *17*(6), 821–828, doi:10.1177/0959683607080523.

Campbell, R., D. McCarroll, I. Robertson, N. J. Loader, H. Grudd, and B. Gunnarson (2011), Blue intensity in Pinus sylvestris tree rings: a manual for a new palaeoclimate proxy, *Tree-Ring Res.*, *67*(2), 127–134.

Cayan, D. R., E. P. Maurer, M. D. Dettinger, M. Tyree, and K. Hayhoe (2008), Climate change scenarios for the California region, *Clim. Change*, *87*(S1), 21–42, doi:10.1007/s10584-007-9377-6.

Chang, E. K. M. (2003), Midwinter Suppression of the Pacific Storm Track Activity as Seen in Aircraft Observations, *J. Atmos. Sci.*, *60*(11), 1345–1358, doi:10.1175/1520-0469(2003)60<1345:MSOTPS>2.0.CO;2.

Chang, E. K. M., and Y. Fu (2002), Interdecadal variations in Northern Hemisphere winter storm track intensity, *J. Clim.*, *15*(6), 642–658, doi:10.1175/1520-0442(2002)015<0642:IVINHW>2.0.CO;2.

Chang, E. K. M., S. Lee, and K. L. Swanson (2002), Storm track dynamics, *J. Clim.*, *15*(16), 2163–2183, doi:10.1175/1520-0442(2002)015<02163:STD>2.0.CO;2.

Chapin, F. S., P. A. Matson, and P. M. Vitousek (2011), *Principles of Terrestrial Ecosystem Ecology*, 2nd ed., Springer, New York, NY.

Cherubini, P., M. Dobbertin, and J. L. Innes (1998), Potential sampling bias in long-term forest growth trends reconstructed from tree rings: a case study from the Italian Alps, *For. Ecol. Manage.*, *109*, 103–118.

Ciais, P. et al. (2013), Carbon and Other Biogeochemical Cycles, in *Climate Change 2013: The Physical Science Basis. Contribution of Working Group I to the Fifth Assessment Report of the Intergovernmental Panel on Climate Change*, edited by T. F. Stocker, D. Qin, G.-K. Plattner, M. Tignor, S. K. Allen, J. Boschung, A. Nauels, Y. Xia, V. Bex, and P. M. Midgley, pp. 465–570, Cambridge University Press, Cambridge, UK and New York, NY.

Collins, M. et al. (2013), Long-term Climate Change: Projections, Commitments and Irreversibility, in *Climate Change 2013: The Physical Science Basis. Contribution of Working Group I to the Fifth Assessment Report of the Intergovernmental Panel on Climate Change*, edited by T. F. Stocker, D. Qin, G.-K. Plattner, M. Tignor, S. K. Allen,

J. Boschung, A. Nauels, Y. Xia, V. Bex, and P. M. Midgley, pp. 1029–1136, Cambridge University Press, Cambridge, UK.

Compo, G. P. et al. (2011), The twentieth century reanalysis project, *Q. J. R. Meteorol. Soc.*, *137*, 1–28, doi:10.1002/qj.776.

Cook, B. I., J. E. Smerdon, R. Seager, and S. Coats (2014), Global warming and 21st century drying, *Clim. Dyn.*, doi:10.1007/s00382-014-2075-y.

Cook, B. I., T. R. Ault, and J. E. Smerdon (2015), Unprecedented 21st century drought risk in the American Southwest and Central Plains, *Sci. Adv.*, *1*, e1400082, doi:10.1126/sciadv.1400082.

Cook, E. R. (1985), A time series analysis approach to tree-ring standardization, Ph.D. Dissertation, University of Arizona, Tuscon, Arizona, USA.

Cook, E. R., and K. Peters (1981), The smoothing spline: a new approach to standardizing forest interior tree-ring width series for dendroclimatic studies, *Tree-Ring Bull.*, *41*, 45–53.

Cook, E. R., D. M. Meko, D. W. Stahle, and M. K. Cleaveland (1999), Drought reconstructions for the continental United States, *J. Clim.*, *12*, 1145–1162.

Cook, E. R., C. A. Woodhouse, C. M. Eakin, D. M. Meko, and D. W. Stahle (2004), Long-term aridity changes in the western United States., *Science*, *306*, 1015–1018, doi:10.1126/science.1102586.

Crawford, C. J., D. Griffin, and K. F. Kipfmueller (2015), Capturing season-specific precipitation signals in the northern Rocky Mountains, USA, using earlywood and latewood tree rings, *J. Geophys. Res. Biogeosciences*, *120*, 428–440, doi:10.1002/2014JG002740.

Crowley, T. J., and T. S. Lowery (2000), Warm was the medieval warm period?, *Ambio*, *29*(1), 51–54.

Cutler, D. R., T. C. Edwards, Jr., K. H. Beard, A. Cutler, J. G. Hess, and J. T. Lawler (2007), Random forests for classification in ecology, *Ecology*, *88*(11), 2783–2792.

Daly, C., M. Halbleib, J. I. Smith, W. P. Gibson, M. K. Doggett, G. H. Taylor, J. Curtis, and P. P. Pasteris (2008), Physiographically sensitive mapping of climatological temperature and precipitation across the conterminous United States, *Int. J. Climatol.*, *28*, 2031–2064, doi:10.1002/joc.

Dannenberg, M. P., and E. K. Wise (2016), Seasonal climate signals from multiple tree-ring metrics: a case study of Pinus ponderosa in the upper Columbia River basin, *J. Geophys. Res. Biogeosciences*, *121*, 1178–1189, doi:10.1002/2015JG003155.

Dannenberg, M. P., C. Song, T. Hwang, and E. K. Wise (2015), Empirical evidence of El Niño-Southern Oscillation influence on land surface phenology and productivity in the western United States, *Remote Sens. Environ.*, *159*, 167–180, doi:10.1016/j.rse.2014.11.026.

Dennison, P. E., S. C. Brewer, J. D. Arnold, and M. A. Moritz (2014), Large wildfire trends in the western United States, 1984-2011, *Geophys. Res. Lett.*, *41*(8), 2928–2933, doi:10.1002/2014GL059576.

Eidenshink, J., B. Schwind, K. Brewer, Z.-L. Zhu, B. Quayle, and S. Howard (2007), A project for monitoring trends in fire severity, *Fire Ecol.*, *3*(1), 3–21.

Emanuel, R. E., H. E. Epstein, B. L. McGlynn, D. L. Welsch, D. J. Muth, and P. D'Odorico (2010), Spatial and temporal controls on watershed ecohydrology in the northern Rocky Mountains, *Water Resour. Res.*, *46*, W11553, doi:10.1029/2009WR008890.

Emanuel, R. E., D. A. Riveros-Iregui, B. L. McGlynn, and H. E. Epstein (2011), On the spatial heterogeneity of net ecosystem productivity in complex landscapes, *Ecosphere*, *2*(7), 1–13, doi:10.1890/ES11-00074.1.

Emile-Geay, J., K. M. Cobb, M. E. Mann, and A. T. Wittenberg (2013), Estimating Central Equatorial Pacific SST Variability over the Past Millennium. Part I: Methodology and Validation, *J. Clim.*, *26*(7), 2302–2328, doi:10.1175/JCLI-D-11-00510.1.

Esper, J., E. R. Cook, and F. H. Schweingruber (2002), Low-frequency signals in long tree-ring chronologies for reconstructing past temperature variability., *Science*, *295*, 2250–2253, doi:10.1126/science.1066208.

Fisher, J., J. Mustard, and M. Vadeboncoeur (2006), Green leaf phenology at Landsat resolution: Scaling from the field to the satellite, *Remote Sens. Environ.*, *100*(2), 265–279, doi:10.1016/j.rse.2005.10.022.

Flexas, J. (2002), Drought-inhibition of photosynthesis in C3 plants: stomatal and non-stomatal limitations revisited, *Ann. Bot.*, *89*(2), 183–189, doi:10.1093/aob/mcf027.

Fritts, H. C. (1976), *Tree Rings and Climate*, Academic Press, New York.

Garbulsky, M. F., J. Peñuelas, D. Papale, J. Ardö, M. L. Goulden, G. Kiely, A. D. Richardson, E. Rotenberg, E. M. Veenendaal, and I. Filella (2010), Patterns and controls of the variability of radiation use efficiency and primary productivity across terrestrial ecosystems, *Glob. Ecol. Biogeogr.*, *19*(2), 253–267, doi:10.1111/j.1466-8238.2009.00504.x.

Gebremichael, M., and A. P. Barros (2006), Evaluation of MODIS Gross Primary Productivity (GPP) in tropical monsoon regions, *Remote Sens. Environ.*, *100*(2), 150–166, doi:10.1016/j.rse.2005.10.009.

Gislason, P. O., J. A. Benediktsson, and J. R. Sveinsson (2006), Random Forests for land cover classification, *Pattern Recognit. Lett.*, *27*(4), 294–300, doi:10.1016/j.patrec.2005.08.011.

Graumlich, L. J. (1987), Precipitation variation in the Pacific Northwest (1675-1975) as reconstructed from tree rings, *Ann. Assoc. Am. Geogr.*, *77*(1), 19–29.

Graumlich, L. J., L. B. Brubaker, and C. C. Grier (1989), Long-term trends in forest net primary productivity: Cascade Mountains, Washington, *Ecology*, *70*(2), 405–410.

Griffin, D., D. M. Meko, R. Touchan, S. W. Leavitt, and C. A. Woodhouse (2011), Latewood chronology development for summer-moisture reconstruction in the US Southwest, *Tree-Ring Res.*, *67*(2), 87–101.

Griffin, D., C. A. Woodhouse, D. M. Meko, D. W. Stahle, H. L. Faulstich, C. Carrillo, R. Touchan, C. L. Castro, and S. W. Leavitt (2013), North American monsoon precipitation reconstructed from tree-ring latewood, *Geophys. Res. Lett.*, *40*(5), 954–958, doi:10.1002/grl.50184.

Grissino-Mayer, H. D. (2001), Evaluating crossdating accuracy: A manual and tutorial for the computer program COFECHA, *Tree-Ring Res.*, *57*(2), 205–221.

Grissino-Mayer, H. D., and H. C. Fritts (1997), The International Tree-Ring Data Bank: an enhanced global database serving the global scientific community, *The Holocene*, *7*(2), 235–238, doi:10.1177/095968369700700212.

Hamlet, A. F., and D. P. Lettenmaier (1999), Effects of climate change on hydrology and water resources in the Columbia River Basin, *J. Am. Water Resour. Assoc.*, *35*(6), 1597–1623.

Hardin, J. W., D. J. Leopold, and F. M. White (2001), *Harlow and Harrar's Textbook of Dendrology*, 9th ed., McGraw-Hill, New York, NY, NY.

Harris, I., P. D. Jones, T. J. Osborn, and D. H. Lister (2014), Updated high-resolution grids of monthly climatic observations - the CRU TS3.10 Dataset, *Int. J. Climatol.*, *34*(3), 623–642, doi:10.1002/joc.3711.

Heinsch, F. A. et al. (2006), Evaluation of remote sensing based terrestrial productivity from MODIS using regional tower eddy flux network observations, *IEEE Trans. Geosci. Remote Sens.*, *44*(7), 1908–1925, doi:10.1109/TGRS.2005.853936.

Holmes, R. L. (1983), Computer-assisted quality control in tree ring dating and measurement, *Tree-Ring Bull.*, *43*, 69–78.

Hornberger, G. M., P. L. Wiberg, J. P. Raffensperger, and P. D'Odorico (2014), *Elements of Physical Hydrology*, JHU Press.

Hu, J., D. J. P. Moore, S. P. Burns, and R. K. Monson (2010), Longer growing seasons lead to less carbon sequestration by a subalpine forest, *Glob. Chang. Biol.*, *16*(2), 771–783, doi:10.1111/j.1365-2486.2009.01967.x.

Hwang, T., S. Kang, J. Kim, Y. Kim, D. Lee, and L. Band (2008), Evaluating drought effect on MODIS Gross Primary Production (GPP) with an eco-hydrological model in the mountainous forest, East Asia, *Glob. Chang. Biol.*, *14*, 1–20, doi:10.1111/j.1365-2486.2008.01556.x.

Hwang, T., C. Song, P. V. Bolstad, and L. E. Band (2011a), Downscaling real-time vegetation dynamics by fusing multi-temporal MODIS and Landsat NDVI in topographically complex terrain, *Remote Sens. Environ.*, *115*(10), 2499–2512, doi:10.1016/j.rse.2011.05.010.

Hwang, T., C. Song, J. M. Vose, and L. E. Band (2011b), Topography-mediated controls on local vegetation phenology estimated from MODIS vegetation index, *Landsc. Ecol.*, *26*(4), 541–556, doi:10.1007/s10980-011-9580-8.

Jiang, X., S. A. Rauscher, T. D. Ringler, D. M. Lawrence, A. P. Williams, C. D. Allen, A. L. Steiner, D. M. Cai, and N. G. McDowell (2013), Projected future changes in vegetation in western North America in the twenty-first century, *J. Clim.*, *26*(11), 3671–3687, doi:10.1175/JCLI-D-12-00430.1.

Jones, P. D. et al. (2009), High-resolution palaeoclimatology of the last millennium: a review of current status and future prospects, *The Holocene*, *19*(1), 3–49.

Kagawa, A., A. Sugimoto, and T. C. Maximov (2006), 13CO2 pulse-labelling of photoassimilates reveals carbon allocation within and between tree rings, *Plant, Cell Environ.*, *29*(8), 1571–1584, doi:10.1111/j.1365-3040.2006.01533.x.

Kanniah, K. D., J. Beringer, L. B. Hutley, N. J. Tapper, and X. Zhu (2009), Evaluation of Collections 4 and 5 of the MODIS Gross Primary Productivity product and algorithm improvement at a tropical savanna site in northern Australia, *Remote Sens. Environ.*, *113*(9), 1808–1822, doi:10.1016/j.rse.2009.04.013.

Kapnick, S., and A. Hall (2012), Causes of recent changes in western North American snowpack, *Clim. Dyn.*, *38*(9–10), 1885–1899, doi:10.1007/s00382-011-1089-y.

Kirdyanov, A. V., K. S. Treydte, A. Nikolaev, G. Helle, and G. H. Schleser (2008), Climate signals in tree-ring width, density and δ13C from larches in Eastern Siberia (Russia), *Chem. Geol.*, *252*(1–2), 31–41, doi:10.1016/j.chemgeo.2008.01.023.

Kirtman, B. et al. (2013), Near-term Climate Change: Projections and Predictability, in *Climate Change 2013: The Physical Science Basis. Contribution of Working Group I to the Fifth Assessment Report of the Intergovernmental Panel on Climate Change*, edited by T. F. Stocker, D. Qin, G.-K. Plattner, M. Tignor, S. K. Allen, J. Boschung, A. Nauels, Y. Xia, V. Bex, and P. M. Midgley, pp. 953–1028, Cambridge University Press, Cambridge, UK.

Knapp, P. A., and P. T. Soulé (2011), Increasing water-use efficiency and age-specific growth responses of old-growth ponderosa pine trees in the Northern Rockies, *Glob. Chang. Biol.*, *17*(1), 631–641, doi:10.1111/j.1365-2486.2010.02209.x.

Knutson, K. C., and D. A. Pyke (2008), Western juniper and ponderosa pine ecotonal climate–growth relationships across landscape gradients in southern Oregon, *Can. J. For. Res.*, *38*, 3021–3032, doi:10.1139/X08-142.

Körner, C., and D. Basler (2010), Phenology under global warming, *Science*, *327*(5972), 1461–2, doi:10.1126/science.1186473.

Kusnierczyk, E. R., and G. J. Ettl (2002), Growth response of ponderosa pine (Pinus ponderosa) to climate in the eastern Cascade Mountains, Washington, U.S.A.: implications for climatic change, *Ecoscience*, *9*(4), 544–551.

Leung, L. R., Y. Qian, X. Bian, W. M. Washington, J. Han, and J. O. Roads (2004), Mid-century ensemble regional climate change scenarios for the western United States, *Clim. Change*, *62*, 75–113.

Leuning, R., H. A. Cleugh, S. J. Zegelin, and D. Hughes (2005), Carbon and water fluxes over a temperate Eucalyptus forest and a tropical wet/dry savanna in Australia: measurements and comparison with MODIS remote sensing estimates, *Agric. For. Meteorol.*, *129*(3–4), 151–173, doi:10.1016/j.agrformet.2004.12.004.

Liang, E., D. Eckstein, and H. Liu (2009), Assessing the recent grassland greening trend in a long-term context based on tree-ring analysis: A case study in North China, *Ecol. Indic.*, *9*(6), 1280–1283, doi:10.1016/j.ecolind.2009.02.007.

Liang, E. Y., X. M. Shao, and J. C. He (2005), Relationships between tree growth and NDVI of grassland in the semi-arid grassland of north China, *Int. J. Remote Sens.*, *26*(13), 2901–2908, doi:10.1080/01431160500056931.

Lilliefors, H. W. (1967), On the Kolmogorov-Smirnov test for normality with mean and variance unknown, *J. Am. Stat. Assoc.*, *62*, 399–402.

Littell, J. S., D. L. Peterson, and M. Tjoelker (2008), Douglas-fir growth in mountain ecosystems: water limits tree growth from stand to region, *Ecol. Monogr.*, *78*(3), 349–368.

Littell, J. S., D. McKenzie, D. L. Peterson, and A. L. Westerling (2009), Climate and wildfire area burned in western U.S. ecoprovinces, 1916-2003, *Ecol. Appl.*, *19*(4), 1003–1021, doi:10.1890/07-1183.1.

Littell, J. S., G. T. Pederson, S. T. Gray, M. Tjoelker, A. F. Hamlet, and C. A. Woodhouse (2016), Reconstructions of Columbia River streamflow from tree-ring chronologies in the Pacific Northwest, USA, *JAWRA J. Am. Water Resour. Assoc.*, *52*(5), 1121–1141, doi:10.1111/1752-1688.12442.

Lo, Y.-H., J. A. Blanco, B. Seely, C. Welham, and J. P. (Hamish) Kimmins (2010), Relationships between climate and tree radial growth in interior British Columbia, Canada, *For. Ecol. Manage.*, *259*(5), 932–942, doi:10.1016/j.foreco.2009.11.033.

Lorenz, D. J., and E. T. DeWeaver (2007), Tropopause height and zonal wind response to global warming in the IPCC scenario integrations, *J. Geophys. Res. Atmos.*, *112*, D10119, doi:10.1029/2006JD008087.

Luce, C. H., J. T. Abatzoglou, and Z. A. Holden (2013), The missing mountain water: slower westerlies decrease orographic enhancement in the Pacific Northwest USA, *Science*, *342*, 1360–1364, doi:10.1126/science.1242335.

Lute, A. C., J. T. Abatzoglou, and K. C. Hegewisch (2015), Projected changes in snowfall extremes and interannual variability of snowfall in the western United States, *Water Resour. Res.*, *51*, 960–972, doi:10.1002/2014WR016267.

Luterbacher, J., D. Dietrich, E. Xoplaki, M. Grosjean, and H. Wanner (2004), European seasonal and annual temperature variability, trends, and extremes since 1500, *Science*, *303*, 1499–1503, doi:10.1126/science.1093877.

Lutz, E. R., A. F. Hamlet, and J. S. Littell (2012), Paleoreconstruction of cool season precipitation and warm season streamflow in the Pacific Northwest with applications to climate change assessments, *Water Resour. Res.*, *48*, W01525, doi:10.1029/2011WR010687.

Mann, M. E., and P. D. Jones (2003), Global surface temperatures over the past two millennia, *Geophys. Res. Lett.*, *30*(15), 1820, doi:10.1029/2003GL017814.

Mann, M. E., R. S. Bradley, and M. K. Hughes (1998), Global-scale temperature patterns and climate forcing over the past six centuries, *Nature*, *392*, 779–787.

Mann, M. E., Z. Zhang, M. K. Hughes, R. S. Bradley, S. K. Miller, S. Rutherford, and F. Ni (2008), Proxy-based reconstructions of hemispheric and global surface temperature variations over the past two millennia, *Proc. Natl. Acad. Sci. U. S. A.*, *105*(36), 13252–13257, doi:10.1073/pnas.0805721105.

Mbengue, C., and T. Schneider (2013), Storm track shifts under climate change: What can be learned from large-scale dry dynamics, *J. Clim.*, *26*(24), 9923–9930, doi:10.1175/JCLI-D-13-00404.1.

McAfee, S. A., and J. L. Russell (2008), Northern annular mode impact on spring climate in the western United States, *Geophys. Res. Lett.*, *35*, L17701, doi:10.1029/2008GL034828.

McCarroll, D., E. Pettigrew, A. Luckman, F. Guibal, and J.-L. Edouard (2002), Blue reflectance provides a surrogate for latewood density of high-latitude pine tree rings, *Arctic, Antarct. Alp. Res.*, *34*(4), 450–453.

McCarroll, D., R. Jalkanen, S. Hicks, M. Tuovinen, M. Gagen, F. Pawellek, D. Eckstein, U. Schmitt, J. Autio, and O. Heikkinen (2003), Multiproxy dendroclimatology: a pilot study in northern Finland, *The Holocene*, *13*(6), 829–838, doi:10.1191/0959683603hl668rp.

McCarroll, D., M. Tuovinen, R. Campbell, M. Gagen, H. Grudd, R. Jalkanen, N. J. Loader, and I. Robertson (2011), A critical evaluation of multi-proxy dendroclimatology in northern Finland, *J. Quat. Sci.*, *26*(1), 7–14, doi:10.1002/jqs.1408.

McCarroll, D., G. H. Young, and N. J. Loader (2015), Measuring the skill of variance-scaled climate reconstructions and a test for the capture of extremes, *The Holocene*, *25*(4), 618–626, doi:10.1177/0959683614565956.

McDowell, N. G., D. J. Beerling, D. D. Breshears, R. A. Fisher, K. F. Raffa, and M. Stitt (2011), The interdependence of mechanisms underlying climate-driven vegetation mortality, *Trends Ecol. Evol.*, *26*(10), 523–32, doi:10.1016/j.tree.2011.06.003.

McKee, T. B., N. J. Doesken, and J. Kleist (1993), The relationship of drought frequency and duration to time scales, in *Preprints from the Eighth Conference on Applied Climatology*, pp. 179–184, American Meteorological Society, Anaheim, CA.

Meko, D. M., and C. H. Baisan (2001), Pilot study of latewood-width of conifers as an indicator of variability of summer rainfall in the North American monsoon region, *Int. J. Climatol.*, *21*(6), 697–708, doi:10.1002/joc.646.

Meko, D. M., R. Touchan, and K. J. Anchukaitis (2011), Seascorr: A MATLAB program for identifying the seasonal climate signal in an annual tree-ring time series, *Comput. Geosci.*, *37*(9), 1234–1241, doi:10.1016/j.cageo.2011.01.013.

Meko, D. M., R. Touchan, J. V. Díaz, D. Griffin, C. A. Woodhouse, C. L. Castro, C. Carillo, and S. W. Leavitt (2013), Sierra San Pedro Mártir, Baja California, cool-season precipitation reconstructed from earlywood width of Abies concolor tree rings, *J. Geophys. Res. Biogeosciences*, *118*(4), 1660–1673, doi:10.1002/2013JG002408.

Mekonnen, M. M., and A. Y. Hoekstra (2016), Four billion people facing severe water scarcity, *Sci. Adv.*, *2*, e1500323, doi:10.1126/sciadv.1500323.

Mesinger, F. et al. (2006), North American regional reanalysis, *Bull. Am. Meteorol. Soc.*, *87*(3), 343–360, doi:10.1175/BAMS-87-3-343.

Moberg, A., D. M. Sonechkin, K. Holmgren, N. M. Datsenko, W. Karlén, and S.-E. Lauritzen (2005), Highly variable Northern Hemisphere temperatures reconstructed from low- and high-resolution proxy data., *Nature*, *433*(7026), 613–7, doi:10.1038/nature03265.

Monteith, J. L. (1965), Evaporation and environment, *Symp. Soc. Exp. Biol*.

Monteith, J. L. (1972), Solar radiation and productivity in tropical ecosystems, *J. Appl. Ecol.*, *9*(3), 747–766.

Monteith, J. L. (1977), Climate and the efficiency of crop production in britain, *Philos. Trans. R. Soc. B Biol. Sci.*, *281*, 277–294, doi:10.1098/rstb.1977.0140.

Moody, A., and D. M. Johnson (2001), Land-surface phenologies from AVHRR using the discrete fourier transform, *Remote Sens. Environ.*, *75*(3), 305–323, doi:10.1016/S0034-4257(00)00175-9.

Moorcroft, P. R. (2006), How close are we to a predictive science of the biosphere?, *Trends Ecol. Evol.*, *21*(7), 400–407, doi:10.1016/j.tree.2006.04.009.

Mote, P. W., and E. P. Salathé (2010), Future climate in the Pacific Northwest, *Clim. Change*, *102*(1–2), 29–50, doi:10.1007/s10584-010-9848-z.

Mote, P. W., A. F. Hamlet, M. P. Clark, and D. P. Lettenmaier (2005), Declining mountain snowpack in western North America, *Bull. Am. Meteorol. Soc.*, *86*(1), 39–49, doi:10.1175/BAMS-86-1-39.

Mu, Q., M. Zhao, F. A. Heinsch, M. Liu, H. Tian, and S. W. Running (2007), Evaluating water stress controls on primary production in biogeochemical and remote sensing based models, *J. Geophys. Res.*, *112*, G01012, doi:10.1029/2006JG000179.

Myneni, R. B. et al. (2002), Global products of vegetation leaf area and fraction absorbed PAR from year one of MODIS data, *Remote Sens. Environ.*, *83*, 214–231, doi:10.1016/S0034-4257(02)00074-3.

Nakamura, H. (1992), Midwinter Suppression of Baroclinic Wave Activity in the Pacific, *J. Atmos. Sci.*, *49*(17), 1629–1642, doi:10.1175/1520-0469(1992)049<1629:MSOBWA>2.0.CO;2.

Nehrbass-Ahles, C., F. Babst, S. Klesse, M. Nötzli, O. Bouriaud, R. Neukom, M. Dobbertin, and D. Frank (2014), The influence of sampling design on tree-ring-based quantification of forest growth, *Glob. Chang. Biol.*, *20*(9), 2867–2885, doi:10.1111/gcb.12599.

Nemani, R. R., C. D. Keeling, H. Hashimoto, W. M. Jolly, S. C. Piper, C. J. Tucker, R. B. Myneni, and S. W. Running (2003), Climate-driven increases in global terrestrial net primary production from 1982 to 1999, *Science*, *300*(5625), 1560–1563.

Neukom, R., J. Luterbacher, R. Villalba, M. Küttel, D. Frank, P. D. Jones, M. Grosjean, J. Esper, L. Lopez, and H. Wanner (2010), Multi-centennial summer and winter precipitation variability in southern South America, *Geophys. Res. Lett.*, *37*, L14708, doi:10.1029/2010GL043680.

Neukom, R. et al. (2011), Multiproxy summer and winter surface air temperature field reconstructions for southern South America covering the past centuries, *Clim. Dyn.*, *37*, 35–51, doi:10.1007/s00382-010-0793-3.

Nightingale, J. M., N. C. Coops, R. H. Waring, and W. W. Hargrove (2007), Comparison of MODIS gross primary production estimates for forests across the U.S.A. with those generated by a simple process model, 3-PGS, *Remote Sens. Environ.*, *109*(4), 500–509, doi:10.1016/j.rse.2007.02.004.

Notaro, M., A. Mauss, and J. W. Williams (2012), Projected vegetation changes for the American Southwest: combined dynamic modeling and bioclimatic-envelope approach, *Ecol. Appl.*, *22*(4), 1365–1388.

Offermann, C., J. P. Ferrio, J. Holst, R. Grote, R. Siegwolf, Z. Kayler, and A. Gessler (2011), The long way down--are carbon and oxygen isotope signals in the tree ring uncoupled from canopy physiological processes?, *Tree Physiol.*, *31*(10), 1088–1102, doi:10.1093/treephys/tpr093.

Omernik, J. M. (1987), Ecoregions of the conterminous United States, *Ann. Assoc. Am. Geogr.*, *77*(1), 118–125.

Oster, J. L., D. E. Ibarra, M. J. Winnick, and K. Maher (2015), Steering of westerly storms over western North America at the Last Glacial Maximum, *Nat. Geosci.*, *8*(3), 201–205, doi:10.1038/ngeo2365.

Pal, M. (2005), Random forest classifier for remote sensing classification, *Int. J. Remote Sens.*, *26*(1), 217–222, doi:10.1080/01431160412331269698.

Pallardy, S. G. (2008), *Physiology of Woody Plants*, 3rd ed., Academic Press, New York, NY.

Pan, Y., R. Birdsey, J. Hom, K. McCullough, and K. Clark (2006), Improved estimates of net primary productivity from MODIS satellite data at regional and local scales, *Ecol. Appl.*, *16*(1), 125–32.

Pan, Y. et al. (2011), A large and persistent carbon sink in the world's forests, *Science*, *333*, 988–993.

Pederson, G. T., S. T. Gray, C. A. Woodhouse, J. L. Betancourt, D. B. Fagre, J. S. Littell, E. Watson, B. H. Luckman, and L. J. Graumlich (2011), The unusual nature of recent snowpack declines in the North American cordillera, *Science*, *333*, 332–335, doi:10.1126/science.1201570.

Penny, S. M., D. S. Battisti, and H. R. Gerard (2013), Examining mechanisms of variability within the pacific storm track: Upstream seeding and jet-core strength, *J. Clim.*, *26*(14), 5242–5259, doi:10.1175/JCLI-D-12-00017.1.

Peterson, D. W., and D. L. Peterson (1994), Effects of climate on radial growth of subalpine conifers in the North Cascade Mountains, *Can. J. For. Res.*, *24*, 1921–1932.

Peterson, D. W., and D. L. Peterson (2001), Mountain hemlock growth responds to climatic variability at annual and decadal time scales, *Ecology*, *82*(12), 3330–3345.

Peterson, D. W., D. L. Peterson, and G. J. Ettl (2002), Growth responses of subalpine fir to climatic variability in the Pacific Northwest, *Can. J. For. Res.*, *32*, 1503–1517, doi:10.1139/X02-072.

Pierce, D. W., and D. R. Cayan (2013), The uneven response of different snow measures to human-induced climate warming, *J. Clim.*, *26*(12), 4148–4167, doi:10.1175/JCLI-D-12-00534.1.

Pierce, D. W. et al. (2013), Probabilistic estimates of future changes in California temperature and precipitation using statistical and dynamical downscaling, *Clim. Dyn.*, *40*(3–4), 839–856, doi:10.1007/s00382-012-1337-9.

Pinzon, J. E., and C. J. Tucker (2014), A non-stationary 1981-2012 AVHRR NDVI3g time series, *Remote Sens.*, *6*(8), 6929–6960, doi:10.3390/rs6086929.

Prasad, A. M., L. R. Iverson, and A. Liaw (2006), Newer Classification and Regression Tree Techniques: Bagging and Random Forests for Ecological Prediction, *Ecosystems*, *9*(2), 181–199, doi:10.1007/s10021-005-0054-1.

Quadrelli, R., and J. M. Wallace (2002), Dependence of the structure of the Northern Hemisphere annular mode on the polarity of ENSO, *Geophys. Res. Lett.*, *29*(23), 2132, doi:10.1029/2002GL015807.

R Core Team (2014), R: A Language and Environment for Statistical Computing, R Foundation for Statistical Computing, Vienna, Austria.

Rathgeber, C., A. Nicault, J. Guiot, T. Keller, F. Guibal, and P. Roche (2000), Simulated responses of Pinus halepensis forest productivity to climatic change and CO2 increase using a statistical model, *Glob. Planet. Change*, *26*(4), 405–421, doi:10.1016/S0921-8181(00)00053-9.

Restaino, C. M., D. L. Peterson, and J. Littell (2016), Increased water deficit decreases Douglas fir growth throughout western US forests, *Proc. Natl. Acad. Sci.*, doi:10.1073/pnas.1602384113.

Richardson, A. D., T. F. Keenan, M. Migliavacca, Y. Ryu, O. Sonnentag, and M. Toomey (2013), Climate change, phenology, and phenological control of vegetation feedbacks to

the climate system, *Agric. For. Meteorol.*, *169*, 156–173, doi:10.1016/j.agrformet.2012.09.012.

Riveros-Iregui, D. A., and B. L. McGlynn (2009), Landscape structure control on soil CO2 efflux variability in complex terrain: Scaling from point observations to watershed scale fluxes, *J. Geophys. Res.*, *114*, G02010, doi:10.1029/2008JG000885.

Riveros-Iregui, D. A., B. L. McGlynn, L. A. Marshall, D. L. Welsch, R. E. Emanuel, and H. E. Epstein (2011), A watershed-scale assessment of a process soil CO2 production and efflux model, *Water Resour. Res.*, *47*, W00J04, doi:10.1029/2010WR009941.

Rogers, B. M., R. P. Neilson, R. Drapek, J. M. Lenihan, J. R. Wells, D. Bachelet, and B. E. Law (2011), Impacts of climate change on fire regimes and carbon stocks of the U.S. Pacific Northwest, *J. Geophys. Res.*, *116*, G03037, doi:10.1029/2011JG001695.

Running, S. W. (2012), A Measurable Planetary Boundary for the Biosphere, *Science*, *337*, 1458–1459, doi:10.1126/science.1227620.

Running, S. W., R. R. Nemani, F. A. Heinsch, M. Zhao, M. Reeves, and H. Hashimoto (2004), A Continuous Satellite-Derived Measure of Global Terrestrial Primary Production, *Bioscience*, *54*(6), 547–560, doi:10.1641/0006-3568(2004)054[0547:ACSMOG]2.0.CO;2.

Rupp, D. E., J. T. Abatzoglou, and P. W. Mote (2016), Projections of 21st century climate of the Columbia River Basin, *Clim. Dyn.*, doi:10.1007/s00382-016-3418-7.

Rydval, M., L.-Å. Larsson, L. McGlynn, B. E. Gunnarson, N. J. Loader, G. H. F. Young, and R. Wilson (2014), Blue intensity for dendroclimatology: Should we have the blues? Experiments from Scotland, *Dendrochronologia*, *32*(3), 191–204, doi:10.1016/j.dendro.2014.04.003.

Salathé, E. P. (2006), Influences of a shift in North Pacific storm tracks on western North American precipitation under global warming, *Geophys. Res. Lett.*, *33*, L19820, doi:10.1029/2006GL026882.

Seager, R., and G. A. Vecchi (2010), Greenhouse warming and the 21st century hydroclimate of southwestern North America, *Proc. Natl. Acad. Sci. U. S. A.*, *107*(50), 21277–82, doi:10.1073/pnas.0910856107.

Seager, R., M. Ting, C. Li, N. Naik, B. Cook, J. Nakamura, and H. Liu (2013), Projections of declining surface-water availability for the southwestern United States, *Nat. Clim. Chang.*, *3*(5), 482–486, doi:10.1038/nclimate1787.

Settele, J., R. Scholes, R. A. Betts, S. Bunn, P. Leadley, D. Nepstad, J. T. Overpeck, and M. A. Taboada (2014), Terrestrial and Inland Water Systems, in *Climate Change 2014: Impacts, Adaptation, and Vulnerability. Part A: Global and Sectoral Aspects. Contribution of Working Group II to the Fifth Assessment Report of the Intergovernmental Panel on Climate Change*, edited by C. B. Field et al., pp. 271–359, Cambridge University Press, Cambridge, UK and New York, NY.

Shaw, T. A. et al. (2016), Storm track processes and the opposing influences of climate change, *Nat. Geosci.*, *9*, 656–665, doi:10.1038/ngeo2783.

Shugart, H. H. (1984), *A Theory of Forest Dynamics: The Ecological Implications of Forest Succession Models*, Springer-Verlag, New York, NY.

Smith, W. K., S. C. Reed, C. C. Cleveland, A. P. Ballantyne, W. R. L. Anderegg, W. R. Wieder, Y. Y. Liu, and S. W. Running (2016), Large divergence of satellite and Earth system model estimates of global terrestrial CO2 fertilization, *Nat. Clim. Chang.*, *6*(3), 306–310, doi:10.1038/nclimate2879.

Song, C., and C. E. Woodcock (2003), A regional forest ecosystem carbon budget model: impacts of forest age structure and landuse history, *Ecol. Modell.*, *164*(1), 33–47, doi:10.1016/S0304-3800(03)00013-9.

Song, C., M. P. Dannenberg, and T. Hwang (2013), Optical remote sensing of terrestrial ecosystem primary productivity, *Prog. Phys. Geogr.*, *37*(6), 834–854, doi:10.1177/0309133313507944.

Song, C., J. M. Chen, T. Hwang, A. Gonsamo, H. Croft, Q. Zhang, M. Dannenberg, Y. Zhang, C. Hakkenberg, and J. Li (2015), Ecological characterization of vegetation using multi-sensor remote sensing in the solar reflective spectrum, in *Remote Sensing Handbook, Volume 2: Land Resources Monitoring, Modeling, and Mapping*, edited by P. S. Thenkabail, pp. 533–575, CRC Press, Boca Raton, FL.

Soulé, P. T., and P. A. Knapp (2011), Radial Growth and Increased Water-Use Efficiency for Ponderosa Pine Trees in Three Regions in the Western United States, *Prof. Geogr.*, *63*(3), 379–391, doi:10.1080/00330124.2011.574088.

St. George, S. (2014), An overview of tree-ring width records across the Northern Hemisphere, *Quat. Sci. Rev.*, *95*, 132–150, doi:10.1016/j.quascirev.2014.04.029.

St. George, S., and T. R. Ault (2014), The imprint of climate within Northern Hemisphere trees, *Quat. Sci. Rev.*, *89*, 1–4, doi:10.1016/j.quascirev.2014.01.007.

St. George, S., D. M. Meko, and E. R. Cook (2010), The seasonality of precipitation signals embedded within the North American Drought Atlas, *The Holocene*, *20*(6), 983–988, doi:10.1177/0959683610365937.

Stahle, D. W., M. K. Cleaveland, H. D. Grissino-Mayer, R. D. Griffin, F. K. Fye, M. D. Therrell, D. J. Burnette, D. M. Meko, and J. Villanueva Diaz (2009), Cool- and warm-season precipitation reconstructions over western New Mexico, *J. Clim.*, *22*(13), 3729–3750, doi:10.1175/2008JCLI2752.1.

Steinman, B. A., M. B. Abbott, M. E. Mann, N. D. Stansell, and B. P. Finney (2012), 1,500 year quantitative reconstruction of winter precipitation in the Pacific Northwest, *Proc. Natl. Acad. Sci. U. S. A.*, *109*(29), 11619–11623, doi:10.1073/pnas.1201083109.

Stewart, I. T., D. R. Cayan, and M. D. Dettinger (2005), Changes toward earlier streamflow timing across western North America, *J. Clim.*, *18*, 1136–1155, doi:10.1175/JCLI3321.1.

Stokes, M. A., and T. L. Smiley (1968), *An Introduction to Tree-Ring Dating*, University of Chicago Press, Chicago, IL.

Tang, G., J. A. Arnone, P. S. J. Verburg, R. L. Jasoni, and L. Sun (2015), Trends and climatic sensitivities of vegetation phenology in semiarid and arid ecosystems in the US Great Basin during 1982-2011, *Biogeosciences*, *12*(23), 6985–6997, doi:10.5194/bg-12-6985-2015.

Torrence, C., and G. P. Compo (1998), A practical guide to wavelet analysis, *Bull. Am. Meteorol. Soc.*, *79*(1), 61–78.

Touchan, R., E. Xoplaki, G. Funkhouser, J. Luterbacher, M. K. Hughes, N. Erkan, Ü. Akkemik, and J. Stephan (2005), Reconstructions of spring/summer precipitation for the Eastern Mediterranean from tree-ring widths and its connection to large-scale atmospheric circulation, *Clim. Dyn.*, *25*, 75–98, doi:10.1007/s00382-005-0016-5.

Urban, D. L., M. E. Harmon, and C. B. Halpern (1993), Potential response of pacific northwestern forests to climatic change, effects of stand age and initial composition, *Clim. Change*, *23*(3), 247–266, doi:10.1007/BF01091618.

USDA Natural Resources Conservation Service (2016), Snow Telemetry (SNOTEL) and Snow Course Data and Products, *Natl. Clim. Water Cent.* Available from: http://www.wcc.nrcs.usda.gov/snow/ (Accessed 27 September 2016)

Vicente-Serrano, S. M., S. Beguería, and J. I. López-Moreno (2010a), A multiscalar drought index sensitive to global warming: The standardized precipitation evapotranspiration index, *J. Clim.*, *23*(7), 1696–1718, doi:10.1175/2009JCLI2909.1.

Vicente-Serrano, S. M., S. Beguería, J. I. López-Moreno, M. Angulo, and A. El Kenawy (2010b), A new global 0.5° gridded dataset (1901–2006) of a multiscalar drought index: comparison with current drought index datasets based on the Palmer Drought Severity Index, *J. Hydrometeorol.*, *11*(4), 1033–1043, doi:10.1175/2010JHM1224.1.

Vicente-Serrano, S. M. et al. (2013), Response of vegetation to drought time-scales across global land biomes, *Proc. Natl. Acad. Sci. U. S. A.*, *110*(1), 52–57, doi:10.1073/pnas.1207068110.

Vicente-Serrano, S. M., J. J. Camarero, and C. Azorin-Molina (2014), Diverse responses of forest growth to drought time-scales in the Northern Hemisphere, *Glob. Ecol. Biogeogr.*, *23*(9), 1019–1030, doi:10.1111/geb.12183.

Watson, E., and B. H. Luckman (2001), Dendroclimatic reconstruction of precipitation for sites in the southern Canadian Rockies, *The Holocene*, *11*(2), 203–213.

Watson, E., and B. H. Luckman (2002), The dendroclimatic signal in Douglas-fir and ponderosa pine tree-ring chronologies from the southern Canadian Cordillera, *Can. J. For. Res.*, *32*, 1858–1874, doi:10.1139/X02-096.

Wei, S., Y. Dai, Q. Duan, B. Liu, and H. Yuan (2014), A global soil data set for earth system modeling, *J. Adv. Model. Earth Syst.*, *6*, 249–263, doi:10.1002/2013MS000282.Received.

Westerling, A. L., H. G. Hidalgo, D. R. Cayan, and T. W. Swetnam (2006), Warming and earlier spring increase western U.S. forest wildfire activity., *Science*, *313*(5789), 940–943, doi:10.1126/science.1128834.

Western, A. W., R. B. Grayson, G. Blöschl, G. R. Willgoose, and T. A. McMahon (1999), Observed spatial organization of soil moisture and its relation to terrain indices, *Water Resour. Res.*, *35*(3), 797–810, doi:10.1029/1998WR900065.

White, M. A. et al. (2009), Intercomparison, interpretation, and assessment of spring phenology in North America estimated from remote sensing for 1982-2006, *Glob. Chang. Biol.*, *15*(10), 2335–2359, doi:10.1111/j.1365-2486.2009.01910.x.

Wigley, T. M. L., K. R. Briffa, and P. D. Jones (1984), On the average value of correlated time series, with applications in dendroclimatology and hydrometeorology, *J. Clim. Appl. Meteorol.*, *23*, 201–213.

Wilcox, R. R. (2005), *Introduction to Robust Estimation and Hypothesis Testing*, 2nd ed., Academic Press, San Diego, CA.

Wilks, D. (2006), On "field significance" and the false discovery rate, *J. Appl. Meteorol. Climatol.*, *45*, 1181–1189.

Williams, A. P. et al. (2013), Temperature as a potent driver of regional forest drought stress and tree mortality, *Nat. Clim. Chang.*, *3*(3), 292–297, doi:10.1038/nclimate1693.

Williams, A. P. et al. (2015), Correlations between components of the water balance and burned area reveal new insights for predicting forest fire area in the southwest United States, *Int. J. Wildl. Fire*, *24*(1), 14–26, doi:10.1071/WF14023.

Wilson, R., E. Cook, R. D'Arrigo, N. Riedwyl, M. N. Evans, A. Tudhope, and R. Allan (2010), Reconstructing ENSO: the influence of method, proxy data, climate forcing and teleconnections, *J. Quat. Sci.*, *25*(1), 62–78, doi:10.1002/jqs.

Wilson, R., R. Rao, M. Rydval, C. Wood, L.-A. Larsson, and B. H. Luckman (2014), Blue Intensity for dendroclimatology: The BC blues: A case study from British Columbia, Canada, *The Holocene*, doi:10.1177/0959683614544051.

Wise, E. K. (2010a), Climate–streamflow linkages in the north-central Rocky Mountains: implications for a changing climate, *Ann. Assoc. Am. Geogr.*, *100*(4), 806–817, doi:10.1080/00045608.2010.500246.

Wise, E. K. (2010b), Spatiotemporal variability of the precipitation dipole transition zone in the western United States, *Geophys. Res. Lett.*, *37*, L07706, doi:10.1029/2009GL042193.

Wise, E. K. (2010c), Tree ring record of streamflow and drought in the upper Snake River, *Water Resour. Res.*, *46*, W11529, doi:10.1029/2010WR009282.

Wise, E. K., and M. P. Dannenberg (2014), Persistence of pressure patterns over North America and the North Pacific since AD 1500, *Nat. Commun.*, *5*, 4912, doi:10.1038/ncomms5912.

Yi, L., H. Yu, J. Ge, Z. Lai, X. Xu, L. Qin, and S. Peng (2012), Reconstructions of annual summer precipitation and temperature in north-central China since 1470 AD based on drought/flood index and tree-ring records, *Clim. Change*, *110*, 469–498, doi:10.1007/s10584-011-0052-6.

Yin, J. H. (2005), A consistent poleward shift of the storm tracks in simulations of 21st century climate, *Geophys. Res. Lett.*, *32*, L18701, doi:10.1029/2005GL023684.

Zhang, L., B. Wylie, T. Loveland, E. Fosnight, L. L. Tieszen, L. Ji, and T. Gilmanov (2007a), Evaluation and comparison of gross primary production estimates for the Northern Great Plains grasslands, *Remote Sens. Environ.*, *106*(2), 173–189, doi:10.1016/j.rse.2006.08.012.

Zhang, X., D. Tarpley, and J. T. Sullivan (2007b), Diverse responses of vegetation phenology to a warming climate, *Geophys. Res. Lett.*, *34*, L19405, doi:10.1029/2007GL031447.

Zhang, Y., C. Song, K. Zhang, X. Cheng, and Q. Zhang (2014), Spatial-temporal variability of terrestrial vegetation productivity in the Yangtze River Basin during 2000-9, *J. Plant Ecol.*, *7*(1), 10–23, doi:10.1093/jpe/rtt025.

Zhang, Y., C. Song, G. Sun, L. E. Band, A. Noormets, and Q. Zhang (2015), Understanding moisture stress on light use efficiency across terrestrial ecosystems based on global flux and remote-sensing data, *J. Geophys. Res. Biogeosciences*, *120*, 2053–2066, doi:10.1002/2015JG003023.Received.